

12-2013

Steady-State Switching and Dispersion/Absorption Spectroscopy of Multistate Atoms Inside an Optical Ring Cavity

Jiteng Sheng

University of Arkansas, Fayetteville

Follow this and additional works at: <http://scholarworks.uark.edu/etd>

 Part of the [Optics Commons](#), and the [Plasma and Beam Physics Commons](#)

Recommended Citation

Sheng, Jiteng, "Steady-State Switching and Dispersion/Absorption Spectroscopy of Multistate Atoms Inside an Optical Ring Cavity" (2013). *Theses and Dissertations*. 970.
<http://scholarworks.uark.edu/etd/970>

This Dissertation is brought to you for free and open access by ScholarWorks@UARK. It has been accepted for inclusion in Theses and Dissertations by an authorized administrator of ScholarWorks@UARK. For more information, please contact scholar@uark.edu, ccmiddle@uark.edu.

Steady-State Switching and Dispersion/Absorption Spectroscopy of Multistate Atoms
Inside an Optical Ring Cavity

Steady-State Switching and Dispersion/Absorption Spectroscopy of Multistate Atoms
Inside an Optical Ring Cavity

A dissertation submitted in partial fulfillment
of the requirements for the degree of
Doctor of Philosophy in Physics

by

Jiteng Sheng
Zhejiang University
Bachelor of Science in Physics, 2008

December 2013
University of Arkansas

This dissertation is approved for recommendation to the Graduate Council.

Professor Min Xiao
Dissertation Director

Professor Julio Gea-Banacloche
Committee Member

Professor Reeta Vyas
Committee Member

Professor Surendra Singh
Committee Member

Professor Mark Arnold
Committee Member

ABSTRACT

This thesis mainly focuses on the experimental investigations of electromagnetically induced transparency (EIT) related phenomena in various systems involving multilevel atoms inside an optical ring cavity. Semiclassical methods, e.g. density-matrix equations, are used through out this thesis to simulate the experimental results. First, the cavity transmission spectrum can be significantly modified when multilevel atoms are placed inside an optical ring cavity. Such coupled atom-cavity systems are well explained by the intracavity dispersion/absorption properties. Specifically, three-level lambda-type, four-level N-type and double-lambda-type atoms inside an optical ring cavity are investigated by examining their cavity transmission spectra. Second, optical multistability (OM) has been demonstrated with EIT atoms inside an optical ring cavity. Such OM has been utilized to realize a controllable optical multistate switch, which can be modeled as a triple-well system. Third, self-Kerr nonlinearities of multilevel atoms are measured in an optical ring cavity by scanning the cavity length. Fourth, bright Stokes and anti-Stokes fields are generated simultaneously in a doubly-resonant atomic optical parametric oscillator (AOPO). In addition, vacuum-induced absorption and noise correlations are studied in the AOPO system. Last, a theoretical model is proposed to realize parity-time (PT) symmetry in a four-level N-type atomic system by spatially modifying the complex refractive index in free space. Moreover, the experimental progress is made to observe discrete diffraction pattern in an optically induced lattice by interfering with plane waves in a coherent atomic medium.

ACKNOWLEDGMENTS

It has been a long and wonderful journey to complete my doctoral dissertation and a subsequent Ph.D. degree. I came into this Ph.D. program as a bachelor who freshly completed the undergraduate degree with very limited knowledge of scientific research. Now, I am about to complete this journey as a husband, a father of two girls with accumulated scientific research experience and great passion to be a physicist in the future.

During this journey, I have received great support from a group of people. Within the supporters, I want to give my special and sincere appreciation to my supervisor Professor Min Xiao first for his generous support, thoughtful advising, gentle encouragement and patient directing. All I have learnt from him and his continuous help and support in all stages is the foundation for me to complete the dissertation. I have been very proud to be chosen by his dynamic and selective academic group, where my experimental skills and research abilities get well trained and greatly improved. His amazing physical intuition and abundant creative ideas have and will continue to guide me as a researcher. I still remember Professor Xiao's words when I began my study in the lab: "Every student who graduates from this lab is supposed to have ability to be an independent researcher in the future". This has always been my goal during the five years of my Ph.D. program.

I would also like to give my special thanks to all my advisory committee members for their guidance and encouragement through these years. Professor Julio Gea-Banacloche, as our

collaborator, provided me a lot of help and theoretical support on my first research work. Professor Surendra Singh, Professor Reeta Vyas, and Professor Mark Arnold as my lecturers of Laser Physics, Electrodynamics, and Scientific Computation, respectively, their rigorous teaching attitudes and profound knowledge also benefit my research in various aspects.

Thirdly, I would like to show my sincere appreciation to Dr. Haibin Wu, the person who first introduced me to the basic experimental skills and the idea of cavity EIT. Dr. Wu was a former Ph. D. student in our lab. He is now a professor in East China Normal University. His generous support and knowledge sharing helped me get rid of lots of difficulties on experiment techniques.

I am also very grateful to be able to work with Professor Demetrios N. Christodoulides and his Ph.D. student Mohammad-Ali Miri from University of Central Florida. During the last year of my Ph.D. program, we collaborated with them on a project to realize parity-time (PT) symmetry in coherent atomic media. Their professional knowledge on PT symmetry helped us to approach our goals faster, opened my eyes enriched my theoretical skills in this area. This is also essential for me to complete this dissertation.

I also want to extend my gratitude to other researchers whom I have worked with and learnt from during my Ph.D. program. Dr. Huaibin Zheng, a one-year visiting scholar from Xi'an Jiaotong University, taught me a lot of technical details about semiconductor lasers and the ideas of four-wave mixing when I first joining the lab. At the same time, I have also learnt a lot

from the discussions with Professor Jing Zhang, visiting professor from Shanxi University for one semester And Dr. Jianming Wen, post doctoral researcher in the lab at that time.

Meanwhile, I would like to show my appreciation to Dr. Youbin Yu, Dr. Xihua Yang and Utsab Khadka. After one and half years since I joined the group, I started to run the cavity system on my own. During this time, I learnt the ideas of quantum correlations and entanglement from the discussions with the visiting professor Dr. Yu, and the density-matrix methods from visiting professor Dr. Yang. I also frequently collaborated with Utsab, a former graduate student working on another optical table in the lab. We collaborated frequently with each other and yielded several works published during those years.

I would also like to thank other group members who joined and started working in the lab during my last semester, Jing Wang, Dr. Bing He, and visiting professor Shubin Yan. They brought fresh ideas and pleasure environment to our lab during my dissertation preparation.

Last, but certainly not least, I would like to thank my parents and my wife, Feiya Zhao, for their love and supports. Without them I could not have made it here. I would like to express my deepest gratitude to them.

TABLE OF CONTENTS

1	Introduction	1
1.1	Electromagnetically induced transparency.....	1
1.2	Four-wave mixing.....	6
1.3	Optical resonator.....	8
2	Cavity transmission spectra with multilevel atoms inside an optical cavity	12
2.1	Introduction.....	12
2.2	Side peak splitting and anti-crossing in a three-level atom-cavity system.....	13
2.3	Dressed intracavity dark state in a four-level N-type atom-cavity system.....	30
2.4	Intracavity dark-state field amplification by four-wave mixing.....	39
3	Optical multistability and all-optical multistate switching	51
3.1	Introduction.....	51
3.2	Observation of optical multistability in an intracavity three-level atomic system.....	52
3.3	Dual-channel optical multistability and multistate switching.....	67
4	Self-Kerr nonlinearity and optical parametric oscillator	75
4.1	Modified self-Kerr nonlinearity in an N-type atomic system.....	75
4.2	Noise correlations in a doubly-resonant optical parametric oscillator.....	88
5	Parity-time symmetry and photonic structures in atomic systems	98
5.1	Generation of parity-time symmetric potentials in an N-type atomic system.....	98
5.2	Observation of discrete diffraction pattern in an optically induced lattice.....	119
6	Conclusions and outlook	126
	Bibliography	131
A	Publications of dissertation author	146
A.1.	Journal papers.....	146
A.2.	Conference presentations.....	147

Chapter 1 Introduction

Light-matter interaction is a broad topic and plays a major role in a variety of research fields, such as, nonlinear and quantum optics, quantum information, nanophotonics, bioengineering, astronomy, and so on. The reason why the studies of the light-matter interactions are so important is that the light, which is composed of photons, is an attractive information carrier due to its fast speed and weak interaction with the environment. In addition, the light can strongly interact with the materials, selective coupling with matters, hence, it can be used to modify and explore the properties of the matter.

In this thesis, I will focus on the interactions of light with atoms [1]. The multilevel atoms are good candidates for exploring fundamental physical phenomena owing to their well studied and relatively simple energy level structures compared to molecules, and their rich available quantized energy levels make it possible for the atoms to interact with diverse light fields simultaneously. One notable and extensively studied phenomenon in the last two decades is the electromagnetically induced transparency (EIT) and its related effects [2-5]. By utilizing multiple light fields, the atoms can be coherently prepared into dark states, which make the light propagate through the atoms without absorption [2].

1.1 Electromagnetically induced transparency

The interaction strength between a light field and atoms depends critically on the frequency of the light field. When the light frequency is on resonance to a particular atomic transition, the

optical response of the medium is dramatically enhanced. However, this is usually accompanied by a strong absorption during the light propagation through such resonant medium. EIT, termed by Harris and co-workers [3], can be used to eliminate the linear absorption by quantum interference at the resonant frequency of an atomic transition. In addition, the steep normal linear dispersion and greatly enhanced nonlinearity are usually accompanied near the atomic resonance under EIT conditions [2].

A typical three-level lambda-type atomic system for EIT is shown in Fig. 1.1. A weak probe field and a strong coupling field with frequencies ω_p and ω_c interact with the transitions $|1\rangle\text{-}|3\rangle$ and $|2\rangle\text{-}|3\rangle$, respectively. The transition of $|1\rangle\text{-}|2\rangle$ is dipole-forbidden. The combined effect of the probe and coupling fields is to induce the atoms into a superposition state between the states $|1\rangle$ and $|2\rangle$, i.e. the dark state, which has no contribution from the excited state $|3\rangle$. Therefore, due to destructive quantum interference between two possible routes, i.e., directly via the $|1\rangle\text{-}|3\rangle$ pathway, or indirectly via the $|1\rangle\text{-}|3\rangle\text{-}|2\rangle\text{-}|3\rangle$ pathway, there is no possibility of excitation to $|3\rangle$, leading to a vanishing absorption for the probe field [2]. There are several ways to describe EIT process, such as density-matrix [6], dressed-state [7], probability amplitude [3], perturbation theory [8], Bloch vector [9], etc, and all these methods will lead to the same results except that the corresponding physical pictures give different insights in some aspects. In the following, we will choose the density-matrix method to model the EIT effect.

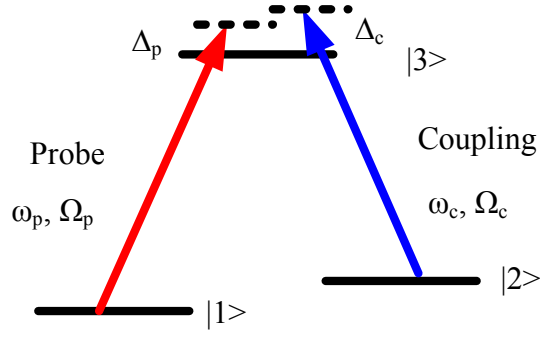


Figure 1.1: A typical three-level lambda-type atomic system for EIT [2].

In the interaction picture, the Hamiltonian of the three-level atom interacting with a coupling field and a probe field in a rotating frame can be written as [2]

$$H_{\text{int}} = -\frac{\hbar}{2} \begin{pmatrix} 0 & 0 & \Omega_p^* \\ 0 & 2(\Delta_p - \Delta_c) & \Omega_c^* \\ \Omega_p & \Omega_c & 2\Delta_p \end{pmatrix}. \quad (1.1)$$

Here $\Omega_p = \mu_{13}E_p / \hbar$ and $\Omega_c = \mu_{23}E_c / \hbar$ are the Rabi frequencies of the probe and coupling fields, and $\Delta_p = \omega_p - \omega_{13}$ and $\Delta_c = \omega_c - \omega_{23}$ are the frequency detunings of the probe and coupling fields, respectively. Then, the equations for the density-matrix elements under dipole and rotating-wave approximations are given by [5,10]

$$\begin{aligned}
\dot{\rho}_{22} &= -\Gamma_{21}\rho_{22} + \Gamma_{32}\rho_{33} + \frac{i}{2}(\rho_{32}\Omega_c^* - \rho_{23}\Omega_c), \\
\dot{\rho}_{33} &= -(\Gamma_{31}\rho_{33} + \Gamma_{32}\rho_{33}) + \frac{i}{2}(\rho_{23}\Omega_c - \rho_{32}\Omega_c^* + \rho_{13}\Omega_p - \rho_{31}\Omega_p^*), \\
\dot{\rho}_{21} &= -\tilde{\gamma}_{21}\rho_{21} + \frac{i}{2}\rho_{31}\Omega_c^* - \frac{i}{2}\rho_{23}\Omega_p, \\
\dot{\rho}_{31} &= -\tilde{\gamma}_{31}\rho_{31} + \frac{i}{2}\rho_{21}\Omega_c + \frac{i}{2}(\rho_{11} - \rho_{33})\Omega_p, \\
\dot{\rho}_{32} &= -\tilde{\gamma}_{32}\rho_{32} + \frac{i}{2}(\rho_{22} - \rho_{33})\Omega_c + \frac{i}{2}\rho_{12}\Omega_p.
\end{aligned} \tag{1.2}$$

Here, we define $\tilde{\gamma}_{21} = \gamma_{21} - i(\Delta_p - \Delta_c)$, $\tilde{\gamma}_{31} = \gamma_{31} - i\Delta_p$, and $\tilde{\gamma}_{32} = \gamma_{32} - i\Delta_c$. Γ_{nm} is the natural decay rate between level $|n\rangle$ and level $|m\rangle$; and $\gamma_{nm} = \frac{1}{2}(\Gamma_n + \Gamma_m)$.

If we assume that the coupling field is much stronger than the probe field, i.e. $\Omega_p \ll \Omega_c$, and the population is all in the ground state, i.e. $\rho_{11} \approx 1$, $\rho_{22} \approx \rho_{33} \approx 0$, then by solving Eq. (1.2) at the steady-state condition, we can get [5]

$$\rho_{31} = \frac{i\Omega_p/2}{\tilde{\gamma}_{31} + \frac{|\Omega_c|^2/4}{\tilde{\gamma}_{21}}}. \tag{1.3}$$

The susceptibility of the atomic medium is proportional to ρ_{31} . Figures 1.2(a) and (b) show the linear susceptibility of the atomic medium for the two-level system, i.e. $\Omega_c = 0$, and the three-level EIT system, i.e. $\Omega_c \neq 0$, respectively. The black solid curves represent the real parts of the susceptibilities, while the red dotted curves are the imaginary parts. From Fig. 1.2(b), it is clear that the absorption is significantly suppressed near the atomic resonance, leading to a transparency window, and the slope of the dispersion near the resonance changes from negative to positive for a three-level EIT system. Usually, the negative dispersion slope leads to fast light,

while the positive dispersion slope gives rise to slow light. However, in the two-level system, the absorption is too strong to make the study of fast light difficult. In an EIT system, since the absorption can be negligible, the effect of the slow light owing to the steep positive dispersion is quite clear [5]. A lot of evidence of slow light has been experimentally observed [11,12], for example, Hau et al. has demonstrated that the speed of light can be reduced down to 17 meters per second in an ultracold EIT system [11]. Moreover, it was quickly realized that the light can be not only slowed down, but also stored in an EIT medium, which is known as optical memory [13,14] or quantum memory [15,16].

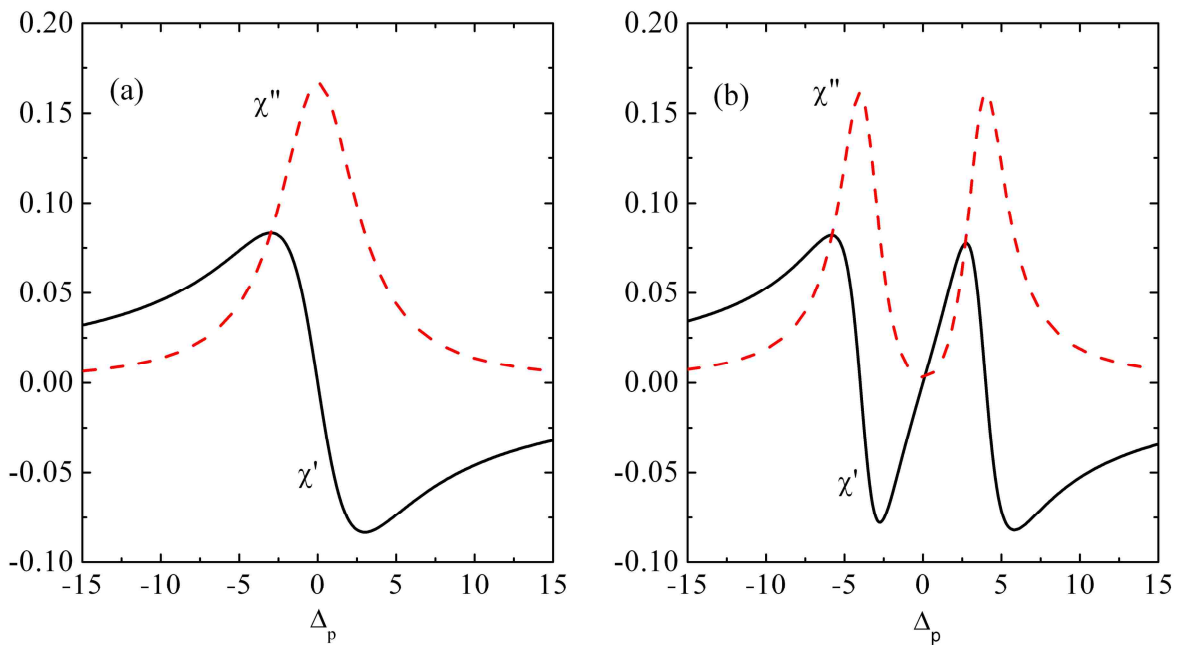


Figure 1.2: Linear susceptibility of the atomic medium, where χ' and χ'' represent the real and imaginary parts, respectively. (a) Two-level system, i.e. $\Omega_c = 0$. (b) Three-level EIT system, i.e. $\Omega_c \neq 0$ [2].

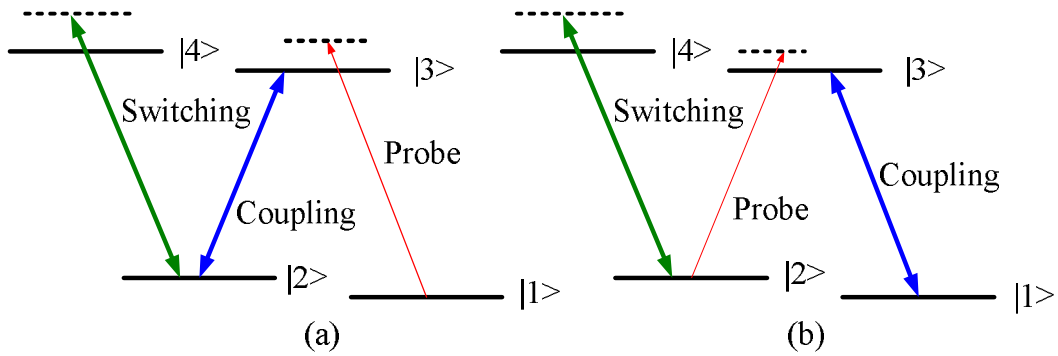


Figure 1.3: Two different types of four-level N-type systems [2].

Beside the three-level lambda-type atomic system, the ladder and V-type configurations can also be used to study EIT [2]. Moreover, by adding more light fields to drive additional atomic transitions based on the principal lambda scheme, a variety of other interesting schemes will emerge, such as N-type [17-27], M-type [28], inverted-Y-type [29], tripod-type [30], double-lambda-type [31-42], etc. Among those different configurations, the four-level N-type atomic system can generally be divided into two main schemes depending on the placement of the additional driving field. One is related to two-photon absorption [18], as shown in Fig. 1.3(a), and some applications of it will be discussed in Sections 2.3 and 4.1. The other is with an active Raman gain [27], as shown in Fig. 1.3(b), in which the weak probe field can be amplified, and more details will be discussed in Section 5.1.

1.2 Four-wave mixing

By the definition, four-wave mixing (FWM) [43] is a process with four different fields interacting in the same nonlinear medium. FWM process can be achieved in the so-called

double-lambda configuration in atoms [31-42], as illustrated in Fig. 1.4. From Fig. 1.4, it is clearly seen that four individual fields make a closed-circle in this double-lambda configuration, i.e., $\omega_1 + \omega_4 = \omega_2 + \omega_3$, which is the requirement for energy conservation. Another necessary condition for FWM is called the phase-matching condition [43], i.e. $k_1 + k_4 = k_2 + k_3$, here k_i ($i=1,2,3,4$) is the wave vector for each field. The double-lambda scheme shown in Fig. 1.4 has served as an important system in EIT-based FWM, because the FWM efficiency is dramatically improved due to the enhanced third-order nonlinearity by EIT [33]. Typically there are two possible FWM cases. One is that three fields are applied such that the fourth field is generated [31], and an application of this case will be provided in Section 2.4. The other is that two fields with one in each of the two lambda systems are applied such that two new fields can be generated corresponding to the Stokes and anti-Stokes components of the two applied fields [35], and more details will be presented in Sections 3.3 and 4.2.

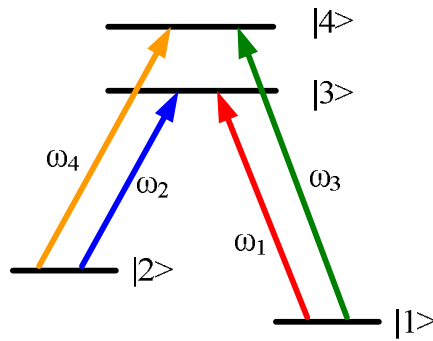


Figure 1.4: Four-wave mixing in a double-lambda configuration [2].

1.3 Optical resonator

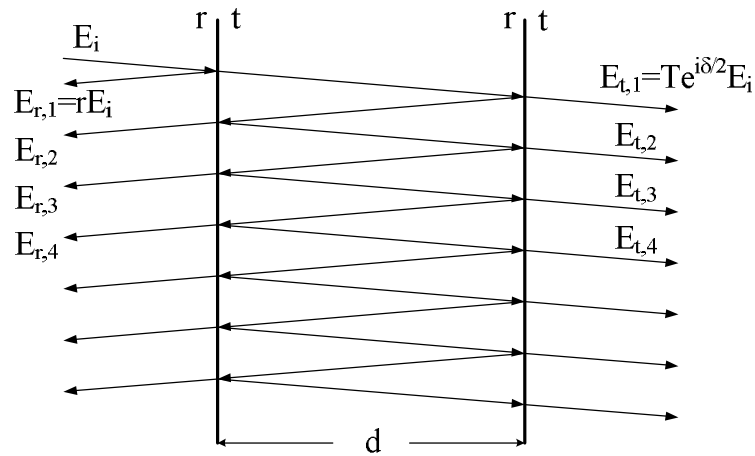


Figure 1.5: Multiple amplitude interference inside a Fabry-Perot cavity [44].

Optical resonator, i.e. optical cavity, is one key component of widely used in quantum and nonlinear optics experiments [44]. The simplest case for the optical resonator is the so-called Fabry-Perot (FP) cavity, which is typically made out of two parallel highly reflecting mirrors. The light coupled into this cavity will then circulate inside the cavity by reflecting back and forth between two cavity mirrors a number of times, and lead to the multiple interference of fields at the output or reflected field, as shown in Fig. 1.5. Therefore, the cavity output field amplitudes from all the round trips can be added up as [44]

$$\begin{aligned}
E_t &= E_{t,1} + E_{t,2} + E_{t,3} + \dots \\
&= E_{t,1} + Re^{i\delta} E_{t,1} + (Re^{i\delta})^2 E_{t,1} + \dots \\
&= \frac{E_{t,1}}{1 - Re^{i\delta}} \\
&= \frac{Te^{i\delta/2}}{1 - Re^{i\delta}} E_i.
\end{aligned} \tag{1.4}$$

Here, $E_{t,i}$ ($i = 1, 2, 3, \dots$) is the cavity output field amplitude of the i th round-trip, $\delta = \frac{4\pi d}{\lambda}$ is the single round-trip phase shift, and R (T) is the intensity reflectivity (transmission) of the cavity mirrors, respectively. The cavity output intensity can then be obtained as [44]

$$\frac{I_t}{I_i} = \frac{|E_t|^2}{|E_i|^2} = \frac{T^2}{(1 - R)^2 + 4R \sin^2\left(\frac{\delta}{2}\right)}. \tag{1.5}$$

Typical cavity transmission spectrum can then be plotted from Eq. (1.5), which is shown in Fig. 1.6. Free spectral range (FSR) is the space between two successive transmission maxima, and a measure of the sharpness or the width of the transmission peak is called full width at half maximum (FWHM).

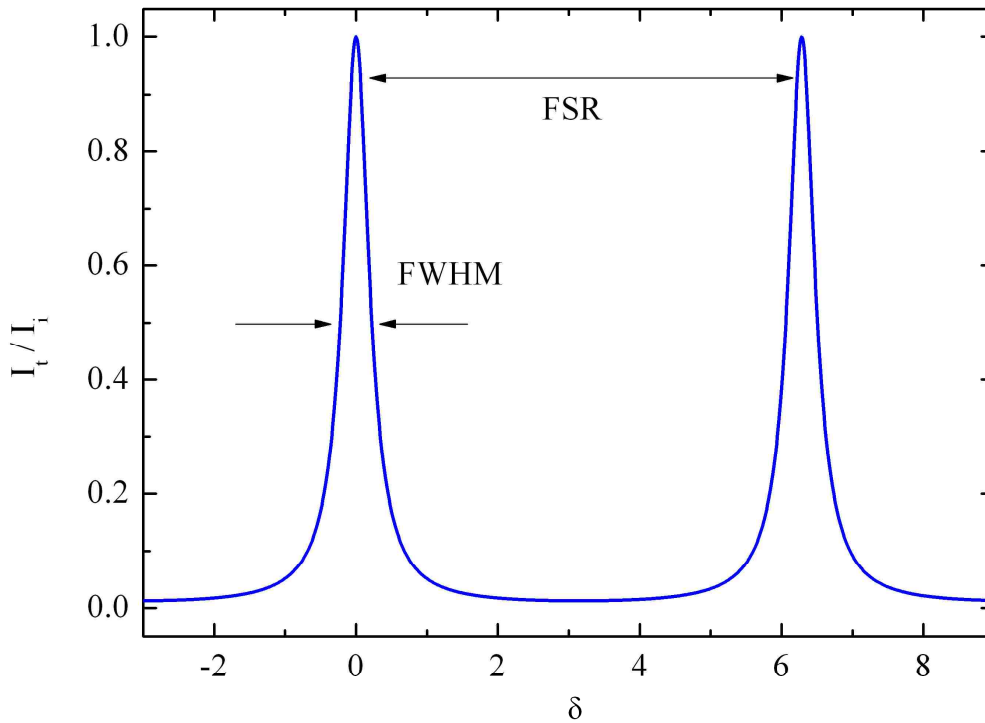


Figure 1.6: Typical cavity transmission spectrum [44].

As discussed above, the EIT medium can dramatically enhance the linear and nonlinear dispersions near the two-photon resonance associated with the eliminated absorption [2]. When EIT medium is placed inside an optical ring cavity, the properties of the atom-cavity system can be substantially affected, and it can exhibit distinguished effects compared to the EIT medium in free space or cavity containing two-level atoms. In the following, my research works in the Quantum and Nonlinear Optics Laboratory of Professor Min Xiao at the University of Arkansas during the last five years will be summarized, which are mainly based on the already published or going to be published results in peer-reviewed journals. Chapter 2 describes the modified

cavity transmission spectra of multilevel atoms inside an optical ring cavity. Chapter 3 presents the observation of optical multistabilities owing to the cavity feedback on three-level coherently-prepared (EIT) atoms, and the implementations of all-optical multistate switching. Chapter 4 includes both the measurement of the self-Kerr nonlinearity in a four-level N-type atomic system by scanning cavity length technique and the study of the noise correlations in a doubly-resonant optical parametric oscillator. In Chapter 5, a theoretical proposal is provided to generate parity-time (PT) symmetric potential in an N-type atomic system, and then the experimental observation of discrete diffraction pattern in an optically induced lattice is introduced, which may open up a novel platform for studying the properties of the periodically-modulated material and PT symmetry in coherent atomic media. Chapter 6 gives the conclusion and outlook.

Chapter 2 Cavity transmission spectra with multilevel atoms inside an optical cavity

2.1 Introduction

The cavity transmission spectrum will become more complex than the one for the empty cavity when a multilevel atomic medium is placed inside an optical cavity, which can be explained by the cavity quantum electrodynamics (cavity-QED) [45-47] or the intracavity absorption and dispersion properties [48,49]. A well-known cavity-QED effect is the so-called “normal-mode splitting” or “vacuum Rabi splitting” phenomenon [50-61] with the atom-cavity system exhibiting a double-peaked transmission spectrum when two-level atoms are coupled into a single cavity mode under the strong-coupling condition, which can be mathematically described by the Jaynes-Cummings model [62]. Such fundamental cavity-QED system has been widely studied experimentally in atomic beams [50,52], cold atomic clouds [54,55], ultra-cold atoms [57], hot atomic vapor [61], and so on. There are typically two ways to enhance the coupling strength to achieve the strong coupling regime, one is to use microcavity by decrease the cavity mode volume [50], and the other is to increase the atom number in the cavity since the effective coupling strength of the cavity with atoms is given by $g\sqrt{N}$, where g is the coupling parameter of a single atom with single-mode cavity field and N is the number of atoms in the cavity mode. Additionally, long atomic and field lifetimes are also essential to reach the strong coupling regime [45]. When the two-level atoms are replaced by three-level EIT atoms [63], an additional narrow central peak appears, which is named as “dark-state polariton” [64]. The incorporation of EIT in the intracavity medium will not only enrich the fundamental

understanding of cavity-QED, but can also lead to some new applications in quantum computation and quantum information processing. Such signature three-peak spectrum with three-level EIT atom-cavity coupling has been observed in cold atoms [65], hot atomic vapor [63], ion Coulomb crystals [66], and even in a single atom [67]. The splitting of the dark-state peak when four-level N-type atoms are used inside an optical cavity [25,68], and the amplification of the intracavity dark-state field by a FWM process in a double-lambda atom-cavity system [42] were also observed recently. In Section 2.2, the side peak splitting and anti-crossing-like phenomena in a three-level atom-cavity system will be presented in the following. Section 2.3 shows the splitting of the dark-state peak in a four-level N-type atom-cavity system, and Section 2.4 describes the amplification of the intracavity dark-state field by an intracavity FWM process.

2.2 Side peak splitting and anti-crossing in a three-level atom-cavity system

It is possible to explain the cavity transmission peak structures by solving the Maxwell-Bloch or Heisenberg-Langevin equations in investigating simple systems, such as a cavity coupled to a homogeneously-broadened two-level atomic medium [53] or with three-level EIT atoms on resonance [63]. When fully considering the cavity transmission spectrum of an atom-cavity system coupled with three-level Doppler-broadened atoms including frequency detunings, we show that the linear dispersion and absorption properties can be used to qualitatively explain the complex cavity transmission spectra under different experimental conditions. The advantage of only considering the linear dispersion and absorption properties when the probe (cavity) field is

relatively weak is that it is straightforward and sufficient to understand the major characteristics of the cavity transmission peaks, such as the number of peaks and their positions.

When an atomic medium is placed inside an optical cavity, the normalized intensity transmission function of an empty cavity in Eq. (1.5) is modified as

$$S(\omega_p) = \frac{I_{output}}{I_{input}} = \frac{T^2}{(1 - R\kappa)^2 + 4R\kappa \sin^2\left(\frac{\delta}{2}\right)}, \quad (2.1)$$

where $\kappa \equiv e^{-\alpha l/2}$ is the absorption of the intracavity medium and δ is the intracavity round-trip phase shift, which can be calculated as

$$\begin{aligned} \delta &= \frac{\omega_p L}{c} + \frac{(n-1)\omega_p l}{c} - 2\pi m \\ &= \frac{\omega_p L}{c} + \frac{(n-1)\omega_p l}{c} - \frac{\omega_{cav} L}{c} \\ &= \frac{(\omega_p - \omega_{cav} - \omega_{13} + \omega_{13})L}{c} + \frac{(n-1)\omega_p l}{c} \\ &= \frac{(\Delta_p - \Delta_\theta)L}{c} + \frac{\chi'(\omega_{13} + \Delta_p)l}{2c} \\ &\approx \left(\Delta + \frac{\chi'\omega_{13}l}{2L}\right) \frac{L}{c}. \end{aligned} \quad (2.2)$$

Here L is the total cavity length, l is the length of the medium, $\chi = \chi' + i\chi''$ is the complex susceptibility of the medium, $\Delta_p = \omega_p - \omega_{13}$ is the probe frequency detuning, $\Delta_\theta = \omega_{cav} - \omega_{13}$ is the cavity frequency detuning, and $\Delta = \Delta_p - \Delta_\theta$ is the relative frequency detuning (the probe detuning from the cavity resonance).

Therefore, the general cavity intensity transmission function of the coupled atom-cavity system is modified as [49,69]

$$S(\omega_p) = \frac{T^2}{1 + R^2 \kappa^2 - 2R\kappa \cos[(\Delta + (\omega_p l / 2L)\chi')L/c]}. \quad (2.3)$$

When $\Delta + (\omega_p l / 2L)\chi'$ equals to zero, the cavity intensity transmission function $S(\omega_p)$ has a maximum value, which corresponds to a peak in the cavity transmission spectrum. Here we define the detuning line as $-\Delta$ and the modified dispersion curve as $(\omega_p l / 2L)\chi'$ in Eq. (2.3).

When these two curves have an intersection, a peak appears in the transmission spectrum, i.e., cavity transmission intensity vs probe frequency detuning. Even when the detuning line, $-\Delta$, and the modified dispersion curve, $(\omega_p l / 2L)\chi'$, don't have an intersection, the place where the absolute difference between the detuning line and the dispersion curve has a minimum value could still generate a transmission peak, e.g. maximum value in Eq. (2.3) in the cavity transmission function [49,69].

When three-level EIT atoms are placed inside an optical cavity, typically a signature three-peak structure can be observed in the cavity transmission spectrum [63]. Two broad side peaks are caused by the “bright polaritons”, and the middle narrow peak is called “dark-state polariton” peak due to on-resonant EIT. The Langevin equations under the weak probe approximation can be given by [63]

$$\begin{aligned}
\dot{a} &= -i(\Delta_\theta - i\kappa) - ig\sqrt{N}\sigma_{13} + E_{in}, \\
\dot{\sigma}_{13} &= -i(\Delta_p - i\gamma_{31})\sigma_{13} - i\frac{\Omega_c}{2}\sigma_{12} - ig\sqrt{N}a, \\
\dot{\sigma}_{12} &= -i(\Delta_p - \Delta_c - i\gamma_{12})\sigma_{12} - i\frac{\Omega_c}{2}\sigma_{13}.
\end{aligned} \tag{2.4}$$

By assuming the resonances of the atoms and the cavity with the coupling and probe fields, i.e.

$\Delta_p = \Delta_c = \Delta_\theta = 0$, the eigenvalues of Eq. 2.4 can be solved to be

$$0, \pm\sqrt{g^2N + \Omega_c^2/4}. \tag{2.5}$$

Hence, the cavity transmission spectrum shows three distinct peaks with their corresponding eigenvalues as given in Eq. (2.5).

In the following, we will analyze the linear intracavity dispersion and absorption properties of such three-level EIT atom-cavity system, since it gives a good physical picture to qualitatively understand the complicated peak structures in the cavity transmission spectra from such coupled atom-cavity system, even with cavity, and coupling field frequency detunings.

Two on-resonance cases, i.e. $\Delta_\theta = \Delta_c = 0$, are illustrated in Fig. 2.1. The signature three-peak structure in cavity transmission spectrum can be observed in both cases as shown in Figs. 2.1(c) and (d), respectively. In the first case, the detuning line ($-\Delta = -\Delta_p$) does not cross the dispersion curve ($(\omega_p l / 2L)\chi'$) except at $\Delta_p = 0$, however, there still exist two broad side peaks at the places where the difference between the dispersion curve and the detuning line has a minimum value (Fig. 2.1(c)). In the second case, the detuning line crosses the dispersion

curve at several places. Since there are five crossings, one might expect to observe five peaks under certain experimental conditions [69]. However, since the absorption is quite large near the two-photon resonance as shown by the dotted curve in Fig. 2.1(b), therefore, at a relatively low probe intensity, the two peaks close to the probe resonance are severely absorbed (barely seen), leaving a three-peak structure with two narrower side peaks, as shown in Fig. 2.1(d).

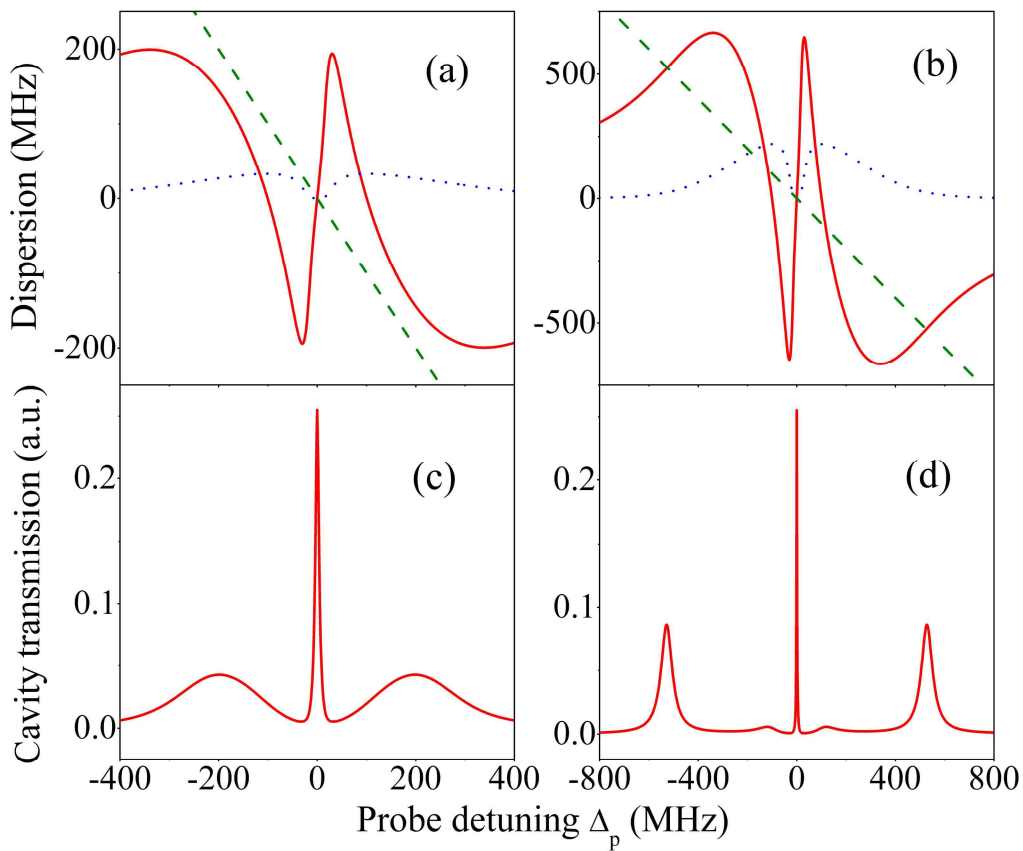


Figure 2.1: Theoretical plots of dispersion curves and cavity transmission spectra versus probe frequency detuning for a Doppler-broadened three-level atomic medium. (a) and (b): red solid curves are intracavity dispersion curves; blue dotted curves give the absorption (which are suppressed [63]); and green dashed lines are the detuning lines. (c) and (d) are the cavity

transmission spectra corresponding to (a) and (b), respectively. The parameters used in the calculation are: decay rate for the probe transition $\gamma_{31} = 2\pi \times 3 \text{ MHz}$, the ground-state dephasing rate $\gamma_{12} = 2\pi \times 0.1 \text{ MHz}$, $\Omega_c = 2\pi \times 32 \text{ MHz}$, the coupling detuning $\Delta_c = 0$, the cavity detuning $\Delta_\theta = 0$, and the atomic density $N = 1.5 \times 10^{10} \text{ cm}^{-3}$ or $N = 5 \times 10^{10} \text{ cm}^{-3}$ for (a) and (b), respectively.

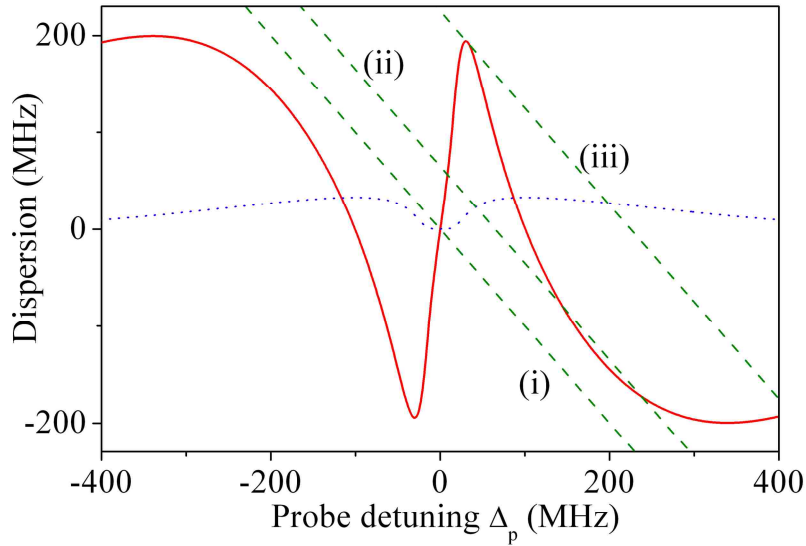


Figure 2.2: Dispersion picture at different cavity frequency detuning values. (i), (ii), and (iii) give the detuning line $-\Delta_p$ at different cavity detuning values. Other parameters used in the calculation are the same as in Fig. 2.1(a).

Next, we will interpret the cavity transmission spectrum when the cavity is detuned from its resonance, i.e. $\Delta_\theta \neq 0$, by utilizing the dispersion picture. Figure 2.2 depicts the cavity detuning cases for the situation as shown in Fig. 2.1(a). The calculated dispersion function $(\omega_p l / 2L)\chi'$ is plotted as a solid red curve. The green dashed lines represent the detuning line

$-\Delta = -(\Delta_p - \Delta_\theta)$ at different cavity detunings. The left dashed green line (i) is for the on-resonance case, i.e. $\Delta_\theta = \Delta_c = 0$, which shows three symmetric peaks in the cavity transmission, corresponding to the case shown in Fig. 2.1(c); the middle dashed green line (ii) and the right dashed green line (iii) are for the cases with cavity detunings, i.e. $\Delta_\theta \neq 0, \Delta_c = 0$, which lead to the complicated, asymmetric cavity transmission spectra. Let's first look at the experimental observations before going into complicated cavity transmission cases.

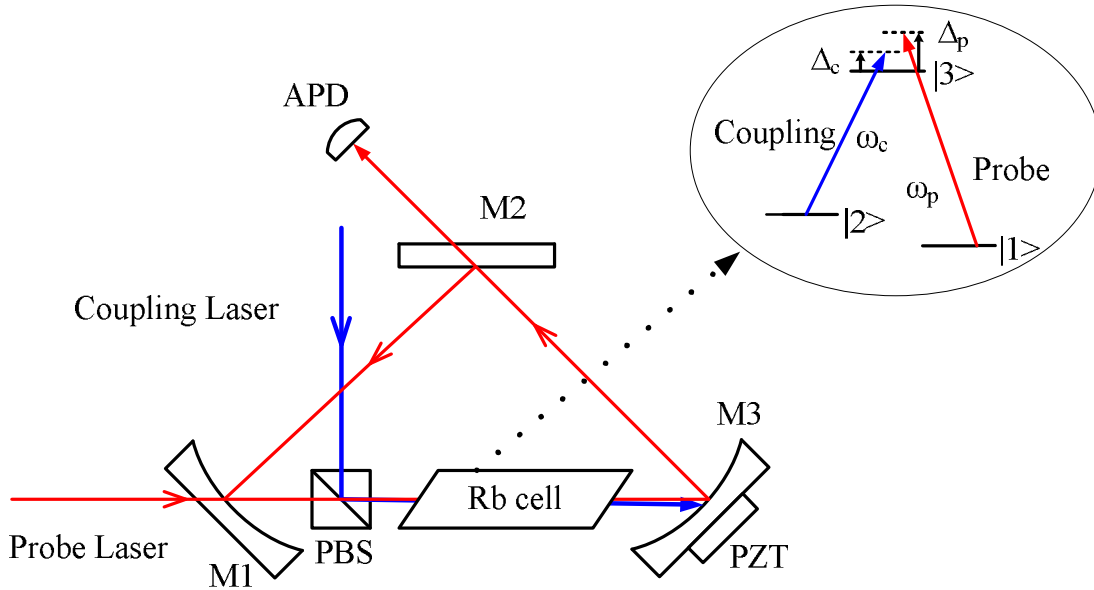


Figure 2.3: Experimental setup. PBS: polarization beam splitter; M1-M3: cavity mirrors; APD: avalanche photo-diode detector; and PZT: piezoelectric transducer.

The experimental setup is shown in Fig. 2.3. The probe and coupling laser beams are from two tunable single-mode diode lasers (Toptica DL 100), respectively, which are current and temperature stabilized with the linewidths ~ 1 MHz. A three-mirror optical ring cavity is composed of an input mirror M1 and a flat output mirror M2 with 3% and 1.4% transmissivities,

respectively; and a high reflector M3 (reflectivity > 99 %) mounted on a PZT for cavity frequency scanning and locking. M1 and M3 are curved mirrors with 10 cm radius of curvature. The cavity length L is 37 cm. The rubidium vapor cell is 5 cm long with Brewster windows, and is wrapped in μ -metal sheets for magnetic field shielding and in heat tape for heating. Three energy levels in D1 line of ^{87}Rb atoms are used for the three-level lambda-type EIT system. The probe field drives near the atomic transition of $5S_{1/2}, F=1 \rightarrow 5P_{1/2}, F'=2$ and the coupling field drives near the atomic transition of $5S_{1/2}, F=2 \rightarrow 5P_{1/2}, F'=2$. The coupling beam is injected through a polarization beam splitter (PBS), which does not circulate in the cavity. The probe beam is injected into the cavity via the input mirror M1 and circulates in the cavity as the cavity field, and the output is detected by an avalanche photo-diode detector (APD). The radii of the coupling and probe beams are estimated to be $600 \mu\text{m}$ and $100 \mu\text{m}$ at the center of the atomic cell, respectively. The empty cavity finesse is about 100. When the atomic cell and PBS are included, the cavity finesse decreases to about 48. An additional home-made frequency-stabilized diode laser with the wavelength $\sim 850 \text{ nm}$ is used to lock the optical ring cavity (not shown in Fig. 2.3).

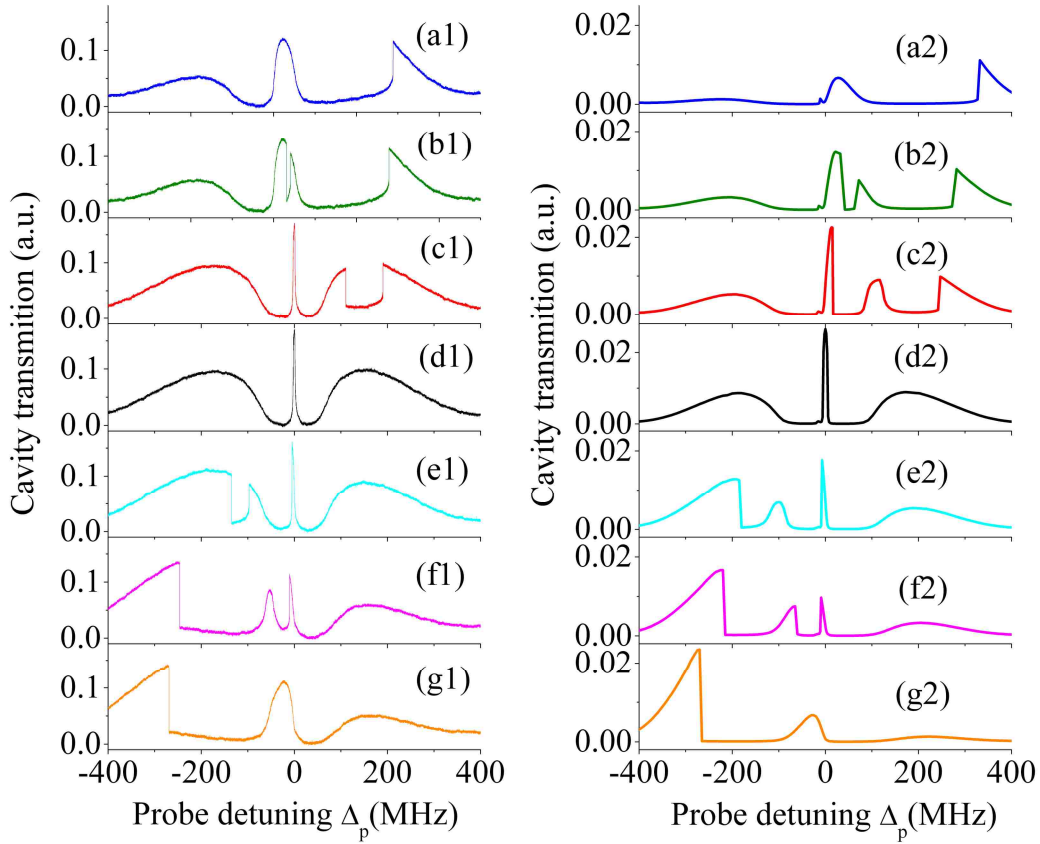


Figure 2.4: Cavity transmission spectra for different cavity detuning values. (a1)-(g1): The experimentally measured transmission spectra. (a1) $\Delta_\theta \approx 160$ MHz, (b1) $\Delta_\theta \approx 140$ MHz, (c1) $\Delta_\theta \approx 20$ MHz, (d1) $\Delta_\theta \approx 0$ MHz, (e1) $\Delta_\theta \approx -40$ MHz, (f1) $\Delta_\theta \approx -120$ MHz, (g1) $\Delta_\theta \approx -160$ MHz. (a2)-(g2): The theoretically calculated results corresponding to the measured spectra shown on (a1)-(g1), respectively. (a2) $\Delta_\theta \approx 80$ MHz, (b2) $\Delta_\theta \approx 40$ MHz, (c2) $\Delta_\theta \approx 20$ MHz, (d2) $\Delta_\theta \approx 0$ MHz, (e2) $\Delta_\theta \approx -20$ MHz, (f2) $\Delta_\theta \approx -40$ MHz, (g2) $\Delta_\theta \approx -80$ MHz.

Figure 2.4 plots the experimentally measured and theoretically calculated cavity transmission spectra versus the probe frequency detuning (Δ_p) for different cavity detuning (Δ_θ) values. Similar transmission spectra have been reported in Ref. [69] at the resonant case

($\Delta_\theta = \Delta_c = 0$) with two symmetric broad side peaks (at a slightly higher temperature of $T = 80.3$ °C) as shown in Fig. 2.4(d1). When the cavity is positively detuned to around 20 MHz, the right side peak begins to split into two peaks (Fig. 2.4(c1)). As the cavity detuning (Δ_θ) further increases, one of the split peaks moves outwards and another moves inwards (Fig. 2.4(b1)). The inward-moving peak merges with the central peak when the cavity frequency detuning $\Delta_\theta \approx 160$ MHz, as shown in Fig. 2.4(a1). If the cavity is negatively detuned, one can see a similar behavior for the left side peak (Figs. 2.4(e1)-(g1)) [49]. The other experimental parameters are as following: the probe power $P_p = 1.7$ mW, the coupling power $P_c = 13.7$ mW, the coupling detuning $\Delta_c = 0$, and the temperature $T = 80.3$ °C.

The central peak positions shown in Figs. 2.4(a1)-(g1) have slight changes, as shown in the inset of Fig. 2.5. The position of the central peak is determined by the frequency-pulling equation [70]:

$$\omega_r = \frac{1}{1+\eta} \omega_{cav} + \frac{\eta}{1+\eta} \omega_{13}. \quad (2.6)$$

Here, $\eta = \frac{\omega_p l}{2L} \frac{\partial \chi'}{\partial \Delta_p}$ defines the frequency-locking coefficient. This is quite different from the

experimental results reported in Ref. [65], in which the cavity detuning Δ_θ could not get too large because of the relatively low atomic density in that experiment, and the dispersion slope

around the EIT resonance is too sharp ($\eta = \frac{\omega_p l}{2L} \frac{\partial \chi'}{\partial \Delta_p} \approx 25$) to observe the obvious frequency

shift of the central peak owing to the frequency pulling effect. In the current experimental

system described in this section, the dispersion slope around the center (near resonance) is not that sharp and the cavity can be detuned as far as 250 MHz, therefore, it is possible to observe the frequency shift of the central peak position due to frequency pulling beyond noise range as predicted by Eq. (2.6). By measuring the frequency pulling slope as shown in the inset of Fig. 2.5, one can roughly calculate the group index and the group velocity from the slope value. Looking at the dispersion curve in Fig. 2.2, we would get the same result as shown in Fig. 2.4. The left dashed green line (i) in Fig. 2.2 gives the resonant case for the cavity, which corresponds to the case in Fig. 2.4(d1); the middle dashed green line (ii) in Fig. 2.2 corresponds to the splitting of the right side peak, which is the case in Fig. 2.4(c1); and the right dashed green line (iii) in Fig. 2.2 gives the case where the central peak and one of the split peaks begin to merge, which corresponds to Fig. 2.4(a1). We can choose ω_{13} as the origin, i.e. zero

detuning, and rewrite Eq. (2.6) as $\Delta_r = \frac{1}{1+\eta} \Delta_\theta$ with $\Delta_r = \omega_r - \omega_{13}$. From the inset of Fig. 2.5,

the slope can be determined to be $\Delta_r / \Delta_\theta \approx 0.1$, which gives $\eta = \frac{\omega_p l}{2L} \frac{\partial \chi'}{\partial \Delta_p} \approx 9$ in the current

case. The group index of the intracavity dispersive medium can be written as

$n_g \approx n + \omega_p \frac{1}{2} \frac{\partial \chi'}{\partial \omega_p}$, which gives $n_g \approx 68$ under the current experimental condition.

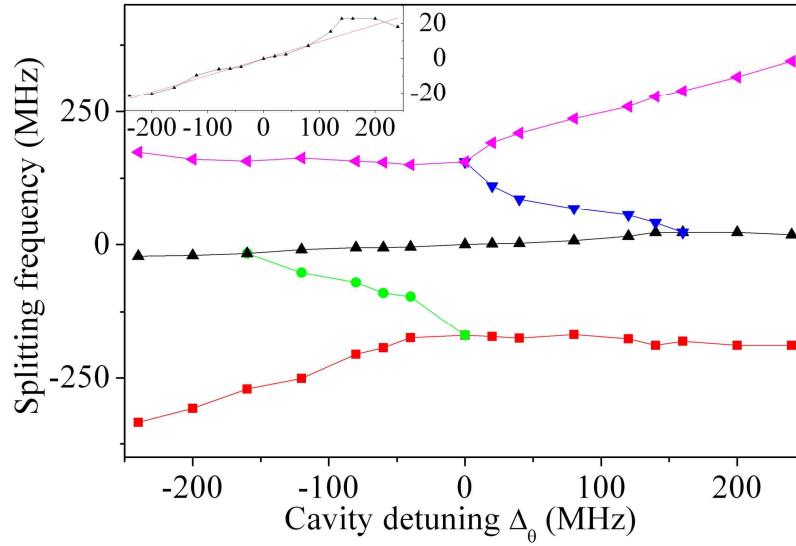


Figure 2.5: Measured positions of the cavity transmission peaks as a function of cavity detuning. The experimental parameters are the same as in Fig. 2.4. Inset: the enlarged display of the center “dark-state polariton” peak.

Figures 2.4(a2)-(g2) present the results of the numerical calculations based on full nonlinear density-matrix equations. In this calculation, unlike in our previous publications [63,69], although the coupling beam is still assumed to be a plane wave, the probe beam (cavity field) is not made of plane-wave approximation. The paraxial wave propagation equation is integrated numerically with the calculated nonlinear susceptibility for many cavity roundtrips, starting from a zero cavity field until it builds up into a steady state. As one can see that the basic features of the experimentally observed spectra showing in Figs. 2.4(a1)-(g1) can be found in the corresponding theoretically simulated curves (Figs. 2.4(a2)-(g2)). However, in spite of the relative sophistication of this calculation, the agreement with the experimental data is still only qualitative, which requires more work to be done on the modeling of this coupled

nonlinear system.

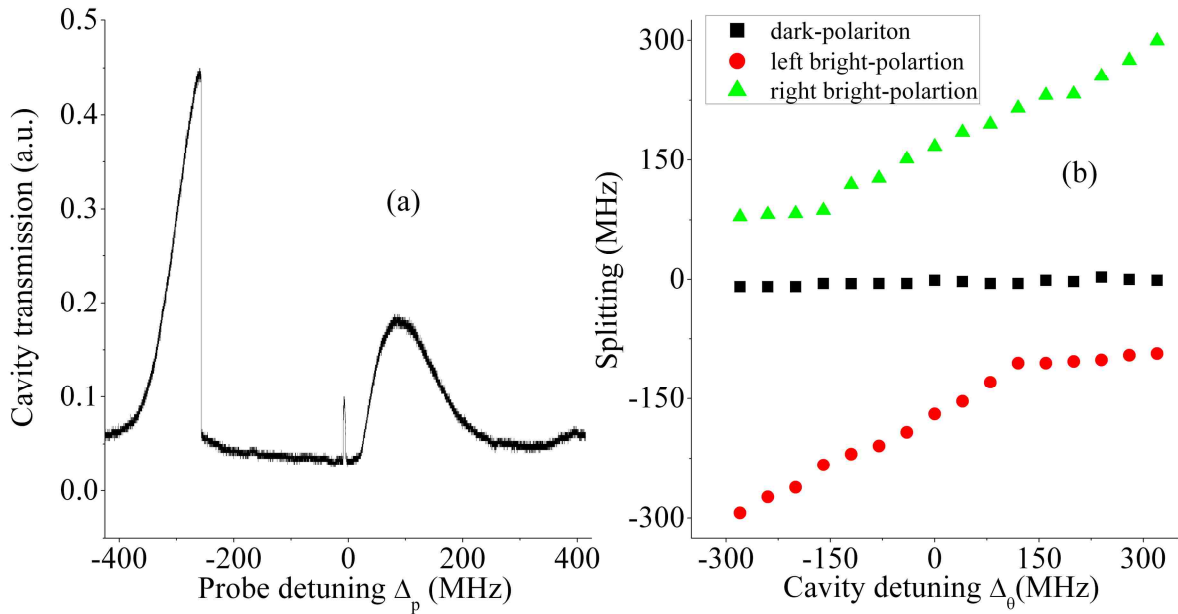


Figure 2.6: (a) Measured cavity transmission spectrum with $\Delta_0 = -200$ MHz. (b) The positions of the polariton peaks as a function of the cavity detuning.

We also consider the cavity detuning case as shown in Fig. 2.1(b). When the detuning line is moved parallelly, the positions of the side peaks move accordingly, resulting in an anti-crossing-like curve. Figure 2.6(a) shows the experimentally measured cavity transmission spectrum at the cavity detuning of $\Delta_0 \approx -200$ MHz, and Fig. 2.6(b) plots the positions of the three peaks as a function of the cavity detuning, which exhibits an anti-crossing-like behavior for the two side (the “bright polariton”) peaks. The other experimental parameters are $T = 84.2$ °C, $P_p = 1.2$ mW, and $P_c = 20.8$ mW. Such anti-crossing behavior can be easily explained as in the coupled two-level atom-cavity systems. One of the main differences between this coupled three-level atom-cavity system and the two-level atom-cavity system is that in such three-level

system, there will always be gaps between the central peak and the two side peaks, which depend on the shape of the dispersion curve of the intracavity medium.

Now, let's examine the case with the coupling frequency detuning. When the coupling detuning is very small, the dispersion curve is slightly shifted in the horizontal direction while the detuning line still passes through the origin. This actually is quite similar to the cavity frequency detuning case, where the dispersion curve is fixed with a moving detuning line. Of course, when the coupling detuning becomes large, the shape of the dispersion curve will change significantly. However, one can qualitatively understand the cavity transmission spectrum even under such condition. Figure 2.7 gives the case for a homogeneously-broadened medium. Since in the homogeneously-broadened case, the value of $|\chi|$ is about 2 orders of magnitude larger than in the inhomogeneously-broadened case, a lower atomic density can be used to simulate the system. Figure 2.7(a) plots the on-resonance case with $\Delta_\theta = 0$ and $\Delta_c = 0$, and Fig. 2.7(b) shows the coupling frequency detuning case with $\Delta_\theta = 0$ and $\Delta_c = 115$ MHz. Although there are five crossing points for the dispersion curve with the detuning line (Fig. 2.7(a)), two of them are always close to the high-absorption positions, as discussed previously. Therefore, as shown in Fig. 2.7(c) only three cavity transmission peaks survived. In Fig. 2.7(b), the cavity is detuned to the right peak position and the dispersion curve is significantly distorted, but one still finds only three peaks in the transmission spectrum (Fig. 2.7(d)) (with two of the five peaks are absorbed), which corresponds to the situation as described in Ref. [71].

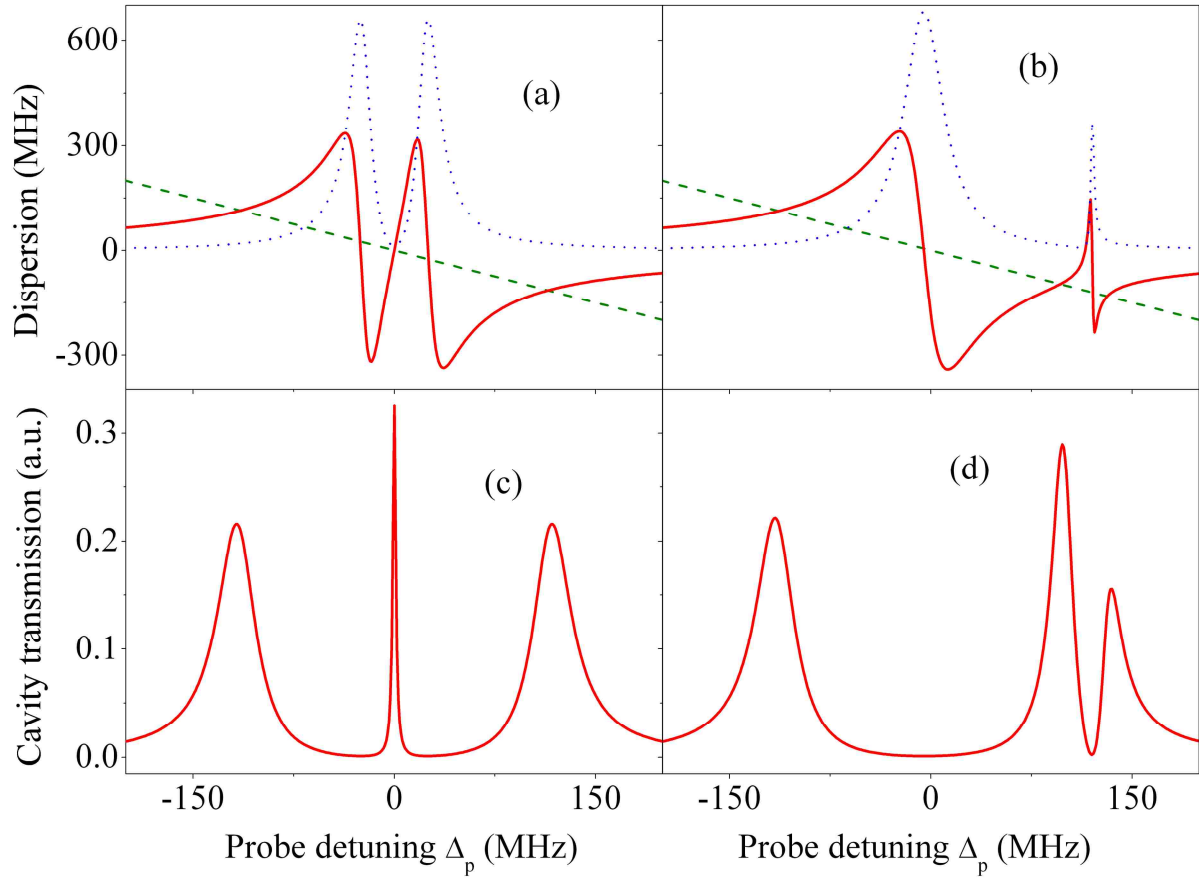


Figure 2.7: Calculated dispersion and cavity transmission curves versus the probe detuning for a three-level homogeneously-broadened medium. (a) and (b): red solid curves show the dispersion plots; blue dotted curves present the absorptions; and green dashed lines show the detuning lines. (c) and (d) are the transmission spectra corresponding to (a) and (b), respectively. The parameters used in the calculation are: $\gamma_{31} = 2\pi \times 3 \text{ MHz}$, $\gamma_{12} = 2\pi \times 0.1 \text{ MHz}$, $\Omega_c = 2\pi \times 8 \text{ MHz}$, $N = 3 \times 10^8 \text{ cm}^{-3}$, and $\Delta_c = 0$ (or $\Delta_c = 115 \text{ MHz}$) for (a) (or (b)).

As opposed to the case shown in Fig. 2.6, Fig. 2.8 presents the experimental results for the coupling frequency detuning case, i.e., $\Delta_\theta = 0$, $\Delta_c \neq 0$. Figure 2.8(a) depicts the cavity

transmission spectrum at the coupling detuning of $\Delta_c = -75$ MHz, and Fig. 2.8(b) presents the positions of the three peaks as a function of the coupling detuning. Again, one can see the anti-crossing-like behavior for the two side peaks. The center peak position changes quasi-linearly with the coupling detuning.

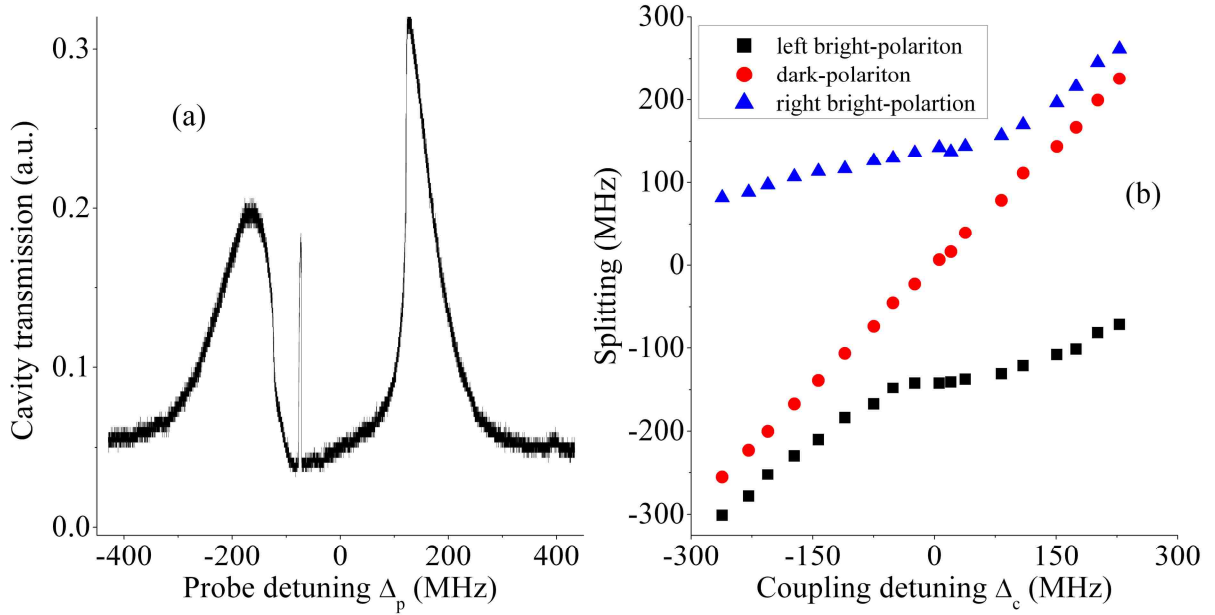


Figure 2.8: (a) Measured cavity transmission spectrum with $\Delta_c = -75$ MHz. (b) The positions of the polariton peaks as a function of the coupling detuning. The experimental parameters are $T = 76.7$ °C, $P_p = 0.5$ mW, $P_c = 7.0$ mW.

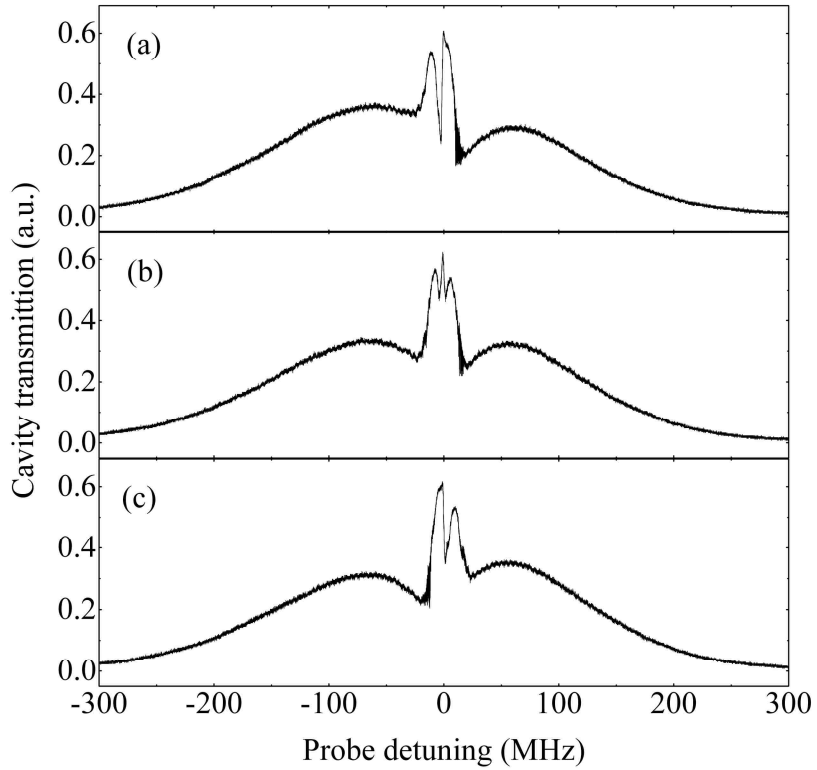


Figure 2.9: Central peak splitting under bad spatial mode overlap case. (a) $\Delta_\theta \approx -5$ MHz. (b) $\Delta_\theta \approx 0$ MHz. (c) $\Delta_\theta \approx 5$ MHz. Other parameters are: $T = 75.1$ °C, $P_p = 1.4$ mW, $P_c = 42.5$ mW.

Finally, let's consider two extreme cases for the three-level atom-cavity system. The first one is called central-peak splitting, as shown in Fig. 2.9. When the overlap between the probe and coupling fields in the intracavity atomic medium is bad, the central peak, i.e. dark-state polariton, becomes broad. Moreover, it splits into two or three peaks. Such abnormal peak structures arise from the complicated dispersion/absorption properties near the atomic resonance, which might result from intracavity spatial mode structure. It could also be caused by the interference between the polariton peaks. The other case happens at the extreme large cavity

detuning, at the middle of two successive modes. Without the coupling field, there is no peak observed when the cavity detuning is fixed at the middle of two modes, as shown in Fig. 2.10(b). However, when the coupling field is applied, four peaks appear, with two central peaks and two broad side peaks, similar to the resonant three-level atom-cavity system case. These phenomena have not been studied in details, and further theoretical modeling is needed to fully understand these interesting effects and their underlying mechanisms.

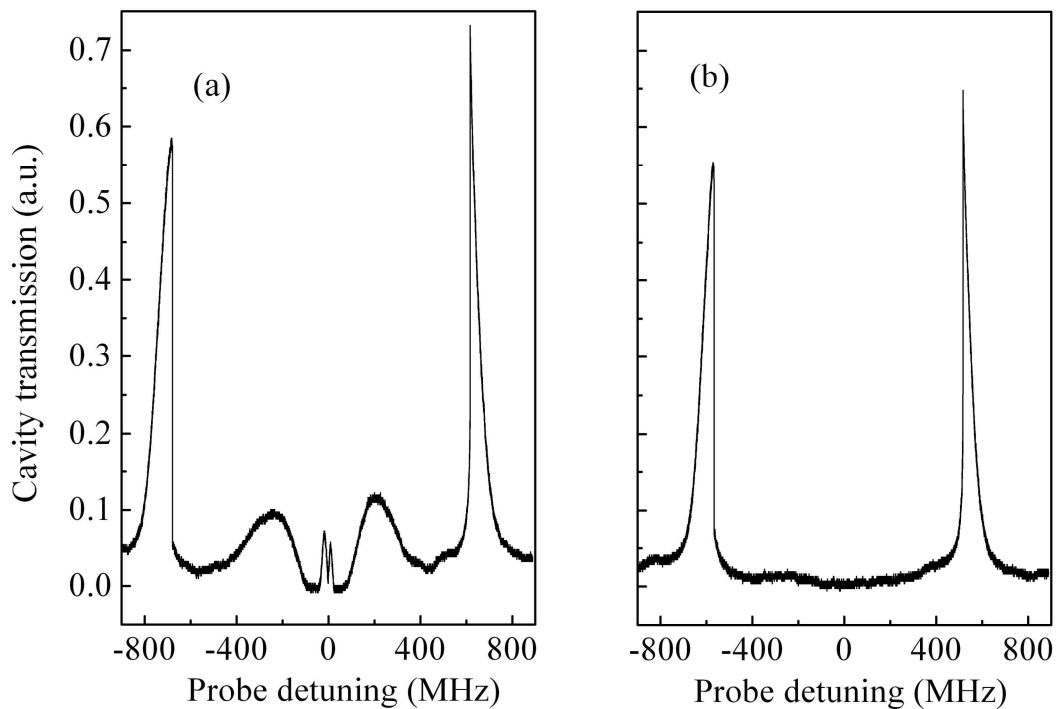


Figure 2.10: (a) With coupling field, $P_c = 27.4$ mW. (b) Without coupling field. Other parameters are: $T = 97.5$ °C, $P_p = 8.67$ mW

2.3 Dressed intracavity dark state in a four-level N-type atom-cavity system

In this section, we consider the system with four-level N-type atoms placed inside an optical

cavity as shown in Fig. 2.11. Without the switching field, the system is the three-level EIT system as discussed in the previous section and we can observe the signature transmission spectrum for the cavity EIT, i.e. a narrow transmission peak at the atomic resonance with two broad side peaks. When the switching field is present, the narrow central peak can be absorbed severely, and then split into two peaks. Such phenomena can be explained in the dressed-state picture and linear-dispersion theory [25]. In addition, an all-optical switch can be realized by utilizing such peculiar feature.

The experimental setup is shown in Fig. 2.11(a). The three-mirror optical ring cavity is the same as the one has been used in the previous section. Four energy levels in the D lines of ^{87}Rb atoms are used for the N-type four-level system, as shown in Fig. 2.11(b). The coupling (ω_c) and switching (ω_s) laser beams are injected separately through two polarization beam splitters (PBS 1 and PBS 2) and counter-propagate through the vapor cell. The probe (ω_p) beam is injected into the cavity via the input mirror M1 and circulates in the cavity as the cavity field, and the output is detected by an APD. The coupling beam co-propagates with the cavity field, and is about 2 degrees misaligned to avoid its circulation in the cavity. The switching beam is carefully aligned to obtain good overlaps with other beams in the vapor cell by monitoring the absorption. The frequency detunings for the probe, coupling, and switching lasers are defined to be $\Delta_p = \omega_p - \omega_{13}$, $\Delta_c = \omega_c - \omega_{23}$, and $\Delta_s = \omega_s - \omega_{24}$, respectively. The radii of the coupling, switching, and probe laser beams are estimated to be 400 μm , 400 μm and 100 μm at the center of the atomic cell, respectively. The temperature of the rubidium cell keeps at about 74°C

during the experiment, which corresponds to an atomic density of $1 \times 10^{12} \text{ cm}^{-3}$. The optical depth (OD) of the probe laser beam is estimated to be about 40 under the current experimental conditions. The empty cavity finesse is about 100. When the atomic cell and the two PBS cubes are included, the cavity finesse decreases down to about 40. The cavity frequency detuning is defined to be $\Delta_\theta = \omega_{\text{cav}} - \omega_{13}$. Figure 2.11(c) is the energy levels in the dressed-state picture when both coupling and switching lasers are on resonance, i.e., $\Delta_c = \Delta_s = 0$.

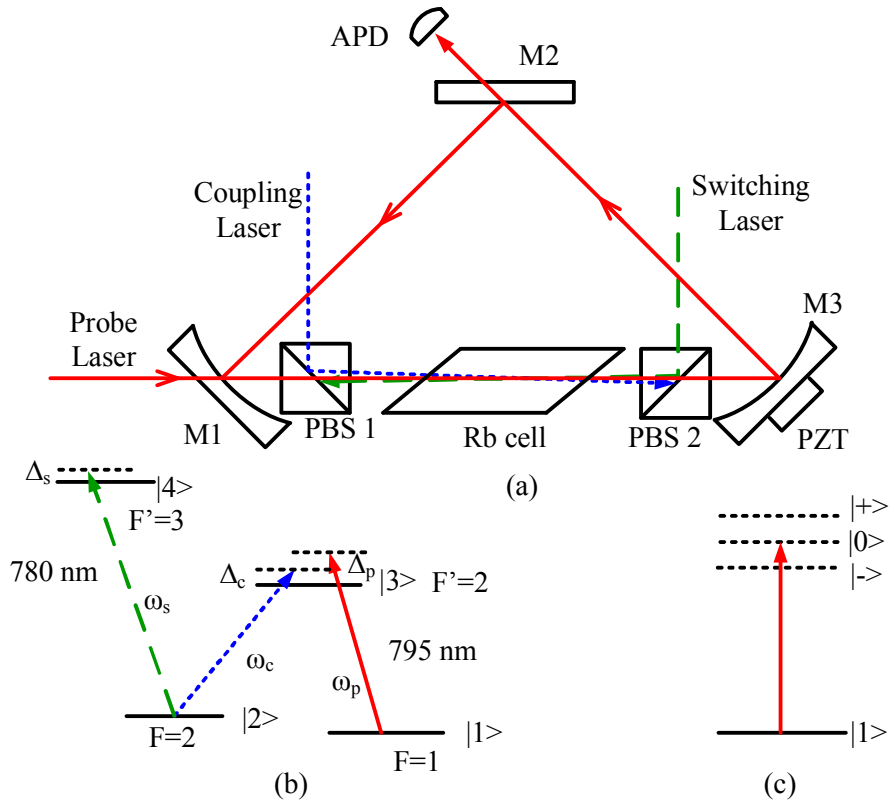


Figure 2.11: (a) Experimental setup. PBS1 & PBS2: polarization beam splitters; M1-M3: cavity mirrors; APD: avalanche photodiode detector; and PZT: piezoelectric transducer. (b) Four-level N-type atomic system in ^{87}Rb and the corresponding laser coupling scheme. (c) Atomic energy levels in the dressed-state picture with both coupling and switching lasers on resonance.

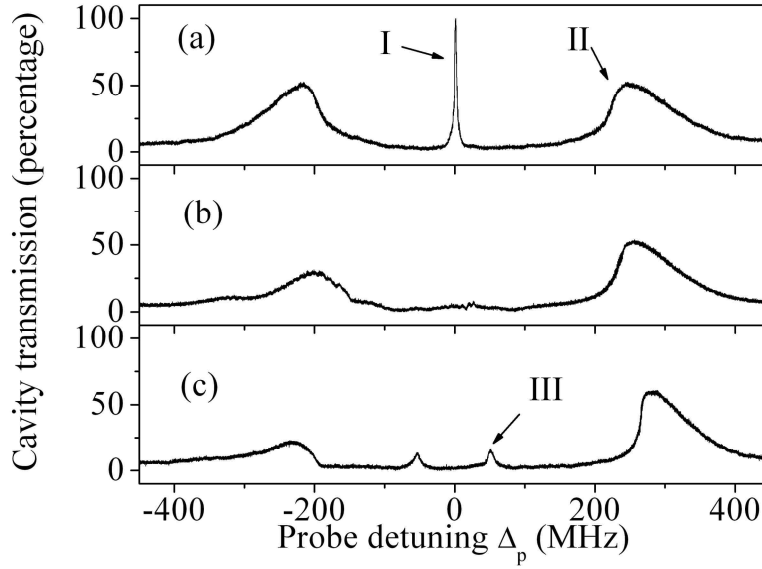


Figure 2.12: Measured cavity transmission spectra versus the probe laser detuning. (a) The switching laser is off. (b) The switching laser is on with $P_s = 0.7$ mW and $\Delta_s = 0$. (c) The switching laser is on with $P_s = 3.3$ mW and $\Delta_s = 0$. Other experimental parameters are $T = 74$ °C, $P_p = 0.5$ mW, $P_c = 13.5$ mW, $\Delta_c = 0$, and $\Delta_\theta = 0$. The cavity transmission is normalized to the central peak height when the switching laser power is zero.

During the experiment, the cavity transmission spectra are measured with and without the switching laser beam when the probe laser frequency is scanning, which are shown in Fig. 2.12. The probe beam power and the coupling beam power are fixed at 0.5 mW and 13.5 mW, respectively. The cavity frequency detuning is fixed at zero, and the coupling and switching lasers are locked on the atomic resonances with the corresponding saturated absorption spectrum, i.e. $\Delta_c = \Delta_s = 0$. In Fig. 2.12(a), one central peak, i.e. the dark-state polariton, can be seen together with two broad side peaks, i.e. the bright polaritons, in the typical three-level

lambda-type EIT atom-cavity system without the switching laser beam [49], as presented in Fig. 2.4(d1) before. When the switching laser is applied, the central peak height will reduce with EIT condition destroyed because of the two-photon absorption [18]. With the increase of switching laser power, the central peak height decreases further until it completely disappears, i.e., totally absorbed, as shown in Fig. 2.13. The situation in Fig. 2.12(b) corresponds to the data point in Fig. 2.13 when the switching laser power is ~ 0.7 mW, where the central peak is totally absorbed. By further increasing the switching laser power, two additional peaks (close to the center) appear, as shown in Fig. 2.12(c), and at the same time the two side peaks move further away from the center. The frequency positions (Δ_p) of the two side peaks depend on the density of the atomic sample (temperature), the coupling laser power, and the switching laser power. When the switching laser power is zero, the positions of the two side peaks are given by Eq. (2.5). When the switching laser power is not zero, the separation between the two side peaks becomes larger, which can be qualitatively understood by considering the change of the refractive property besides the absorption due to the switching beam. As shown in Figs. 2.12(a) and (b), the right side peak moves outward slightly because the switching laser power is relatively weak, while the left side peak shape is modified due to the more complicated energy level structure in the real atomic system, which has not been discussed here.

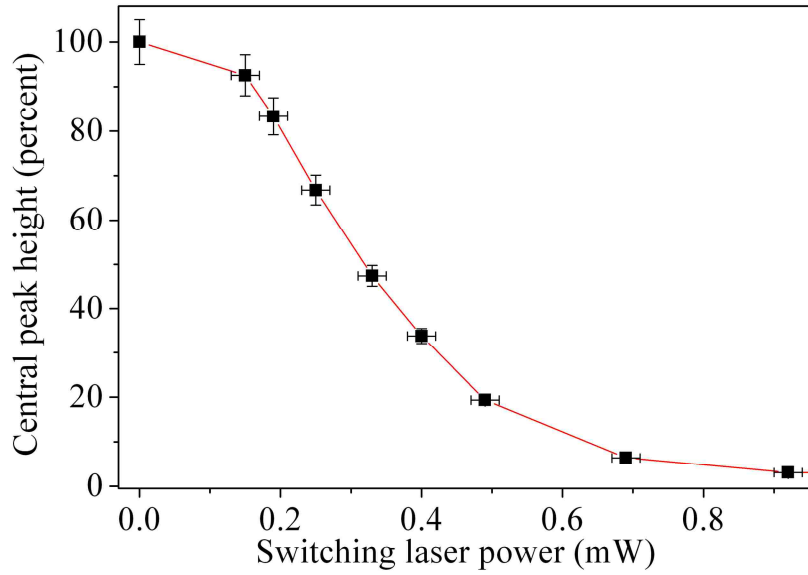


Figure 2.13: Measured central peak heights in the cavity transmission spectra as a function of switching laser power. The central peak heights are normalized to the highest peak when the switching laser power is zero. Other experimental parameters are the same as in Fig. 2.12.

Figure 2.14 shows the absorptive and dispersive switching of the probe laser controlled by a pulsed switching laser, with the coupling laser always on. When the switching laser is turned on and off by an AOM, the switching between different cavity transmission intensities can be made at three different probe frequency positions, marked as I, II, and III, respectively, in Figs. 2.12(a) and (c). Figure 2.14(a) is the switching laser power modulated by a square waveform. Figures 2.14 (b)-(d) show the cavity transmissions as a function of time when the probe frequency is locked onto a Fabry-Perot cavity at $\Delta_p \approx 0$, $\Delta_p \approx 220$ MHz, and $\Delta_p \approx 50$ MHz, corresponding to positions I, II, and III in Figs. 2.12(a) and (c), respectively. Notice that the switching patterns in Figs. 2.14(b) and (c) are out of phase to the one in Fig. 2.14(d), i.e., when

the switching laser is on, the powers shown in Figs. 2.14(b) and (c) (peaks I and II) are also on, while the power shown in Fig. 2.14(d) (peak III) is off.

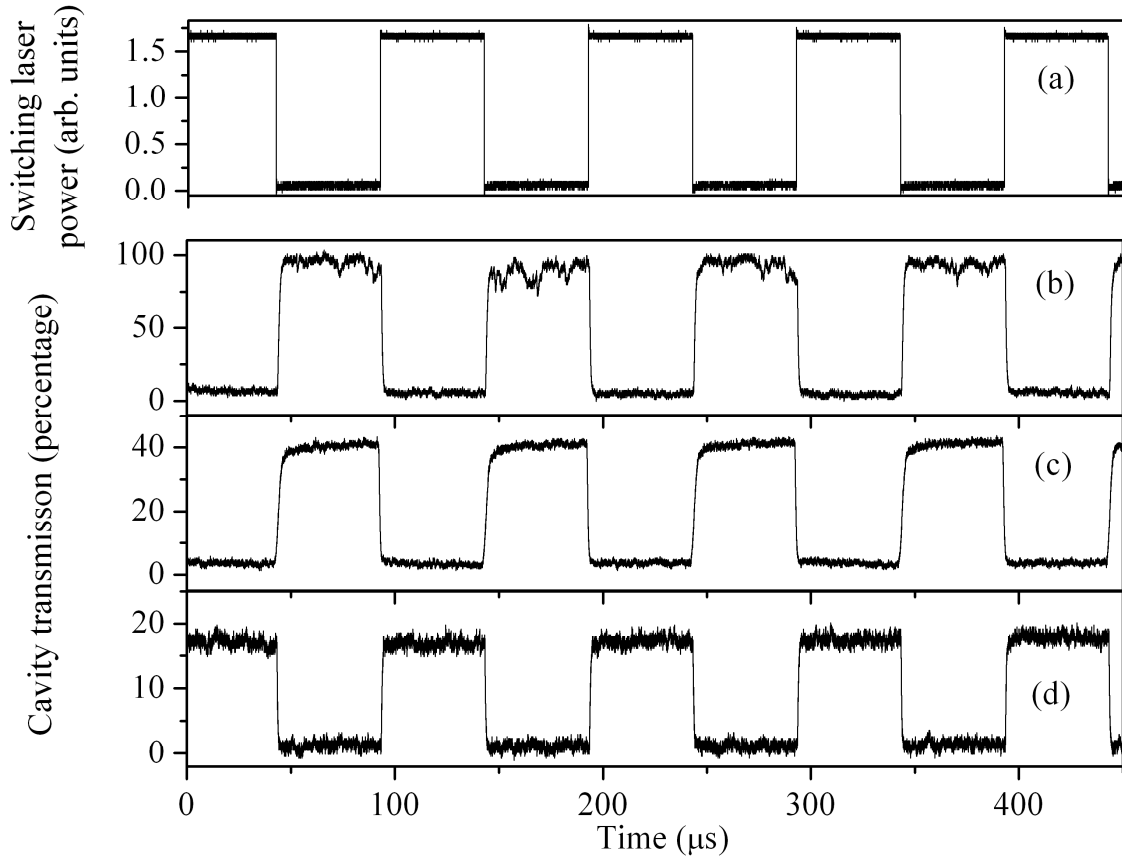


Figure 2.14: All-optical switching of the cavity transmission controlled by the switching laser. (a) The switching laser power as a function of time. (b)-(d) The cavity transmissions as a function of time, with the probe laser frequency fixed at (b) $\Delta_p \approx 0$, (c) $\Delta_p \approx 220$ MHz, and (d) $\Delta_p \approx 50$ MHz, respectively. The cavity transmission is normalized to the central peak height when the switching laser power is zero. Other experimental parameters are the same as in Fig. 2.12.

In order to obtain a stable on-state power shown in Fig. 2.14(b), we used a relatively strong coupling beam (13.5 mW) to get large linewidth of the central peak. In order to reach a good extinction ratio for switching, we also used a relatively strong switching beam (3.3 mW) to observe the obvious shift of the side peaks, as shown in Fig. 2.14(c) and to observe two additional peaks around the center frequency, as shown in Fig. 2.14(d). However, a weak switching beam (0.7 mW) can be used if one needs to make an absorptive switching at the central peak. All the three switchings have the switching speed in the order of 1 μ s (limited by the AOM used in the experiment) and the extinction ratio can reach 20:1 in the current experiment.

The physical mechanism of such switching behaviors can be well understood by considering the combined effects of quantum interference and intracavity dispersion properties. In Fig. 2.12(a), the central peak is usually referred to as the dark-polariton peak and the two side peaks are the bright-polariton peaks, which can be well explained in cavity-QED theory, or as discussed in the previous section. At the weak switching laser power limit, with an increase of the switching laser power, the absorption at the center line increases, the dispersion around the center gradually changes from normal to anomalous. Also, the two anomalous dispersion regions at the two sides resulting from the dressed-states $|+\rangle$ and $|-\rangle$ move away from the center, which leads to the changes of the side peak positions. As shown in Fig. 2.12(b), the central peak is totally absorbed, leaving the two side peaks moving slightly away from the center. By further increasing the switching laser power, the separations between the dressed-states $|+\rangle$ and $|0\rangle$,

and $|0\rangle$ and $|-\rangle$ become even larger. By analyzing the free-space absorption and dispersion behaviors, we find there are two absorption reduced windows around the center due to the destructive interference, and the total dispersion can be understood as the superposition of three dispersive curves. By using the detuning-line method [49] as describe in the previous section, we also find that the cavity round-trip phase is close to zero at the positions where the absorption reduces near the center, thus, we can easily find two additional peaks appearing around the center, as shown in Fig. 2.12(c). Increasing the switching laser power even further, the two peaks around the center, as well as the two side peaks, move further outward. The asymmetry of the two side peaks at high switching laser power results from the hyperfine structure of the D lines.

This four-level N-type atom-cavity system is an extension of the three-level lambda-type EIT atom-cavity system by adding a third (switching) laser beam between one of the ground states to the fourth (excited) level, and the transition between this fourth level ($|4\rangle$) and the other ground state ($|1\rangle$) is forbidden. Therefore, this system has most of the properties as in the three-level EIT system. However, this four-level scheme can be more promising for applications, since it has more flexibility with experimental controls of the parameters, larger enhanced nonlinearities, and both absorption and dispersion properties of the intracavity medium can be dramatically modified. These properties can be useful in studying optical bistability and multistability, as well as in controlled all-optical switching.

2.4 Intracavity dark-state field amplification by four-wave mixing

Besides the four-level N-type atomic system, one can consider a four-level double-lambda system as an intracavity medium. Similar to the N-type system, when the fourth excited level ($|4\rangle$) can be dipole coupled to the ground states $|1\rangle$ and $|2\rangle$, it forms the double-lambda system as shown in Fig. 2.15(b). By utilizing FWM process, we show that the central dark-state peak can be significantly amplified in a four-level double-lambda atom-cavity system. By choosing proper parameters, the dark-state peak intensity can be amplified more than 10 times and the characteristic three-peak structure remains to be unchanged. The amplification is saturated at a relatively high pump laser power, and the dark-state peak position is slightly shifted due to ac-Stark effect induced by the strong pump fields [72].

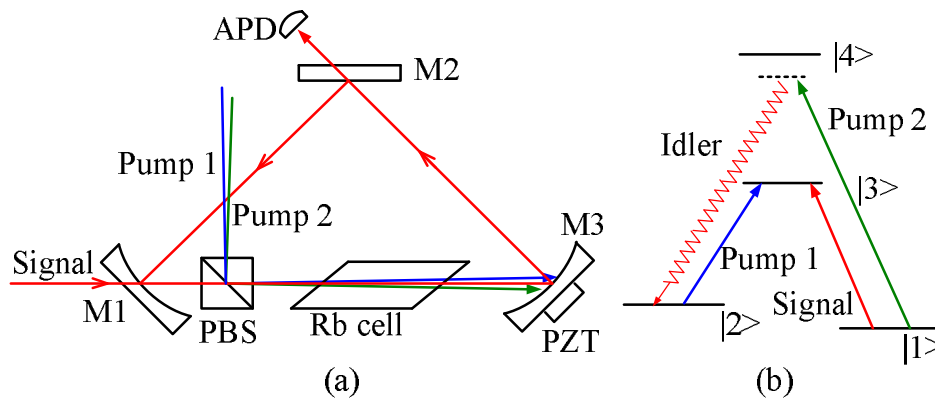


Figure 2.15: (a) Experimental setup. PBS: polarization beam splitter; M1-M3: cavity mirrors; APD: avalanche photodiode detector; and PZT: piezoelectric transducer. (b) The relevant four-level double-lambda atomic system.

The experimental setup is shown in Fig. 2.15(a). The signal, pump-1, and pump-2 laser

beams are from three tunable single-mode diode lasers (Toptica DL 100), respectively, which are current and temperature stabilized. The optical ring cavity is the same as described in the previous sections. The rubidium vapor cell, without buffer gas, is 5 cm long with Brewster windows, and is wrapped in μ -metal sheet for magnetic shielding and in heat tape for stabilizing the temperature at about 81.5 °C (corresponding to an atomic density of about $1.7 \times 10^{12} \text{ cm}^{-3}$) during the experiment. Four energy levels in the D line of ^{87}Rb atom are used to form the double-lambda system, as shown in Fig. 2.15(b). The pump-1 and pump-2 laser beams are injected into the cavity through the polarization beam splitter (PBS) and co-propagate through the vapor cell with about 2 degrees misalignment from the cavity axis to avoid their circulation in the cavity. The signal laser beam is injected into the cavity via the input mirror M1, which serves as the cavity field. The output of the cavity is detected by an APD. The frequency detunings for the signal, pump-1, and pump-2 lasers are defined to be $\Delta_s = \omega_s - \omega_{13}$, $\Delta_{p1} = \omega_{p1} - \omega_{23}$, and $\Delta_{p2} = \omega_{p2} - \omega_{14}$, respectively. The radii of the pump-1, pump-2, and signal laser beams are estimated to be 400 μm , 400 μm and 100 μm at the center of the atomic cell, respectively.

Figure 2.16 shows the cavity transmission spectra under three distinct atomic configurations. When the weak signal laser scans near the $5S_{1/2}, F=1 \rightarrow 5P_{1/2}, F'=2$ transition without the pump beams, a single cavity transmission peak appears, as shown in Fig. 2.16(a), which is similar to the case of an empty cavity transmitted peak with a slightly broadened linewidth owing to the absorption and anomalous dispersion of a two-level atomic system (or can be understood in the weak-coupling regime in cavity-QED theory). By applying an

additional laser (pump-1 laser or coupling in EIT language) on resonance with the $5S_{1/2}$, $F=2 \rightarrow 5P_{1/2}$, $F'=2$ transition, the so-called “cavity EIT” configuration is established, as shown in Fig. 2.16(b), which exhibits the characteristic three-peak structure in the cavity transmission spectrum with one narrow central peak, i.e., dark-state polariton, and two broad side peaks, i.e., bright polaritons [63].

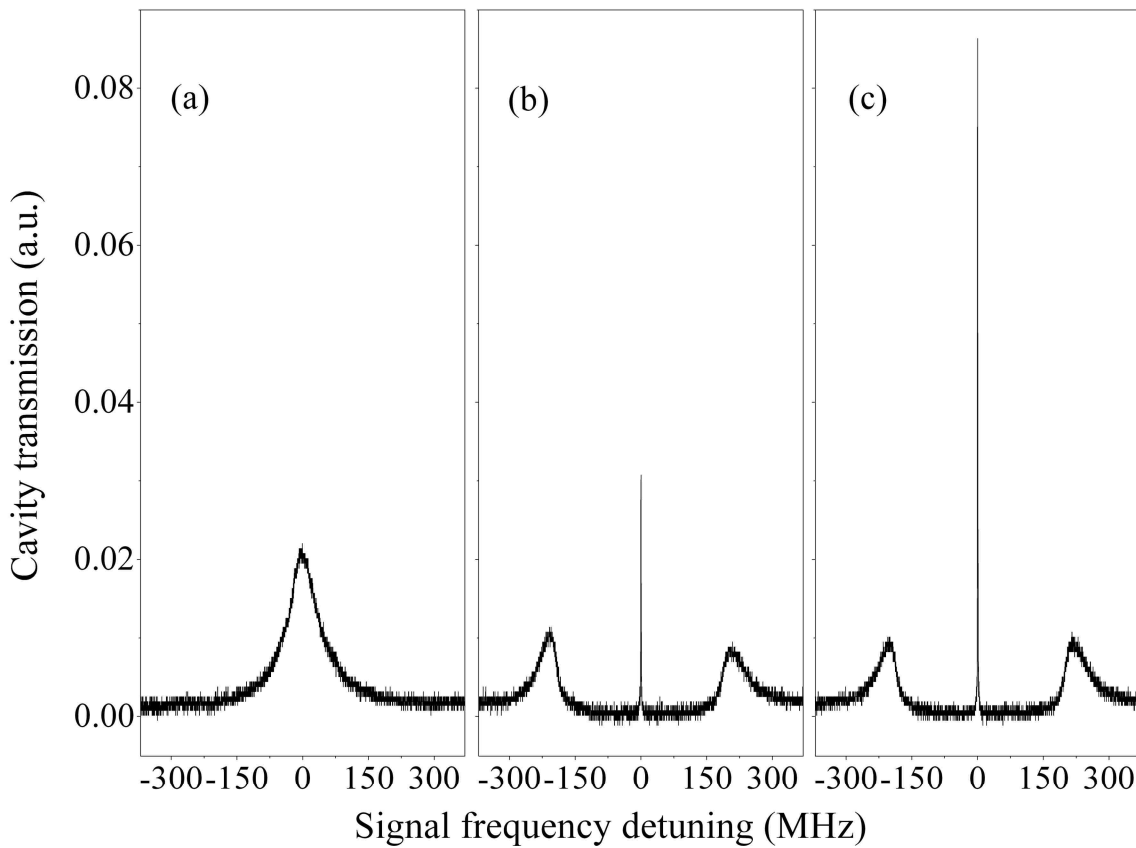


Figure 2.16: Cavity transmission spectra for different atomic systems. The curve in (a) is for the two-level case, (b) is for the three-level case, and (c) is for the four-level double-lambda case with a relatively weak pump-2 laser power.

Such three-peak transmission spectrum has been presented and discussed in the previous sections (Figs. 2.4(d1) and 2.12(a)). Figure 2.16(c) shows the cavity transmission spectrum for the four-level double-lambda atom-cavity system with another relatively weak pump-2 laser ($P_{p2}=1$ mW) applied, which is red detuned (~ 1 GHz) from the $5S_{1/2}, F=1 \rightarrow 5P_{3/2}, F'=1$ transition. The signal laser power for the three cases is fixed at ~ 0.36 mW, and the power of pump-1 laser is fixed at ~ 6.3 mW for Figs. 2.16(b) and (c).

It is clear that the height of the central peak is significantly amplified in Fig. 2.16(c) by comparing with the cavity transmission spectra in Figs. 2.16(b) and (c), while the characteristic three-peak structure does not change significantly with the same two side peaks. To better understand such cavity transmission spectra, theoretical simulation has been carried out to qualitatively compare to the experimental data as shown in Figs. 2.16(b) and (c).

The density-matrix equations for the four-level double-lambda systems under the rotating-wave approximation are given by [10]

$$\begin{aligned}
\dot{\rho}_{22} &= \Gamma_{42}\rho_{44} + \Gamma_{32}\rho_{33} - \Gamma_{21}\rho_{22} + \frac{i}{2}(\rho_{32}\Omega_{p1}^* - \rho_{23}\Omega_{p1} + \rho_{42}\Omega_i^* - \rho_{24}\Omega_i), \\
\dot{\rho}_{33} &= \Gamma_{43}\rho_{44} - \Gamma_{32}\rho_{33} - \Gamma_{31}\rho_{33} + \frac{i}{2}(\rho_{23}\Omega_{p1} - \rho_{32}\Omega_{p1}^* + \rho_{13}\Omega_s - \rho_{31}\Omega_s^*), \\
\dot{\rho}_{44} &= -(\Gamma_{43} + \Gamma_{42} + \Gamma_{41})\rho_{44} + \frac{i}{2}(\rho_{14}\Omega_{p2} - \rho_{41}\Omega_{p2}^* + \rho_{24}\Omega_i - \rho_{42}\Omega_i^*), \\
\dot{\rho}_{21} &= -\tilde{\gamma}_{21}\rho_{21} + \frac{i}{2}\rho_{31}\Omega_{p1}^* - \frac{i}{2}\rho_{24}\Omega_{p2} - \frac{i}{2}\rho_{23}\Omega_s + \frac{i}{2}\rho_{41}\Omega_i^*, \\
\dot{\rho}_{31} &= -\tilde{\gamma}_{31}\rho_{31} + \frac{i}{2}\rho_{21}\Omega_{p1} - \frac{i}{2}\rho_{34}\Omega_{p2} + \frac{i}{2}(\rho_{11} - \rho_{33})\Omega_s, \\
\dot{\rho}_{41} &= -\tilde{\gamma}_{41}\rho_{41} + \frac{i}{2}\rho_{21}\Omega_i - \frac{i}{2}\rho_{43}\Omega_s + \frac{i}{2}(\rho_{11} - \rho_{44})\Omega_{p2}, \\
\dot{\rho}_{32} &= -\tilde{\gamma}_{32}\rho_{32} + \frac{i}{2}(\rho_{22} - \rho_{33})\Omega_{p1} + \frac{i}{2}\rho_{12}\Omega_s - \frac{i}{2}\rho_{34}\Omega_i, \\
\dot{\rho}_{42} &= -\tilde{\gamma}_{42}\rho_{42} - \frac{i}{2}\rho_{43}\Omega_{p1} + \frac{i}{2}\rho_{12}\Omega_{p2} + \frac{i}{2}(\rho_{22} - \rho_{44})\Omega_i, \\
\dot{\rho}_{43} &= -\tilde{\gamma}_{43}\rho_{43} + \frac{i}{2}\rho_{13}\Omega_{p2} - \frac{i}{2}\rho_{42}\Omega_{p1}^* - \frac{i}{2}\rho_{41}\Omega_s^* + \frac{i}{2}\rho_{23}\Omega_i,
\end{aligned} \tag{2.7}$$

where $\Omega_s = \mu_{13}E_s/\hbar$, $\Omega_{p1} = \mu_{23}E_{p1}/\hbar$, $\Omega_{p2} = \mu_{14}E_{p2}/\hbar$, and $\Omega_i = \mu_{24}E_i/\hbar$ are the Rabi frequencies of the signal, pump-1, pump-2, and idler fields, respectively. We write $\tilde{\gamma}_{21} = \gamma_{21} - i(\Delta_s - \Delta_{p1})$, $\tilde{\gamma}_{31} = \gamma_{31} - i\Delta_s$, $\tilde{\gamma}_{41} = \gamma_{41} - i\Delta_{p2}$, $\tilde{\gamma}_{32} = \gamma_{32} - i\Delta_{p1}$, $\tilde{\gamma}_{42} = \gamma_{42} - i(\Delta_{p1} + \Delta_{p2} - \Delta_s)$, and $\tilde{\gamma}_{43} = \gamma_{43} - i(\Delta_{p2} - \Delta_s)$, for simplicity. Γ_{nm} is the natural decay rate between level $|n\rangle$ and level $|m\rangle$; and $\gamma_{nm} = \frac{1}{2}(\Gamma_n + \Gamma_m)$.

In general, the cavity transmission function of the coupled atom-cavity system is given by Eq. (2.3). The susceptibility of the atomic medium can be calculated from the density matrix elements with the expression

$$\chi = \frac{2N\mu_{31}}{\varepsilon_0 E_s} \rho_{31}, \tag{2.8}$$

where N is the atomic density and ϵ_0 is the vacuum permittivity.

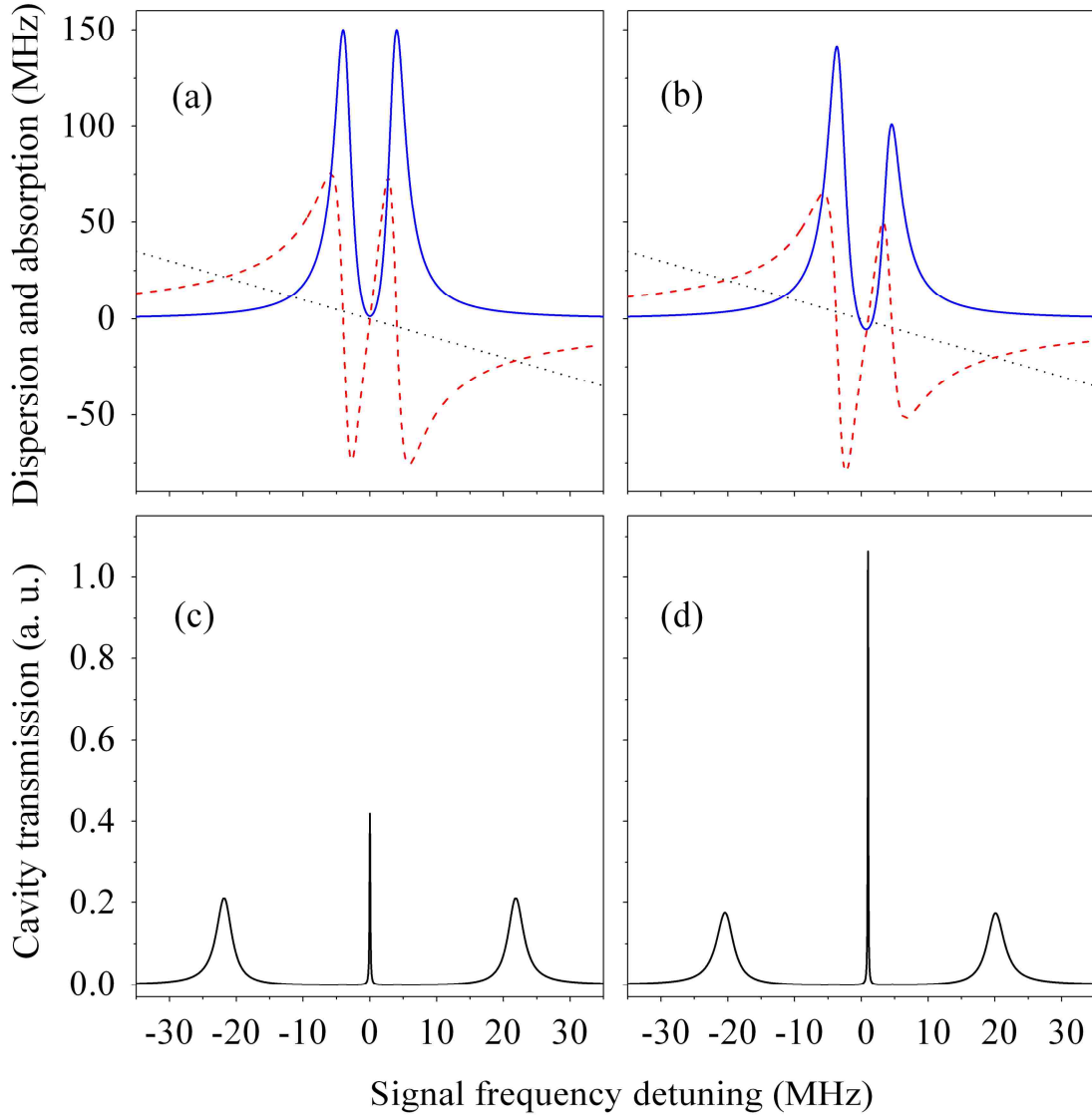


Figure 2.17: Theoretical plots of the dispersion, absorption/gain, and cavity transmission spectra versus signal frequency detuning for three-level lambda and four-level double-lambda systems, respectively. (a, b) present intracavity dispersion curves (dashed red curves), absorption/gain curves (solid blue curves), and detuning lines (dotted dark lines). (c, d) give the

cavity transmission spectra corresponding to three- and four-level systems (corresponding to (a) and (b)), respectively. The parameters used in the calculations are $\Omega_s/2\pi = 0.1$ MHz, $\Omega_{p1}/2\pi = 8$ MHz, and $\Delta_{p1}/2\pi = 0$ MHz, for Figs. 2.17(a) and (c); and $\Omega_s/2\pi = \Omega_i/2\pi = 0.1$ MHz, $\Omega_{p1}/2\pi = 8$ MHz, $\Omega_{p2}/2\pi = 4$ MHz, $\Delta_{p1}/2\pi = 0$ MHz, and $\Delta_{p2}/2\pi = -10$ MHz, for Figs. 2.17(b) and (d), respectively. Other parameters are $\Gamma_{21}/2\pi = \Gamma_{43}/2\pi = 0.1$ MHz, $\Gamma_{31}/2\pi = \Gamma_{41}/2\pi = \Gamma_{32}/2\pi = \Gamma_{42}/2\pi = 3$ MHz, and $N = 3 \times 10^8$ cm⁻³.

By numerically solving Eq. (2.7) under the steady-state conditions, the dispersion and absorption/gain curves, as well as the cavity transmission spectrum can be plotted, as shown in Fig. 2.17. As discussed in Section 2.2, the detuning line, $-\Delta_s$, crosses the dispersion curve, $(\omega_s l/2L)\chi'$, at several places. At each crossing point, $\Delta + (\omega_s l/2L)\chi' = 0$, where the intensity transmission function has its maximum value, corresponding to a peak in the cavity transmission spectrum [49].

Since there are five crossing points, one would expect to observe five peaks under such conditions. However, since there are two large absorption peaks near the resonance, as shown by the solid blue curve in Fig. 2.17(a), at a relatively low signal intensity, the two peaks close to the resonant frequency are severely absorbed, leaving a three-peak structure, as shown in Fig. 2.17(c) [49,63]. In Fig. 2.17(b), the absorption curve becomes negative near the resonant frequency due to the FWM process, which leads to an amplification of the dark-state field, as shown in Fig. 2.17(d). Although phase-matching and wave propagation issues have not been

included in the calculation and only homogeneous case is considered, Figs. 2.17(c) and (d) show good qualitative agreements with Figs. 2.16(b) and (c), respectively,

One can reach the following conclusions by analyzing the intracavity dispersion and absorption/gain properties in Fig. 2.17. First, the FWM process (due to the two pump fields and the signal field) only occurs near the two-photon resonance condition ($\Delta_s - \Delta_{p1} = 0$). Second, the central part of the absorption curve changes from slight absorption to gain when the pump-2 laser is applied. Third, the dispersion curve near the center (resonant frequency) remains to have a sharp normal slope which leads to the slow group velocity and, therefore, the narrowed cavity transmission linewidth [70]. FWM processes in free space with slow light or “stopped light” beams have been observed in several experimental studies [40], which can be attributed to the combination of the gain and sharp normal dispersion. It is worth to point out that typically the cavity transmission spectrum should show two separate peaks when two-level atoms are coupled into an optical cavity under strong coupling condition rather than just one single peak as shown in Fig. 2.16(a). The reason for not seeing such “normal mode splitting” in Fig. 2.16(a) is that the strong coupling condition is not satisfied, i.e., the atomic density and the signal beam intensity are both not high enough under the current experimental condition. To make sure that the observed amplification in Fig. 2.16(c) is indeed due to the FWM process in this double-lambda configuration rather than the Raman amplification in the N-type configuration [27], we checked the spectral components of the central peak by sending the cavity output into a scanning Fabry-Perot interferometer (thorlabs SA210) after fixing the

signal laser frequency on resonance. Although the signal component is dominant (with a ratio of signal to idler of $\sim 4:1$), we have used a narrow band filter (thorlabs FB800) to eliminate the idler beam for the following measurements.

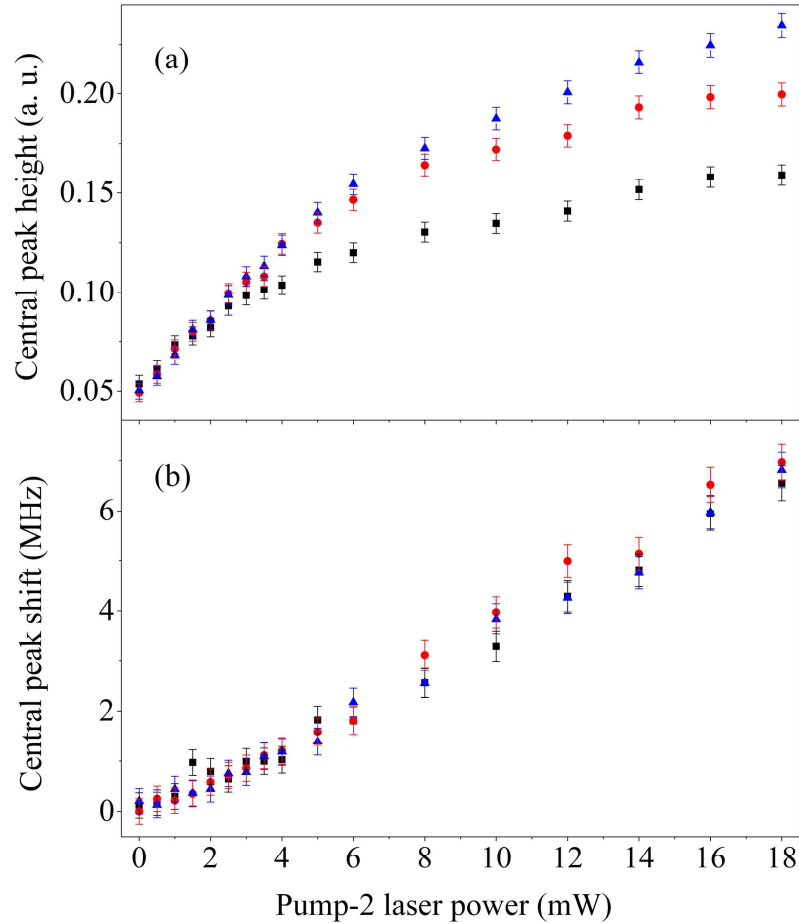


Figure 2.18: (a) and (b) give the measured central peak heights and shifts as a function of the pump-2 laser power, respectively. The black squares, the red circles, and the blue triangles are for the results of different pump-1 laser powers, which are 4.5, 6.3, and 8.3 mW, respectively.

Figures 2.18(a) and (b) present the central peak heights and the central peak shifts versus

the power of the pump-2 laser under three different pump-1 laser powers, respectively. The black squares, the red circles, and the blue triangles represent data taken at the pump-1 laser powers of 4.5, 6.3, and 8.3 mW, respectively. The height of the central peak saturates at a high pump-2 laser power, as shown in Fig. 2.17(a), and different pump-1 laser powers lead to different saturation values.

Moreover, the position of the central peak shifts with the increase of the pump-2 laser power, which is mainly due to the ac-Stark effect. The far detuned pump-2 laser causes the ground state to down shift, which increases the separation between states $|1\rangle$ and $|2\rangle$ (see Fig. 2.15(b)), therefore, the signal laser frequency needs to blue shift in order to satisfy the two-photon resonance condition, where the central peak appears. The situation here is slightly more complicated than the free space case, since when the ground state is down shifted, the cavity field is no longer on resonance, i.e., there is a small cavity detuning relative to the new two-photon resonant frequency. However, owing to the sharp normal dispersion, the central peak shift caused by this small cavity detuning can be neglected comparing to the ground state shift due to ac-Stark effect. By using the detuning line method [49], as described in Section 2.2, the influence of the cavity detuning can be more vividly demonstrated. From Fig. 2.18(a), one can clearly see the difference between different pump-1 laser powers, i.e., higher pump-1 laser power leads to a higher saturation value. Figure 2.18(b) does not give too much information about the relationship between the central peak shift and the pump-1 laser power, since the three lines are quasi-linear and appear to overlap within experimental errors. However, from the

experimental results given below, one will find that these three lines are distinctly different.

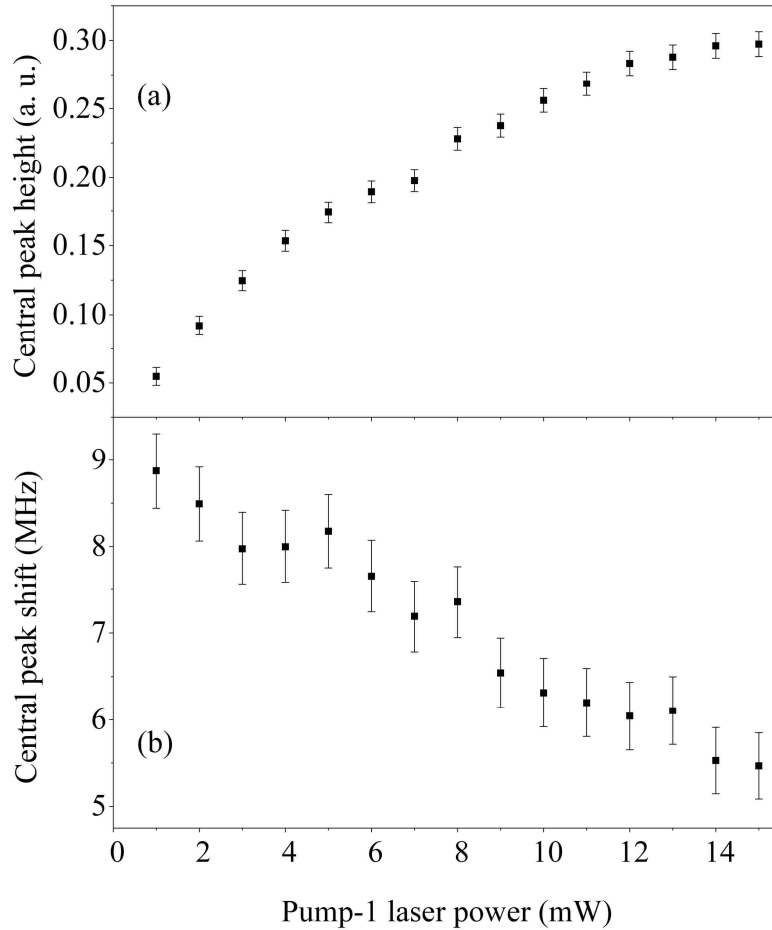


Figure 2.19: (a) and (b) give the measured central peak height and shift, respectively, as a function of the pump-1 laser power with a fixed pump-2 laser power at 20 mW.

To investigate the dependences of the central peak height and the central peak shift on the pump-1 laser power, we fix the pump-2 laser power at ~ 20 mW. By increasing the pump-1 laser power, the central peak height also saturates at a high pump-1 laser power, as shown in Fig. 2.19(a), while the central peak shift decreases (Fig. 2.19(b)). This is caused by the fact that the

resonant pump-1 laser splits the excited state $|3\rangle$, which directly leads to the appearance of EIT due to destructive interference. On the other hand, the ground state $|2\rangle$ is shifted downward by the pump-1 laser, which red-shifts the two-photon resonant condition (with respect to the signal laser frequency). To be precise, at relatively low pump-1 laser power, the slope of the dispersion is not very sharp. In such case, the shift due to the cavity detuning needs to be considered [49].

Although under current experimental conditions, the real amplification of the cavity output comparing to the cavity input for the signal beam has not been realized yet, it is in principle possible to achieve such goal in more sophisticated experiments, which can be more close to the ideal case. Such observation of amplification in the intracavity dark-state field may lead to potential applications in quantum computation and quantum information processing, such as quantum repeaters for quantum networks, and also enrich our fundamental understanding of the cavity-QED effects with multilevel atoms inside optical cavities.

Chapter 3 **Optical multistability and all-optical multistate switching**

3.1 Introduction

When multilevel atoms couple with an optical cavity with relatively high power intracavity field, many interesting phenomena can occur, for example, optical bistability (OB) and optical multistability (OM). OM, which is known as a system to have three or more stable output states for a given input state, has attracted continued interest due to its potential applications in all-optical multistate switching/coding elements. Such multistate switching devices can be used for optical computing, optical communication, and quantum information processing, with an increased channel capacity comparing to the ordinary binary optical switching based on OB [73-77]. OM phenomenon was studied in atomic vapors over 30 years ago under various conditions [78-82]. However, most of those early OM studies were based on polarization switching, which involves two coupled modes (with σ^+ and σ^- polarizations) typically on resonance in the same optical cavity. Recently, similar OM was also theoretically predicted [83] and experimentally realized [84] in the system with semiconductor microcavity polaritons. With the induced atomic coherence [2] in the three-level atomic system, the Kerr nonlinearity can be greatly enhanced near the electromagnetically induced transparency (EIT) resonance [85], which can significantly modify the nonlinear behaviors of the atomic medium inside an optical cavity. In 1996, Harshawardhan and Agarwal theoretically predicted that a control-field-induced OM is possible by using EIT and quantum interferences in a multilevel atomic system [86] rather than using a second cavity field. However, OM based on such mechanism has not been

experimentally demonstrated in previous studies, although OM due to combined absorption and refractive OB effects was experimentally observed in an optical cavity containing multilevel atoms [87].

3.2 Observation of optical multistability in an intracavity three-level atomic system

In this section, we report the first experimental observation of this new type of OM in an optical ring cavity containing three-level lambda-type Doppler-broadened rubidium atoms in a new operating regime from the previously studied OB and OM cases [76,87] (i.e. at a higher temperature and with larger input, as well as control, laser powers). The physical mechanism of this type of OM is that the cavity field experiences higher-order nonlinearities (beyond the third-order Kerr effect) when it passes through the intracavity nonlinear medium, which can be coherently manipulated by a control field, i.e., the coupling field for EIT. In the current system there is only one cavity field, since the control field (not on resonance in the cavity) is only used to prepare the coherent medium and generate large nonlinearity. Such OM curve can be simply viewed as two bistable hysteresis cycles interlacing together with a controllable distance between them. This OM is quite different from the earlier experimental observation by Joshi and Xiao [87], where the observed OM is due to the coexistence of both absorptive and dispersive optical bistabilities at the same time. The great advantage of the OM observed in this new mechanism is its ability for practical applications in multistate switching/coding by adding a pulse sequence to the input (probe) intensity, as was done for the two-state OB case [88].

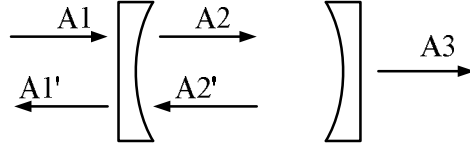


Figure 3.1: OB in the form of a Fabry-Perot cavity containing a nonlinear medium [43].

Since OM is closely related to OB, before introducing the concept for OM, let's quickly see some basic properties regarding OB. There are usually two types of OB, which are known as absorptive and refractive OBs [43,74]. A simple model for realizing absorptive OB is given in Fig. 3.1. The following treatment is adopted from Ref. [43]. Here A_1 denotes the incident field amplitude, A_1' denotes that of the reflected field, A_2 and A_2' denote the forward and backward fields in the cavity, and A_3 denotes the transmitted field amplitude. The cavity boundary conditions about incident and internal fields are in the form of

$$\begin{aligned} A_2 &= A_1 t + A_2' r, \\ A_2' &= r A_2 e^{2ikl - \alpha l}, \end{aligned} \quad (3.1)$$

which yield a relation

$$A_2 = \frac{A_1 t}{1 - r^2 e^{2ikl - \alpha l}}. \quad (3.2)$$

By assuming $R = r^2 e^{2ikl}$, $e^{-\alpha l} \approx 1 - \alpha l$, and $C = \frac{R \alpha l}{1 - R}$, Eq. (3.2) becomes [43]

$$A_2 = \frac{A_1 t}{1 - R(1 - \alpha l)}. \quad (3.3)$$

Here r and t are the amplitude reflection and transmission coefficients, l is the length of the

intracavity medium, and α is the intracavity absorption. Therefore, the intracavity intensity can be obtained as

$$I_2 = |A|^2 = \frac{I_1 T}{[1 - R(1 - \alpha l)]^2} = \frac{I_1}{T(1 + C)^2}. \quad (3.4)$$

Due to the intracavity nonlinear medium, the absorption coefficient α and hence the cooperativity parameter C depend on the intensity of the intracavity field. For simplicity, we consider a saturable absorber (such as a two-level atomic system) and write

$$\alpha = \frac{\alpha_0}{1 + I/I_s}, \quad (3.5)$$

so that

$$C = \frac{C_0}{1 + I/I_s} = \frac{C_0}{1 + 2I_2/I_s}. \quad (3.6)$$

Submitting Eq. (3.6) into Eq. (3.4), we have

$$I_1 = TI_2 \left(1 + \frac{C_0}{1 + 2I_2/I_s}\right)^2 = I_3 \left(1 + \frac{C_0}{1 + 2I_3/TI_s}\right)^2, \quad (3.7)$$

which can be rewritten as

$$\frac{2I_1}{TI_s} = \frac{2I_3}{TI_s} \left(1 + \frac{C_0}{1 + \frac{2I_3}{TI_s}}\right)^2. \quad (3.8)$$

If we define $Y = \frac{2I_1}{TI_s}$ and $X = \frac{2I_3}{TI_s}$ as normalized input and output intensities with T as the transmissivity of the output mirror, respectively, then Eq. (3.8) can be simplified as [43]

$$Y = X\left(1 + \frac{C_0}{1+X}\right)^2. \quad (3.9)$$

The cavity input-output intensity relation of Eq. (3.9) is illustrated in Fig. 3.2 at different values of C_0 (which is critically dependent on the atomic density or number of atoms in the cavity mode). When $C_0 = 0$, the cavity system does not show OB. When C_0 is larger than a critical value, there are two output states corresponding to a given input state, known as OB.

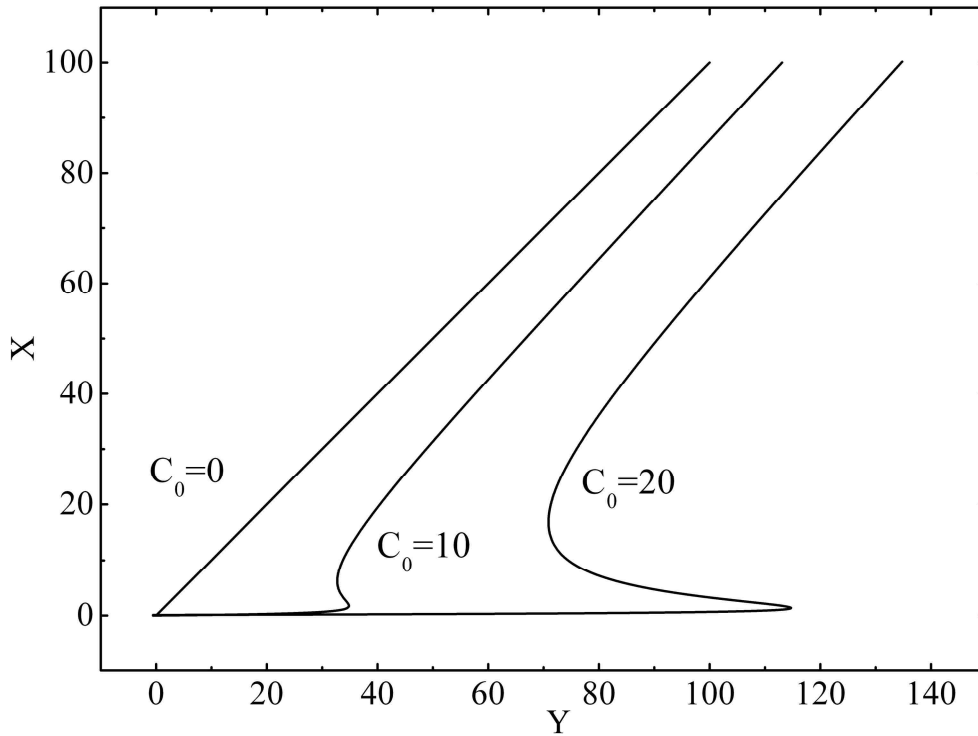


Figure 3.2: The cavity input-output intensity relation [43].

The basic OM phenomenon can be easily analyzed by employing the standard model for OB in a two-level system as given by Bonifacio and Lugiato [89], which was soon extended to different multilevel schemes [90-92]. OB and related effects, such as dynamical instability, stochastic resonance, and chaos, have been extensively studied in our laboratory in the past ten years, and the summary of which is given in Ref. [93]. To illustrate OM, we consider a three-level lambda-type atomic system, as depicted in the inset of Fig. 3.3. The equations for the density-matrix elements under dipole and rotating-wave approximations can be derived by the standard semiclassical model as:

$$\begin{aligned}
\dot{\rho}_{22} &= -\Gamma_{21}\rho_{22} + \Gamma_{32}\rho_{33} + \frac{i}{2}(\rho_{32}\Omega_c^* - \rho_{23}\Omega_c), \\
\dot{\rho}_{33} &= -(\Gamma_{31}\rho_{33} + \Gamma_{32}\rho_{33}) + \frac{i}{2}(\rho_{23}\Omega_c - \rho_{32}\Omega_c^* + \rho_{13}\Omega_p - \rho_{31}\Omega_p^*), \\
\dot{\rho}_{21} &= -\tilde{\gamma}_{21}\rho_{21} + \frac{i}{2}\rho_{31}\Omega_c^* - \frac{i}{2}\rho_{23}\Omega_p, \\
\dot{\rho}_{31} &= -\tilde{\gamma}_{31}\rho_{31} + \frac{i}{2}\rho_{21}\Omega_c + \frac{i}{2}(\rho_{11} - \rho_{33})\Omega_p, \\
\dot{\rho}_{32} &= -\tilde{\gamma}_{32}\rho_{32} + \frac{i}{2}(\rho_{22} - \rho_{33})\Omega_c + \frac{i}{2}\rho_{12}\Omega_p,
\end{aligned} \tag{3.10}$$

where $\Omega_p = \mu_{13}E_p / \hbar$ and $\Omega_c = \mu_{23}E_c / \hbar$ are the Rabi frequencies of the probe and control (coupling) laser beams, respectively. We define $\tilde{\gamma}_{21} = \gamma_{21} - i(\Delta_p - \Delta_c)$, $\tilde{\gamma}_{31} = \gamma_{31} - i\Delta_p$, and $\tilde{\gamma}_{32} = \gamma_{32} - i\Delta_c$. Γ_{nm} is the natural decay rate between level $|n\rangle$ and level $|m\rangle$; and $\gamma_{nm} = \frac{1}{2}(\Gamma_n + \Gamma_m)$. Here, $\Delta_p = \omega_p - \omega_{13}$ and $\Delta_c = \omega_c - \omega_{23}$ are the frequency detunings for the probe and control beams, respectively.

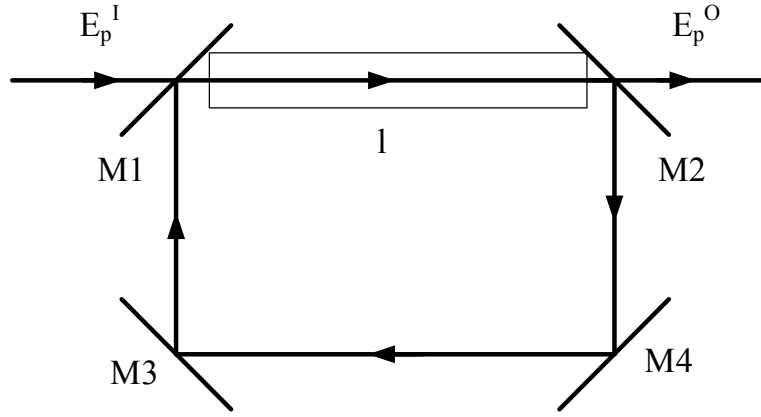


Figure 3.3: Unidirectional ring cavity with an atomic medium of length l [86].

In order to theoretically derive the cavity input-output intensity relation, we consider a unidirectional ring cavity, as shown in Fig. 3.3. Mirrors 3 & 4 have 100 % reflectivity and mirrors 1 & 2 have the reflection and transmission coefficients, R and T , respectively, with $R+T=1$. The following derivations are based on Ref. [86]. The Maxwell's equation for the probe field is

$$\frac{\partial E_p}{\partial z} + \frac{1}{c} \frac{\partial E_p}{\partial t} = i \frac{\omega_p}{2\varepsilon_0 c} P(\omega_p). \quad (3.11)$$

Here, $P(\omega_p)$ is the induced polarization of the intracavity medium. By only considering the steady-state solutions, Eq. (3.11) reduces to

$$\frac{\partial E_p}{\partial z} = i \frac{\omega_p}{2\varepsilon_0 c} P(\omega_p). \quad (3.12)$$

We can also write Eq. (3.12) as

$$E_p(l) - E_p(0) = \frac{\omega_p l}{2\varepsilon_0 c} P(\omega_p). \quad (3.13)$$

The cavity boundary conditions under steady-state limit are given as [86]

$$\begin{aligned} E_p^T &= \sqrt{T} E_p(l), \\ E_p(0) &= \sqrt{T} E_p^T + R e^{-i\delta} E_p(l). \end{aligned} \quad (3.14)$$

By solving Eq. (3.13) together with the cavity boundary conditions given in Eq. (3.14) under the steady-state and mean-field limits [73], the cavity input-output intensity relation can be obtained as:

$$y = \frac{1 - R e^{-i\Delta_\theta}}{T} x - iC \rho_{31}. \quad (3.15)$$

We define the normalized input and intracavity fields as $y = \frac{\mu_{13} E_p^I}{\hbar \sqrt{T}}$ and $x = \frac{\mu_{13} E_p^O}{\hbar \sqrt{T}}$, where

E_p^I (E_p^O) is the input (output) field amplitude. $C = \frac{N \omega_p l \mu_{13}^2}{2 \hbar \varepsilon_0 c T}$ is the cooperativity parameter

defined for OB [73]. N is the atomic density, ε_0 is the vacuum permittivity, and c is the light speed in vacuum. The cavity frequency detuning parameter is defined as $\Delta_\theta = \omega_{cav} - \omega_{13}$.

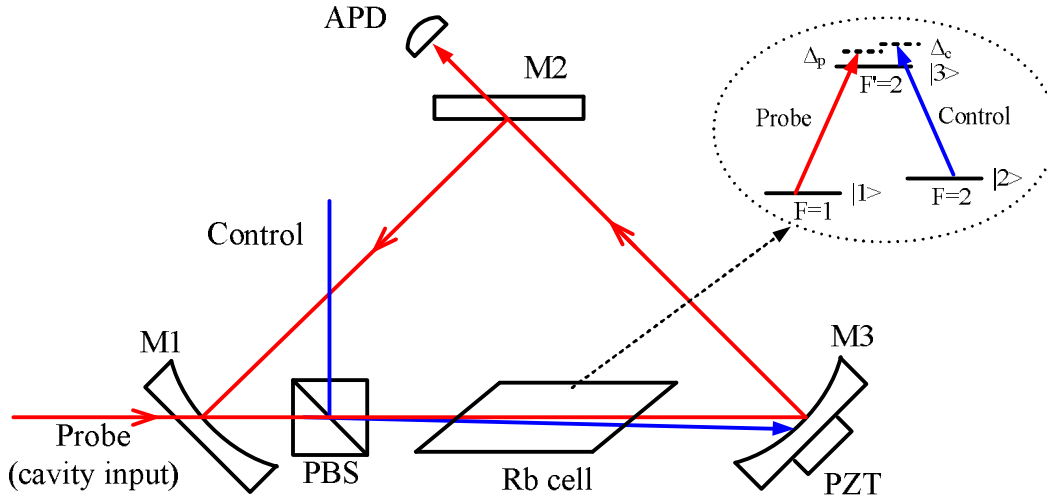


Figure 3.4: Experimental setup. PBS: polarization beam splitter; M1-M3: cavity mirrors; APD: avalanche photodiode detector; and PZT: piezoelectric transducer. Inset: the relevant atomic system.

The experimental setup is shown in Fig. 3.4. The optical ring cavity and the energy levels of ^{87}Rb atoms are the same as used in Section 2.2. The control beam is injected through a PBS, which is not resonant in the cavity. The probe beam is injected into the cavity via the input mirror M1 and circulates in the cavity as the cavity field, and the output is detected by APD. The radii of the control and probe beams are estimated to be $400\ \mu\text{m}$ and $100\ \mu\text{m}$ at the center of the atomic cell, respectively. A third laser is used to lock the cavity (not shown in Fig. 3.4). All three diode lasers are locked to their respective Fabry-Perot cavities. The triangular scan of the cavity input (probe) field is provided by an electro-optical modulator (EOM) before it enters into the cavity [94].

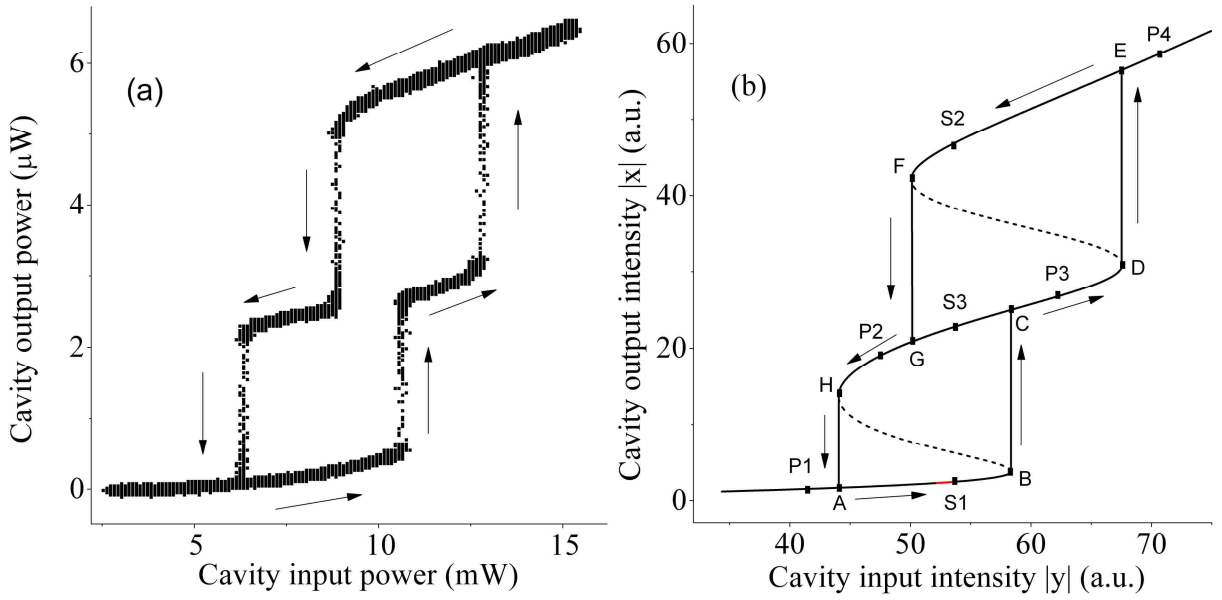


Figure 3.5: (a) Experimentally observed OM curve with $P_c = 15.8$ mW, $\Delta_p/2\pi = -137.7$ MHz, $\Delta_c/2\pi = -227.7$ MHz, $\Delta_\theta/2\pi = 126.6$ MHz, and $T = 105^\circ\text{C}$. (b) Theoretically simulated OM curve using Eqs. (3.10) and (3.15) with appropriate parameters. Arrows indicate the directions of cavity field evolving as the cavity input intensity scans.

A typical OM curve observed in the experiment is shown in Fig. 3.5(a) by carefully adjusting the probe, control, and cavity detunings in certain values at a relatively high temperature ($T = 105^\circ\text{C}$) to give a large enough C value with the probe power P_p scanning triangularly from 0 to 15 mW at a relatively slow rate (100 Hz). Other experimental parameters for Fig. 3.5(a) are control beam power $P_c = 15.8$ mW (the corresponding Rabi frequency is $\Omega_c/2\pi = 131.8$ MHz), $\Delta_p/2\pi = -137.7$ MHz, $\Delta_c/2\pi = -227.7$ MHz, and $\Delta_\theta/2\pi = 126.6$ MHz. Figure 3.5(b) is a theoretically simulated OM curve by numerically solving Eqs. (3.10) and (3.15) together. The key parameters used in the calculation are

$\Omega_c/2\pi = 8$ MHz, $\Delta_p/2\pi = -4$ MHz, $\Delta_c/2\pi = -18$ MHz, $\Delta_\theta/2\pi = 5$ MHz, and $C = 500$.

Here, we have only used the simple homogeneous model and plane waves for all fields to obtain the typical OM curve for a qualitative comparison with the experimental results, which indicates how the intracavity field evolves as the input power scans. In the OB case, the S-type input-output solution gives the bistable hysteresis curve with two stable states in the bistable region, since the middle part of the solution is unstable, the cavity output field jumps up or down at the so-called lower or upper turning (or threshold) point [73]. As shown in Fig. 3.5(b), the input-output solution shows two S-type curves and they interlace together, which gives rise to the tristability in certain input intensity region. By continuously increasing the input field power, the output intensity jumps up to a higher state first at the turning point B and then at the point D (Fig. 3.5(b)), when the input field power is decreased, the output intensity jumps down to a lower state first at the turning point F and then at the point H, which form a typical OM curve “ABCDEFGHA”, as shown in Fig. 3.5(b). In this type of OM, the output intensity can have three stable states, i.e., S1-S3-S2, at one given input intensity. Therefore, it is capable and more convenient to construct multistate switching/coding elements in such an OM system, comparing to other previously demonstrated OM systems [87].

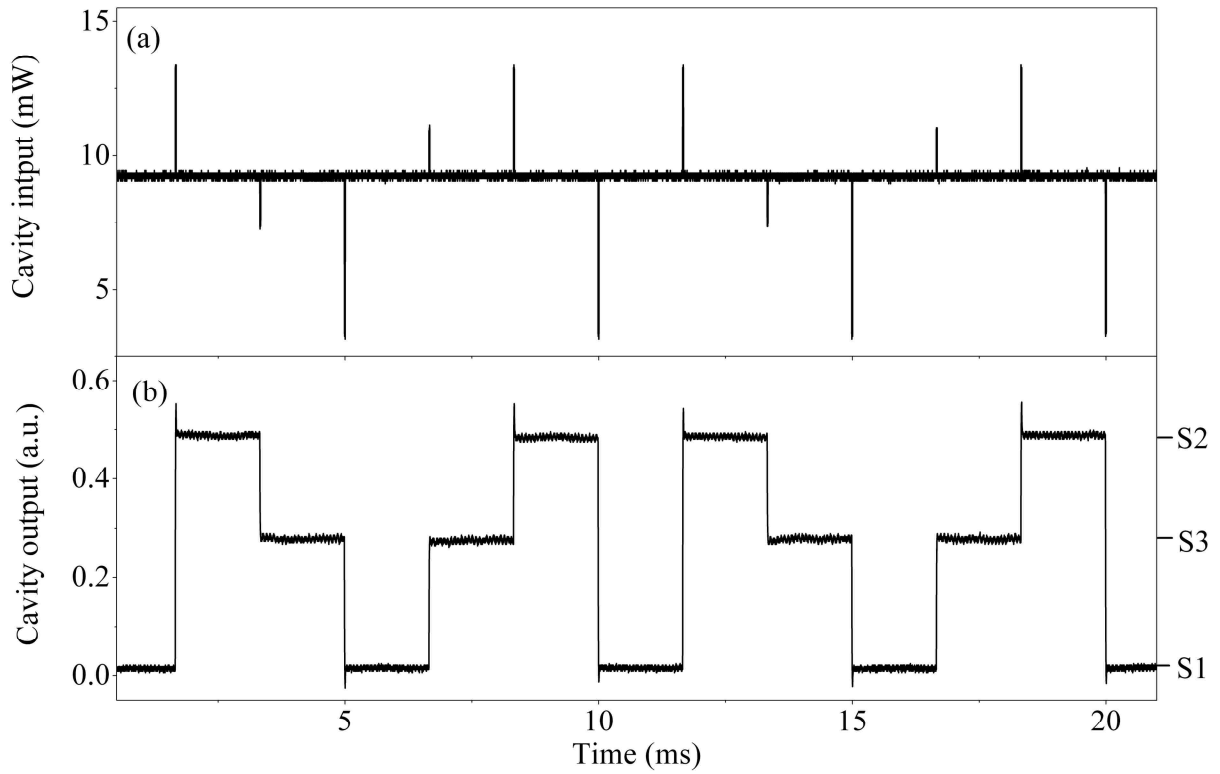


Figure 3.6: Optical multistate switching. (a) Cavity input pulse sequence coded on the EOM. (b) Controlled cavity output intensity with three stable states in responding to the input pulses.

Next, by adding a pulse sequence onto the input (probe) field via the EOM, i.e. modulating input field with instant spikes, we demonstrate that an all-optical multistate switch can be practically realized. We first fix the input power at ~ 9.5 mW under the current experimental conditions, as given in Fig. 3.5(a). Then by utilizing four different pulses (two positive and two negative pulses with different amplitudes as shown in Fig. 3.6(a)), a controllable triple-state switching is demonstrated as shown in Fig. 3.6(b). In Fig. 3.6(b), the initial output is at state 1 (S1), when a large positive pulse is applied, the output field first jumps from S1 to P4 (Fig. 3.5(b)), then it relaxes to the state S2 (upper branch) and stays there as the large pulse ends.

When another small negative pulse turns on, the output field jumps down from S2 to P2 first (Fig. 3.5(b)), then it relaxes and stays at state S3 (middle branch). Accordingly, a large negative pulse switches the output from S3 to S1 when the pulse ends, and a small positive pulse switches the output from S1 to S3, as shown in Fig. 3.6. Obviously, such OM has the capability to switch the cavity output field between any two of the three states by choosing a proper pulse. In such a way, one can code a pulse sequence to perform the desired multistate switchings.

The shape of the OM curve can also be easily controlled by the control laser power, as depicted in Fig. 3.7. When the control beam power is low, the input-output curve is quite monochromatic and single-valued (curve (i) in Fig. 3.7). When the control beam power reaches ~ 8 mW, the curve begins to change significantly (curve (ii)), and the bistability behavior (curve (iii)) shows up at ~ 10.5 mW. As the control beam power is further increased, multistability phenomenon occurs as shown in curve (iv). The typical OM shape (curve (v)) appears when the control beam power reaches to ~ 15.8 mW. As the control beam power increases even further, the OM curve begins to break up into two independent OB curves, and the multistability is gone, as shown in curve (vi) of Fig. 3.7. It is worth to point out that the cavity output curve evolves with different control beam powers as shown in Fig. 3.7 only under the current specially-chosen experimental conditions, since different sets of detuning parameters will lead to different evolution patterns.

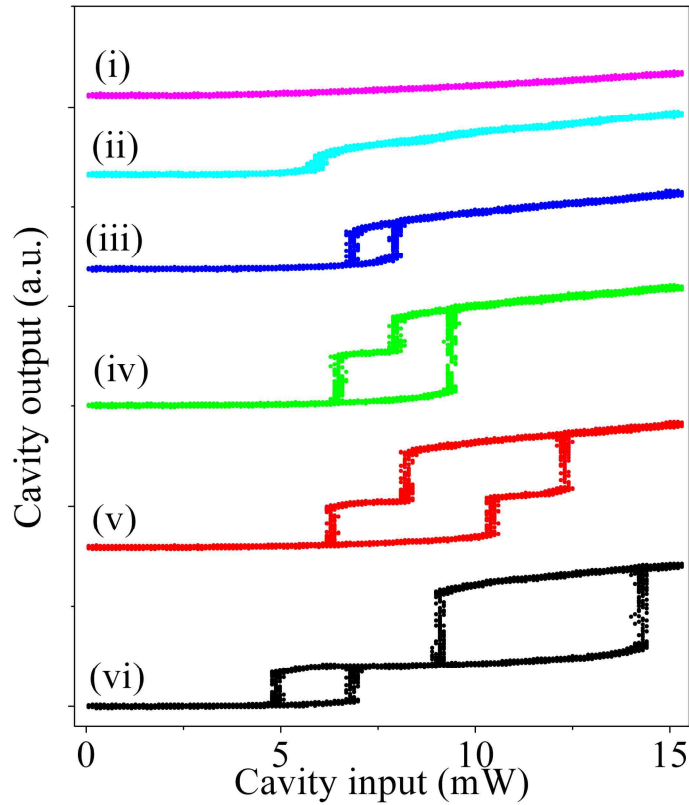


Figure 3.7: Evolution of typical OM curves for different control beam powers of (i) 2.6 mW, (ii) 8.0 mW, (iii) 10.5 mW, (iv) 13.7 mW, (v) 15.8 mW, and (vi) 18.9 mW, respectively. Other experimental parameters are the same as in Fig. 3.5.

To experimentally observe such OM phenomenon in the current system with three-level atoms in a vapor cell inside an optical ring cavity, there are certain conditions needed to be satisfied. First, a high temperature and a large input power scanning range are required. The higher cell temperature leads to a higher atomic density, therefore, higher-order nonlinearities can be made larger, for example, at $T = 105\text{ }^{\circ}\text{C}$, the atomic density can reach $\sim 8 \times 10^{12}\text{ cm}^{-3}$. A large input power scanning range is essential, since if the input power is not scanned to a large enough value, then under certain experimental conditions only part of the OM curve can be

observed. For example, if the cavity input power scans from 0 to 9 mW, then either no bistability or only one bistable loop can be observed at either high or low control beam power as shown in Fig. 3.7 for certain special detuning values. Second, the probe and control frequency detunings should be locked around the point where the Kerr nonlinearity is large and optimal. The observed OM phenomenon is very sensitive to the frequency detuning values. It is worth to point out that the ρ_{31} term in Eq. (3.15) determines the appearance of OM in the experiment. Higher-order nonlinearities enable the multi-stable solutions for Eq. (3.15) at a fixed input intensity (see the discussion about Eq. (19) in Ref. [86]). It was demonstrated that there are two enhanced Kerr nonlinearity peaks (one positive and one negative) around the two-photon resonant center frequency ($\Delta_p = \Delta_c$) due to atomic coherence in such three-level lambda-type system [85]. Therefore, in order to observe OM, it is important to find the large Kerr-nonlinearity points in this system by optimizing several experimental parameters. In principle, the OM curve can be observed with the system at either the positive or negative nonlinear peak. Therefore, the experimental conditions make the system in Fig. 3.5 situate at one of the four parametric regions, i.e. (i) $\Delta_c > 0$, $\Delta_p - \Delta_c > 0$; (ii) $\Delta_c > 0$, $\Delta_p - \Delta_c < 0$; (iii) $\Delta_c < 0$, $\Delta_p - \Delta_c > 0$; and (iv) $\Delta_c < 0$, $\Delta_p - \Delta_c < 0$. However, one needs to avoid wave mixing or Raman processes at certain atomic detunings [41]. Third, after fixing one set of the chosen Δ_p and Δ_c values, we manually scan the cavity detuning Δ_θ until the OM curve occurs. The OM curve is more sensitive to the frequency detunings than to the control beam power. Especially, slight changes on the atomic detunings, i.e., Δ_p and Δ_c , will dramatically modify the OM curve and make it disappear easily. Under certain atomic detunings, four-state

OM curves have also been experimentally observed, which show more complicated behaviors. Although the observed OM curves can be obtained by utilizing the simple homogeneous OB model as given in Eqs. (3.10) and (3.15). For quantitative comparisons between the experimentally observed and theoretically simulated curves, a more comprehensive model is needed to include the considerations of Doppler broadening effect and contributions from multi-Zeeman levels in the atomic system, as well as the spatial beam profiles. Typically, the experimental parameters are much larger than the theoretical ones, such as cooperativity, atomic and cavity detunings, and Rabi frequencies, owing to the Doppler broadening effect, as predicted for dispersive OB in two-level atoms [94].

The observed OM curves can be well controlled by various experimental parameters. Also, such OM possesses a great advancement over the traditional OB, since it is a controllable triple-well system in the potential picture, therefore, one can use it to investigate other interesting effects, such as quantum tunneling between multiple potential wells [95,96]. Other types of OM curves have also been observed during the experiment. For example, the OM curves shown in Figs. 3.8(a) and (b) gives more complex structure compared with the one shown in Fig. 3.5. The OM curves shown in Fig. 3.8 can provide more stable states rather than tri-stable states as shown previously. The physical mechanism for various types of OM curves needs further investigation.

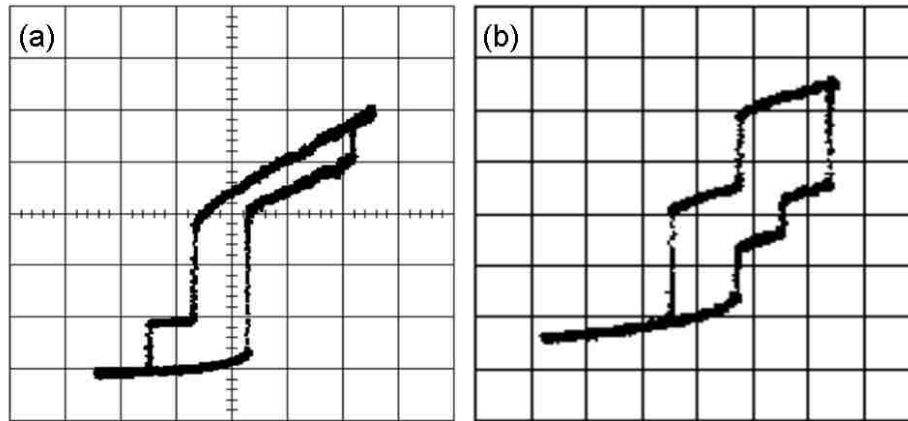


Figure 3.8: Various types of experimental observed OM curves.

3.3 Dual-channel optical multistability and multistate switching

By introducing another optical field, we can realize two outputs with OMs simultaneously on both the signal and the generated Stokes fields in two different output directions of an optical ring cavity containing a hot rubidium vapor cell, as shown in Fig. 3.9. We find that the two OMs, which are governed by different physical processes, are strongly coupled with each other via nonlinear processes in the multilevel atomic medium and have similar threshold behaviors, and therefore, the desired states can be reached at the same time in two output channels. By adding a pulse sequence to the input signal intensity, dual-channel all-optical multistate switchings can be achieved and synchronously controlled, which can be more advantageous in improving the communication capacity [98].

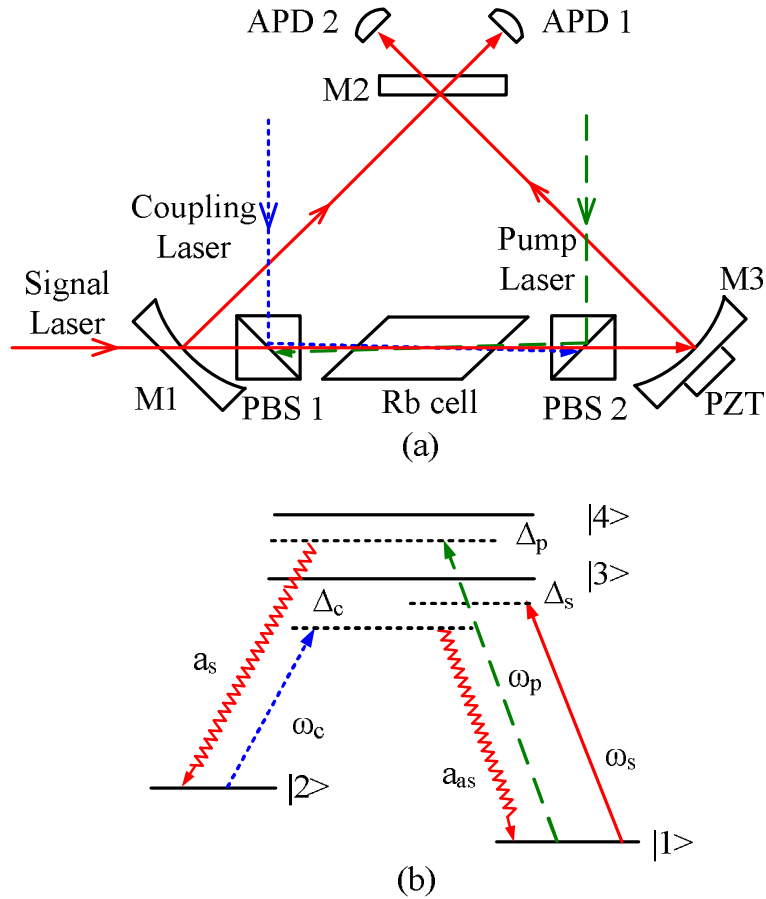


Figure 3.9: (a) Experimental setup. PBS 1 & PBS 2: polarization beam splitters; M1-M3: cavity mirrors; APD 1 & APD 2: avalanche photodiode detectors; PZT: piezoelectric transducer. (b) The relevant four-level atomic system.

The experimental setup is shown in Fig. 3.9(a). The signal, coupling, and pump fields are from single-mode diode lasers (Toptica DL 100) with current and temperature stabilized, which operate at the wavelengths of 795 nm, 795 nm, and 780 nm, respectively. The optical ring cavity is the same as described previously in Section 2.2. The signal field is injected into the cavity via the input mirror M1 and circulates in the cavity as the cavity field. The coupling field is injected through PBS 1 and copropagates with the signal field, while the pump field is injected through

PBS 2 and counter-propagates with the signal field. Both the coupling and pump fields are not on resonance with the cavity. The two outputs of the ring cavity (through M2) are detected by two avalanche photodiode detectors (APD 1 and APD 2). The radii of the signal, coupling, and pump fields are estimated to be 100 μm , 400 μm , and 400 μm at the center of the atomic cell, respectively. The relevant energy-level diagram of ^{87}Rb atoms are shown in Fig. 3.9(b). The signal, coupling, and pump fields drive the transitions $|1\rangle\text{-}|3\rangle$ ($5S_{1/2}, F=1 \rightarrow 5P_{1/2}, F'=2$), $|2\rangle\text{-}|3\rangle$ ($5S_{1/2}, F=2 \rightarrow 5P_{1/2}, F'=2$), and $|1\rangle\text{-}|4\rangle$ ($5S_{1/2}, F=1 \rightarrow 5P_{3/2}, F'=1$) with frequency detunings $\Delta_s = \omega_s - \omega_{13}$, $\Delta_c = \omega_c - \omega_{23}$, and $\Delta_p = \omega_p - \omega_{14}$, respectively.

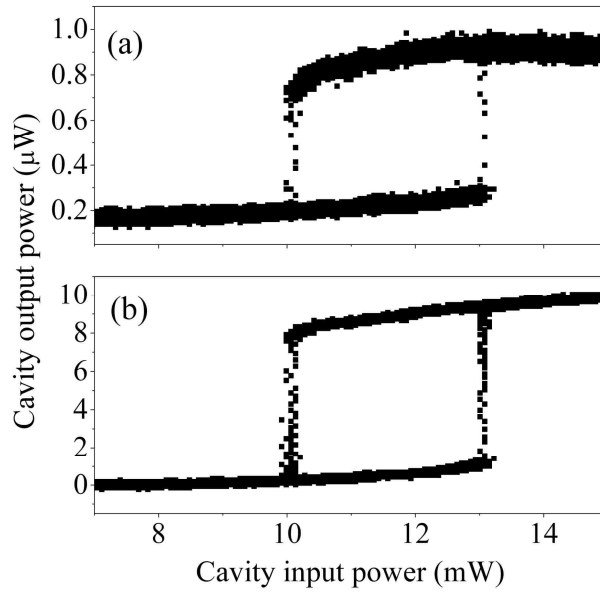


Figure 3.10: Experimentally observed OB curves. (a) and (b) are two cavity outputs as a function of input signal intensity recorded by APD 1 and APD 2, respectively. The experimental parameters are $\Delta_\theta = 154.7$ MHz, $P_c = 19.3$ mW, $P_p = 14.1$ mW, $\Delta_s = -181.1$ MHz, $\Delta_c = -208.4$ MHz, $\Delta_p = -1.2$ GHz, and $T = 103.2$ °C.

Before introducing OM, we would like to first explain the experimental procedure to observe OB, because either OM or OB can be observed in the same experimental setup by carefully choosing different experimental parameters, for example, the laser frequency detunings, the laser intensities, and the cavity frequency detuning. Figures 3.10(a) and (b) show the experimentally observed OB curves from two different outputs of the ring cavity propagating in the opposite direction in the ring cavity as recorded by APD 1 and APD 2. In order to observe two OB curves simultaneously, we first block the pump field, fix the signal and coupling frequency detunings at proper values, and then scan the signal intensity triangularly by an EOM with a relatively slow ramp frequency of ~ 100 Hz, which is similar to the process described in the previous section. A typical OB curve can be observed from APD 2, because OB exists in a broad range of atomic parameter space and is much easier to be observed than OM. Then, the pump field is added, and by tuning the pump frequency detuning and cavity detuning appropriately, two similar OB curves are observed from APD 1 and APD 2 at the same time (Fig. 3.10).

Simultaneous OBs at two outputs in a bidirectional optical ring cavity containing a nonlinear medium have been previously predicted by using the mode coupling theory [98]. Qualitatively speaking, in a Doppler-broadened atomic medium and near the atomic resonance, two counter-propagating cavity modes interact with the same group of atoms, and hence the mode coupling can be quite strong which leads to the possibility of having two OBs for the two cavity modes simultaneously. The physical mechanism in the current work is somewhat

different from the model used in Ref. [98], because the observed two OBs at the two outputs are from two different physical processes, which can be seen from Fig. 3.10(b). When both the coupling and pump fields are applied and counter-propagate through the rubidium cell, bright correlated Stokes and anti-Stokes light beams can be generated under appropriate conditions [41]. The generated Stokes and anti-Stokes fields travel in the same directions as the pump and coupling fields, respectively. The Stokes field output from M2 is detected by APD 1. Since the fourth laser used for cavity locking (injected through M3) has the same propagation direction as the Stokes field, and also comes out from M2, a grating (Thorlabs GH25-18V) is used to spatially separate the Stokes and cavity locking laser fields. Therefore, APD 1 directly measures the first-order beam of the Stokes field, which is $\sim 30\%$ of the original Stokes field immediately out of the cavity. While APD 2 actually measures both the anti-Stokes and the signal fields, and the signal field is dominant (with the anti-Stokes field less than 30%). Under the mean-field limit, the steady-state behavior of the output field is governed by Eq. (3.15). Since the parameters (R , T , Δ_0 , and C) are all fixed to be constants, then the input-output intensity relation is totally determined by the expression of the density-matrix element ρ (ρ is also a function of the intracavity field x). When the signal, coupling, and pump fields are all applied onto the same atomic medium, the density-matrix equations can be really complicated and analytical solutions are difficult to obtain. However, we found that all the density-matrix elements are closely related to the atomic spin coherence term, ρ_{12} [99]. Therefore, we can qualitatively understand that all the cavity outputs are determined by the same atomic spin coherence, which is influenced by all the applied laser fields. Thus it ensures that the cavity

outputs from two different processes (the Stokes field comes from a nonlinear wave-mixing process and the signal field experiences a near-resonance nonlinear process modified by EIT) have the same OB thresholds, as shown in Figs. 3.10(a) and (b). When one intracavity (such as the signal) field changes from low to high, i.e., jumping through the lower threshold of OB, the density-matrix element ρ will then be greatly modified due to nonlinear interaction, and therefore induce a change in the anti-Stokes field.

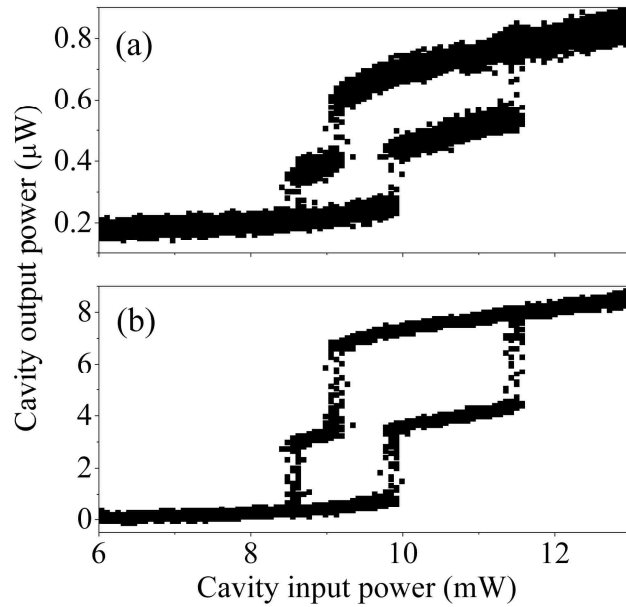


Figure 3.11: Experimentally observed OM curves with $\Delta_0 = 181.7$ MHz. (a) and (b) are two cavity outputs recorded by APD 1 and APD 2, respectively. Other parameters are the same as in Fig. 3.10.

As discussed in the previous section, OM is very sensitive to the atomic parameters. Therefore, it requires even more efforts in order to observe two OM curves simultaneously from

two outputs of the ring cavity by carefully tuning and searching for the appropriate conditions. Figures 3.11(a) and (b) depict the observed OM curves from APD 1 and APD 2, respectively. It is worth to point out that by slightly tuning the cavity detuning, e.g., from 181.7 to 154.7 MHz, the OM curves would be transferred back to OB curves (as shown in Figs. 3.11(a) and (b)). Similarly, the thresholds for both OM curves have basically the same value.

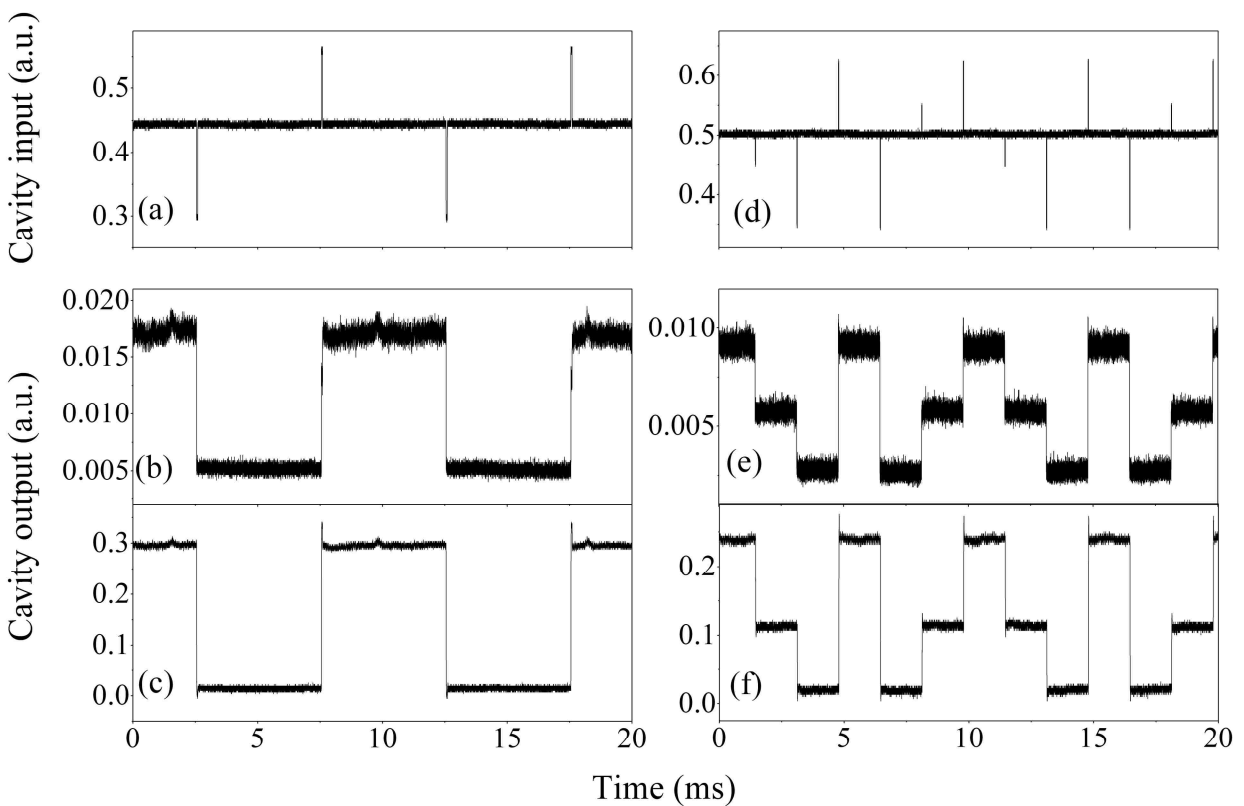


Figure 3.12: All-optical binary (left) and multistate (right) switches. (a) and (d) show the cavity input pulse sequence. (b, c) and (e, f) show the synchronously controlled cavity outputs with two and three stable states for OBs and OMs, respectively.

After the steady OB or OM curves are observed, we fix the signal power in the middle

region of the OB or OM curves and add a pulse sequence onto the input signal field with an EOM and a programmable function generator (Tektronix TDS 2014B). A stable dual-channel all-optical binary or multistate switch can then be practically realized, as shown in Fig. 3.12, which has been extended from the single-channel all-optical switching experiment as presented in the previous section. From Fig. 3.12, one can clearly see that the switches for these two channels can be synchronously controlled by only modulating the input signal intensity. Moreover, the wavelengths of the optical fields in these two output channels are different, one at 780 nm and the other at 795 nm, which might be very useful for the future quantum information networks where different characteristic frequencies might be required for different channels. A practical dual-channel multi-state switch requires that the two outputs can be controlled independently, and therefore nine output combinations are possible (tri-state switch in this section). However, such function is not available under current experimental conditions, which needs further investigation.

Chapter 4 Self-Kerr nonlinearity and optical parametric oscillator

4.1 Modified self-Kerr nonlinearity in an N-type atomic system

One important feature of EIT is its greatly enhanced nonlinearity near atomic resonance with reduced absorption due to quantum interference and atomic coherence [2]. In the past two decades, many resonantly enhanced nonlinear phenomena have been observed in EIT-based media, such as efficient frequency conversion [32], enhanced four- and six-wave mixing processes [100], electromagnetically induced beam focusing [101], elimination of optical filamentation [102], and spatial solitons [103]. The dramatically enhanced self-Kerr nonlinearity [85] and cross-Kerr nonlinearity [104] in three-level EIT systems have been experimentally measured. Although large cross-Kerr nonlinearity in a four-level N-type atomic system was theoretically predicted [17] and experimentally measured [105,106], the self-Kerr nonlinear optical properties of such four-level N-type atomic system have not been investigated so far. In this section, the self-Kerr nonlinearity in the four-level N-type atomic system will be explored. The self-Kerr nonlinear coefficient n_2 is quantitatively measured in such N-type atomic system by utilizing the cavity-scanning technique described in Ref. [85]. We have also developed a theoretical model and obtained analytical solution for the third-order self-Kerr nonlinearity in the N-type system through the iterative method [85] under the weak-probe approximation. Self-Kerr nonlinearities in two-, three- and four-level atomic systems are measured and quantitatively compared in the same experimental setup. Both the value, as well as the sign, of the self-Kerr nonlinear coefficient n_2 and its slope near the atomic resonance can

be altered by simply changing the power of the additional switching field, which can be very useful in the applications of such greatly enhanced nonlinearity with modified absorption and dispersion properties.

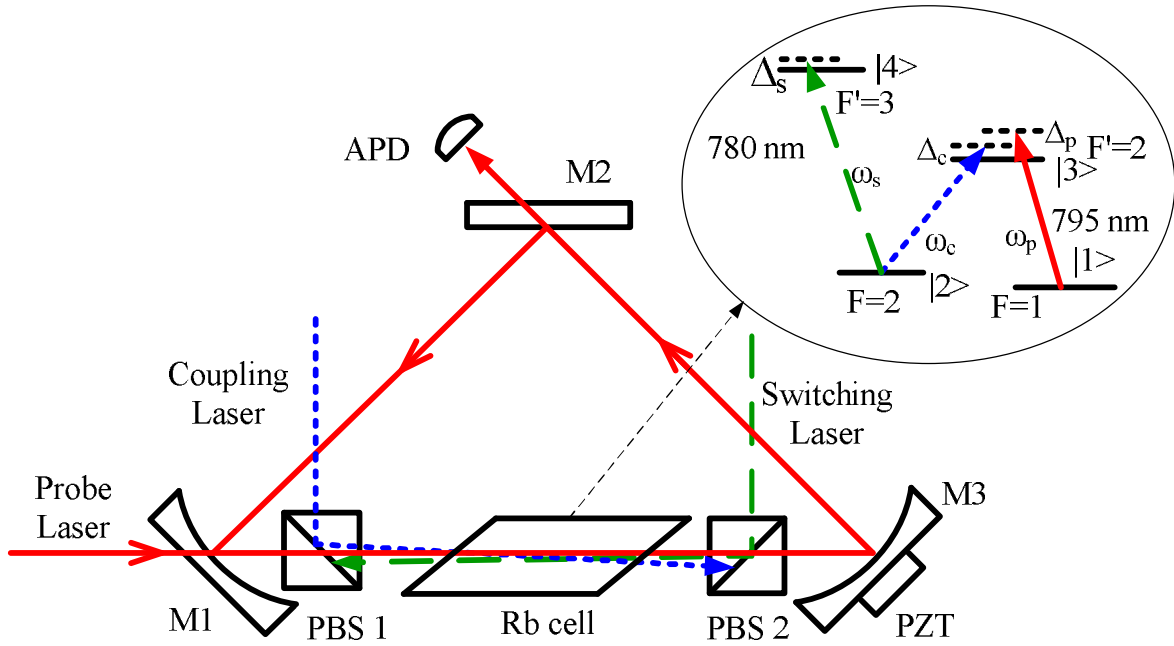


Figure 4.1: Experimental setup. PBS1 & PBS2: polarization beam splitters; M1-M3: cavity mirrors; APD: avalanche photo-diode detector; and PZT: piezoelectric transducer. Bubble: four-level atomic system in ^{87}Rb and laser coupling scheme.

A four-level N-type atomic system is considered in this section, as depicted in the bubble of Fig. 4.1. The density-matrix elements under the rotating-wave approximation can be derived by the standard semiclassical method as [10]

$$\begin{aligned}
\dot{\rho}_{11} &= \Gamma_{21}\rho_{22} + \Gamma_{31}\rho_{33} + \Gamma_{41}\rho_{44} + \frac{i}{2}(\rho_{31}\Omega_p^* - \rho_{13}\Omega_p), \\
\dot{\rho}_{22} &= \Gamma_{42}\rho_{44} + \Gamma_{32}\rho_{33} - \Gamma_{21}\rho_{22} + \frac{i}{2}(\rho_{32}\Omega_c^* - \rho_{23}\Omega_c + \rho_{42}\Omega_s^* - \rho_{24}\Omega_s), \\
\dot{\rho}_{33} &= \Gamma_{43}\rho_{44} - \Gamma_{32}\rho_{33} - \Gamma_{31}\rho_{33} + \frac{i}{2}(\rho_{23}\Omega_c - \rho_{32}\Omega_c^* + \rho_{13}\Omega_p - \rho_{31}\Omega_p^*), \\
\dot{\rho}_{44} &= -(\Gamma_{43} + \Gamma_{42} + \Gamma_{41})\rho_{44} + \frac{i}{2}(\rho_{24}\Omega_s - \rho_{42}\Omega_s^*), \\
\dot{\rho}_{21} &= -\tilde{\gamma}_{21}\rho_{21} - \frac{i}{2}\rho_{23}\Omega_p + \frac{i}{2}\rho_{31}\Omega_c^* + \frac{i}{2}\rho_{41}\Omega_s^*, \\
\dot{\rho}_{31} &= -\tilde{\gamma}_{31}\rho_{31} + \frac{i}{2}\rho_{21}\Omega_c + \frac{i}{2}(\rho_{11} - \rho_{33})\Omega_p, \\
\dot{\rho}_{41} &= -\tilde{\gamma}_{41}\rho_{41} - \frac{i}{2}\rho_{43}\Omega_p + \frac{i}{2}\rho_{21}\Omega_s, \\
\dot{\rho}_{32} &= -\tilde{\gamma}_{32}\rho_{32} + \frac{i}{2}(\rho_{22} - \rho_{33})\Omega_c + \frac{i}{2}\rho_{12}\Omega_p - \frac{i}{2}\rho_{34}\Omega_s, \\
\dot{\rho}_{42} &= -\tilde{\gamma}_{42}\rho_{42} - \frac{i}{2}\rho_{43}\Omega_c + \frac{i}{2}(\rho_{22} - \rho_{44})\Omega_s, \\
\dot{\rho}_{43} &= -\tilde{\gamma}_{43}\rho_{43} + \frac{i}{2}\rho_{23}\Omega_s - \frac{i}{2}\rho_{42}\Omega_c^* - \frac{i}{2}\rho_{41}\Omega_p^*,
\end{aligned} \tag{4.1}$$

where $\Omega_p = \mu_{13}E_p / \hbar$, $\Omega_c = \mu_{23}E_c / \hbar$, and $\Omega_s = \mu_{24}E_s / \hbar$ are the Rabi frequencies of the probe, coupling, and switching lasers, respectively. We define $\tilde{\gamma}_{21} = \gamma_{21} - i(\Delta_p - \Delta_c)$, $\tilde{\gamma}_{31} = \gamma_{31} - i\Delta_p$, $\tilde{\gamma}_{41} = \gamma_{41} - i(\Delta_p - \Delta_c + \Delta_s)$, $\tilde{\gamma}_{32} = \gamma_{32} - i\Delta_c$, $\tilde{\gamma}_{42} = \gamma_{42} - i\Delta_s$, and $\tilde{\gamma}_{43} = \gamma_{43} - i(\Delta_s - \Delta_c)$, for simplicity. Γ_{nm} are the natural decay rates between level $|n\rangle$ and level $|m\rangle$; and $\gamma_{nm} = \frac{1}{2}(\Gamma_n + \Gamma_m) + \gamma_{nm}^{col}$. Here, $\Delta_p = \omega_p - \omega_{13}$, $\Delta_c = \omega_c - \omega_{23}$, and $\Delta_s = \omega_s - \omega_{24}$ are the probe, coupling, and switching frequency detunings, respectively; and γ_{nm}^{col} is the collision-induced dephasing rate.

The standard iterative technique will be used to solve Eq. (4.1) in the steady state, i.e. $\dot{\rho}_{ij} = 0$. The density-matrix elements can be expanded as $\rho_{nm} = \rho_{nm}^{(0)} + \rho_{nm}^{(1)} + \rho_{nm}^{(2)} + \rho_{nm}^{(3)} + \dots$.

Here, we make two assumptions: the first one is that all the populations are in the ground state in the zeroth order, i.e., $\rho_{11}^{(0)} = 1$, $\rho_{22}^{(0)} = \rho_{33}^{(0)} = \rho_{44}^{(0)} = 0$, and the other is that the coupling and the switching fields are much stronger than the probe field, i.e., $\Omega_p \ll \Omega_s, \Omega_c$. Under this weak-probe approximation, the terms with $\rho_{nm}\Omega_p$ ($n \neq m$) can first be neglected in Eq. (4.1). Solving the density-matrix equations for the off-diagonal elements in Eq. (4.1) simultaneously, these off-diagonal density-matrix elements, to the first order, can be obtained to be [24,26]:

$$\begin{aligned}
\rho_{21}^{(1)} &= -\frac{\tilde{\gamma}_{41}\Omega_p\Omega_c^*}{\tilde{\gamma}_{31}|\Omega_s|^2 + \tilde{\gamma}_{41}|\Omega_c|^2 + 4\tilde{\gamma}_{21}\tilde{\gamma}_{31}\tilde{\gamma}_{41}}, \\
\rho_{31}^{(1)} &= \frac{i\Omega_p(|\Omega_s|^2 + 4\tilde{\gamma}_{21}\tilde{\gamma}_{41})}{2(\tilde{\gamma}_{31}|\Omega_s|^2 + \tilde{\gamma}_{41}|\Omega_c|^2 + 4\tilde{\gamma}_{21}\tilde{\gamma}_{31}\tilde{\gamma}_{41})}, \\
\rho_{41}^{(1)} &= -\frac{i\Omega_p\Omega_s\Omega_c^*}{2(\tilde{\gamma}_{31}|\Omega_s|^2 + \tilde{\gamma}_{41}|\Omega_c|^2 + 4\tilde{\gamma}_{21}\tilde{\gamma}_{31}\tilde{\gamma}_{41})}, \\
\rho_{32}^{(1)} &= \rho_{42}^{(1)} = \rho_{43}^{(1)} = 0.
\end{aligned} \tag{4.2}$$

Since in a closed atomic system, the total population is conserved, i.e., $\rho_{11} + \rho_{22} + \rho_{33} + \rho_{44} = 1$, it is straightforward to determine that the second-order diagonal density-matrix elements satisfy the following relationship:

$$\rho_{11}^{(2)} + \rho_{22}^{(2)} + \rho_{33}^{(2)} + \rho_{44}^{(2)} = 0. \tag{4.3}$$

Substituting Eq. (4.2) into the equations of the diagonal density-matrix elements ρ_{nn} in Eq. (4.1), and solving them simultaneously with Eq. (4.3), the diagonal density-matrix elements up to the second order can be obtained to be:

$$\begin{aligned}
\rho_{11}^{(2)} &= -\frac{(\Gamma_{21} + \Gamma_{32}) |\Omega_p|^2}{4\Gamma_{21}(\Gamma_{31} + \Gamma_{32})} \left(\frac{1}{F} + \frac{1}{F^*} \right), \\
\rho_{22}^{(2)} &= \frac{\Gamma_{32} |\Omega_p|^2}{4\Gamma_{21}(\Gamma_{31} + \Gamma_{32})} \left(\frac{1}{F} + \frac{1}{F^*} \right), \\
\rho_{33}^{(2)} &= \frac{|\Omega_p|^2}{4(\Gamma_{31} + \Gamma_{32})} \left(\frac{1}{F} + \frac{1}{F^*} \right), \\
\rho_{44}^{(2)} &= 0,
\end{aligned} \tag{4.4}$$

where $F \equiv \tilde{\gamma}_{31} + \frac{|\Omega_c|^2 / 4}{\tilde{\gamma}_{21} + \frac{|\Omega_s|^2 / 4}{\tilde{\gamma}_{41}}}$.

Substituting Eq. (4.4) into the equations for the off-diagonal density-matrix elements of Eq. (4.1), and solving them again, we can reach the following result:

$$\rho_{31}^{(3)} = -\frac{i\Omega_p |\Omega_p|^2}{8F} \frac{2\Gamma_{21} + \Gamma_{32}}{\Gamma_{21}(\Gamma_{31} + \Gamma_{32})} \left(\frac{1}{F} + \frac{1}{F^*} \right). \tag{4.5}$$

From the definitions of $\chi = \frac{2N\mu_{13}}{\varepsilon_0 E_p} \rho_{31}$, $\chi = \chi^{(1)} + 3|E_p|^2 \chi^{(3)}$, and $n = n_0 + n_2 I$ [43], the

third-order nonlinear susceptibility is obtained as

$$\chi^{(3)} = -\frac{iN |\mu_{13}|^4}{12\varepsilon_0 \hbar^3} \frac{2\Gamma_{21} + \Gamma_{32}}{\Gamma_{21}(\Gamma_{31} + \Gamma_{32})} \frac{1}{F} \left(\frac{1}{F} + \frac{1}{F^*} \right), \tag{4.6}$$

and the self-Kerr nonlinear coefficient n_2 is then given by $\frac{3 \text{Re} \chi^{(3)}}{c\varepsilon_0}$. Here c is the speed of light in vacuum and ε_0 is the vacuum permittivity.

We replace Δ_p , Δ_c , and Δ_s by $\Delta_p + k_p v$, $\Delta_c + k_c v$, and $\Delta_s - k_s v$ owing to the

Doppler broadening effect in an atomic vapor cell [5], then the third-order nonlinear susceptibility in a vapor cell with four-level N-type atomic system is given by

$$\chi^{(3)}(\nu) = \int_{-\infty}^{\infty} -\frac{iN(\nu)|\mu_{13}|^4}{12\varepsilon_0\hbar^3} \frac{2\Gamma_{21} + \Gamma_{32}}{\Gamma_{21}(\Gamma_{31} + \Gamma_{32})} \frac{1}{F(\nu)} \left(\frac{1}{F(\nu)} + \frac{1}{F(\nu)^*} \right) d\nu. \quad (4.7)$$

Here, we will only consider the case where both the coupling and the switching lasers are on resonance ($\Delta_c = \Delta_s = 0$), hence, F is reduced to

$$\begin{aligned} F(\nu) &= \gamma_{31} - i(\Delta_p + k\nu) + \frac{|\Omega_c|^2 / 4}{\gamma_{21} - i((\Delta_p + k\nu) - (\Delta_c + k\nu)) + \frac{|\Omega_s|^2 / 4}{\gamma_{41} - i((\Delta_p + k\nu) - (\Delta_c + k\nu) + (\Delta_s - k\nu))}} \\ &= \gamma_{31} - i(\Delta_p + k\nu) + \frac{|\Omega_c|^2 / 4}{\gamma_{21} - i\Delta_p + \frac{|\Omega_s|^2 / 4}{\gamma_{41} - i(\Delta_p - k\nu)}}, \end{aligned} \quad (4.8)$$

where $k_p \approx k_c \approx k_s \equiv k$ is the wave number of the electromagnetic fields. The atomic speeds obey a Maxwell-Boltzmann distribution, which yields a Gaussian velocity distribution

$$N(\nu) = \frac{N_0}{u\sqrt{\pi}} e^{-\nu^2/u^2}. \quad \text{Here } u/\sqrt{2} \text{ is the root mean square atomic velocity, and}$$

$\Delta\omega_D = 2\sqrt{\ln 2}ku$ is the FWHM of the Doppler width of the thermal atomic distribution. When the switching field Ω_s is switched off, this expression off Eq. (4.8) reduces to the result for three-level lambda system as given in Ref. [85].

The experimental setup is shown in Fig. 4.1. The probe, coupling, and switching lasers are single-mode lasers (Toptica DL 100) with current and temperature stabilized. The optical ring

cavity is the same as illustrated in Section 2.2. Four energy levels in the D line of ^{87}Rb atom are used for the N-type four-level system, as shown in the bubble of Fig. 4.1. The coupling (ω_c) and switching (ω_s) laser beams are injected separately through PBS 1 and PBS 2 and counter-propagate through the vapor cell. The probe (ω_p) beam is injected into the cavity via the input mirror M1 and circulates in the cavity as the cavity field. The output of the cavity is detected by an APD. The coupling beam co-propagates with the cavity field, and has a small misalignment with the cavity axis to avoid its circulation in the cavity. The switching beam is carefully aligned to obtain good overlaps with the other beams in the vapor cell by monitoring the absorption. The radii of the coupling, switching, and probe laser beams are estimated to be $400\ \mu\text{m}$, $400\ \mu\text{m}$ and $100\ \mu\text{m}$ at the center of the atomic vapor cell (5 cm in length), respectively. Both the coupling and switching lasers are locked on the saturated absorption spectrum with $\Delta_c = \Delta_s = 0$ using additional atomic cells. The probe laser is locked onto a Fabry-Perot cavity, and by tuning the applied voltage on the PZT of the Fabry-Perot cavity, the probe laser frequency can be easily detuned within a range of several hundred megahertz. With another Fabry-Perot cavity and the saturated absorption spectrum, the exact value of the probe frequency detuning can be determined.

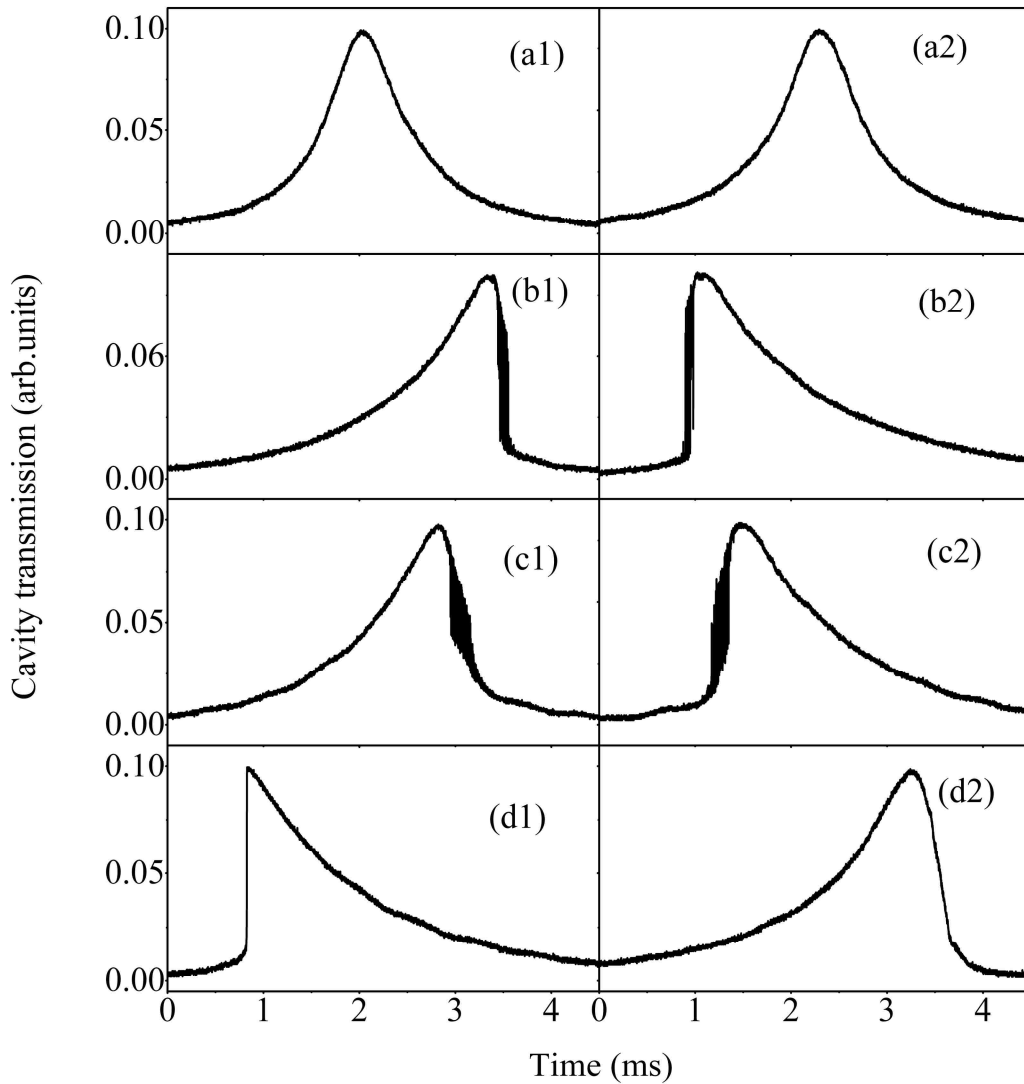


Figure 4.2: Cavity transmissions with the scan of the cavity length. (a1) and (a2) are for the two-level case with the coupling and switching beams turned off; (b1) and (b2) are for the three-level lambda-type case with only the switching beam turned off; (c1) and (c2) are for the four-level N-type case with a relatively weak switching laser beam; and (d1) and (d2) are for the same four-level case with a relatively strong switching laser beam.

When the probe beam is tuned far from the atomic resonances, the atoms act as a linear intracavity medium, the cavity transmission spectrum shows a typical symmetric Lorentzian shape by scanning the ring cavity length. As the probe (cavity) field is tuned to near the atomic resonance, the cavity transmission profile turns to be asymmetric in shape owing to the self-Kerr nonlinear coefficient n_2 , and the degree of such asymmetry can be used to directly measure the Kerr nonlinearity [85]. Figure 4.2 shows the cavity transmission spectra under several different experimental conditions. Figures 4.2(a1) and (a2) are for the two-level case with the coupling and switching laser beams turned off ($P_c = P_s = 0$). Figures 4.2(b1) and (b2) are for the three-level lambda-type case with only the switching beam turned off ($P_c = 13.3$ mW, $P_s = 0$). Figures 4.2(c1) and (c2) are for the four-level N-type case with a relatively weak switching laser beam ($P_c = 13.3$ mW, $P_s = 0.4$ mW) and Figs. 4.2(d1) and (d2) are for the four-level N-type case with a relatively strong switching laser beam ($P_c = 13.3$ mW, $P_s = 2.7$ mW). Other experimental parameters are $T = 66$ °C and $\Delta_c = \Delta_s = 0$. The left and right columns of Fig. 4.2 correspond to the situations when the probe detuning is set at $\Delta_p/2\pi = 14$ and -14 MHz, respectively.

If n_2 is negative, then as the cavity length scanning from shorter to longer, the left part of the peak becomes more gradual, while the right part of the peak becomes steeper, as shown in Fig. 4.2(b1). The opposite is true when the value of n_2 is positive. The self-Kerr nonlinear coefficient n_2 can be directly determined by the degree of asymmetry ($\Delta = t_1 + t_2 - 2t_p$) of the

peak as $n_2 = \frac{\lambda\Delta}{\tau I_p l}$ [85]. Here, λ is the wavelength, τ is the time period between two successive

transmission peaks, I_p is the peak intensity, l is the length of the rubidium cell, and t_1 & t_2 are the times on two sides of its peak at which the output intensity is half of the peak intensity, respectively. Therefore, one can see that from Fig. 4.2 when $\Delta_p/2\pi = 14$ MHz, n_2 is very small in the two-level case as indicated by its almost symmetric transmission peak (Fig. 4.2(a1)); n_2 has a negative value when the coupling beam is applied (Fig. 4.2(b1)); the absolute value of n_2 decreases (i.e. a smaller negative value) when a weak switching beam is applied (Fig. 4.2(c1)) due to the decrease in the degree of the asymmetry; and n_2 changes sign when a strong switching beam is applied (Fig. 4.2(d1)). Similar discussions can be made for Figs. 4.2(a2)-(d2) with the sign of n_2 switched from corresponding Figs. 4.2(a1)-(d1). During the experimental measurements under different conditions, the intracavity peak power has been kept at about 50 μ W ($\Omega_p \approx 2\pi \times 10$ MHz) by adjusting the input probe laser power to compensate for the changes in absorption under different laser beam configurations and powers, therefore, the direct comparison for the nonlinear coefficients between different energy level systems become meaningful.

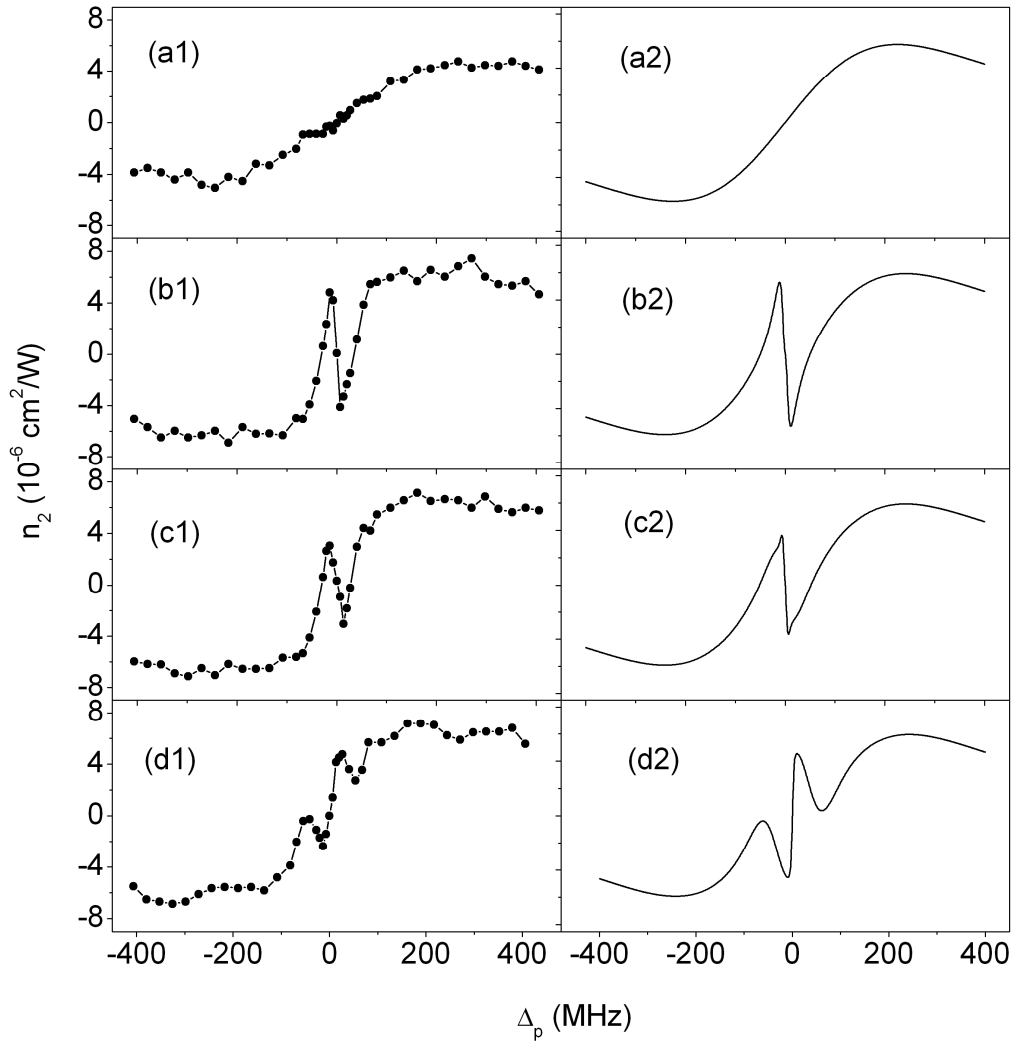


Figure 4.3: Self-Kerr nonlinear coefficients n_2 versus probe frequency detuning for different atomic systems. The left column presents the experimentally measured results and the right column gives the corresponding theoretically calculated curves. (a1)&(a2) are for the two-level case; (b1)&(b2) are for the three-level lambda-type case; (c1)&(c2) are for the four-level N-type case at a relatively small switching laser power; and (d1)&(d2) are for the same four-level case at a relatively strong switching laser power.

Figure 4.3 shows both the experimentally measured and theoretically calculated self-Kerr nonlinear coefficients n_2 versus the probe frequency detuning for different atomic energy level configurations. Each data point on curves shown in Figs. 4.3(a1)-(d1) corresponds to a value deduced from a spectrum curve from Figs. 4.2(a1)-(d1) (or Figs. 4.2(a2)-(d2)). The theoretical simulations are carried out according to Eq. 4.7 including the Doppler broadening effect. The key parameters in the experiments are (a1) $P_c = P_s = 0$; (b1) $P_c = 13.3$ mW ($\Omega_c \approx 2\pi \times 120$ MHz), $P_s = 0$; (c1) $P_c = 13.3$ mW, $P_s = 0.4$ mW ($\Omega_s \approx 2\pi \times 35$ MHz); (d1) $P_c = 13.3$ mW, $P_s = 2.7$ mW ($\Omega_s \approx 2\pi \times 91$ MHz). The frequency detunings for the coupling and switching beams are kept zeros. The parameters used in the calculations are $\gamma_{21} = 2\pi \times 1$ MHz, $\gamma_{31} = \gamma_{41} = 2\pi \times 130$ MHz, $\Delta\omega_D = 2\pi \times 540$ MHz with (a2) $\Omega_c = \Omega_s = 0$; (b2) $\Omega_c = 2\pi \times 100$ MHz, $\Omega_s = 0$; (c2) $\Omega_c = 2\pi \times 100$ MHz, $\Omega_s = 2\pi \times 35$ MHz; and (d2) $\Omega_c = 2\pi \times 100$ MHz, $\Omega_s = 2\pi \times 120$ MHz. The relatively large γ_{31} and γ_{41} values taken for the calculation to basically match the experimental results may come from several factors. Under current experimental conditions, the main contributions are from the power broadening and collisional dephasing. The maximum value of the self-Kerr nonlinear coefficient n_2 for the four-level system (Fig. 4.3(c1)) can reach about 4×10^{-6} cm²/W with dramatic change near the atomic resonance similar to the case of the three-level system (Fig. 4.3(b1)) [85]. As one can see from Figs. 4.3(c1) and (d1), with an increase in the switching laser power, the slope of n_2 near the atomic resonance changes from negative to positive. Specifically, under strong switching laser power, as shown in Figs. 4.3(d1) and (d2), the line shape of n_2 can be understood as a superposition of three curves of the nonlinear coefficients from three atomic resonances [24].

The dependence of the self-Kerr nonlinear coefficient n_2 versus the switching laser power P_s at $\Delta_p/2\pi = 14$ MHz is depicted in Fig. 4.4. The dots with error bars (statistical errors) are the experimental data, and the solid line is a theoretical fitting using Eq. (4.7). From Fig. 4.4, one can clearly see that the Kerr nonlinear coefficient n_2 can be significantly modified at certain near-resonant probe frequency detunings, even switching the sign, by only changing the switching laser power. Such change of sign for nonlinear coefficient (or nonlinear dispersion slope) by controlling the switching beam power can be used in compensating the sharp linear dispersion change [4] to achieve the “white-light cavity” condition for the intracavity EIT medium, as done in the three-level EIT medium [107], with an additional control parameter.

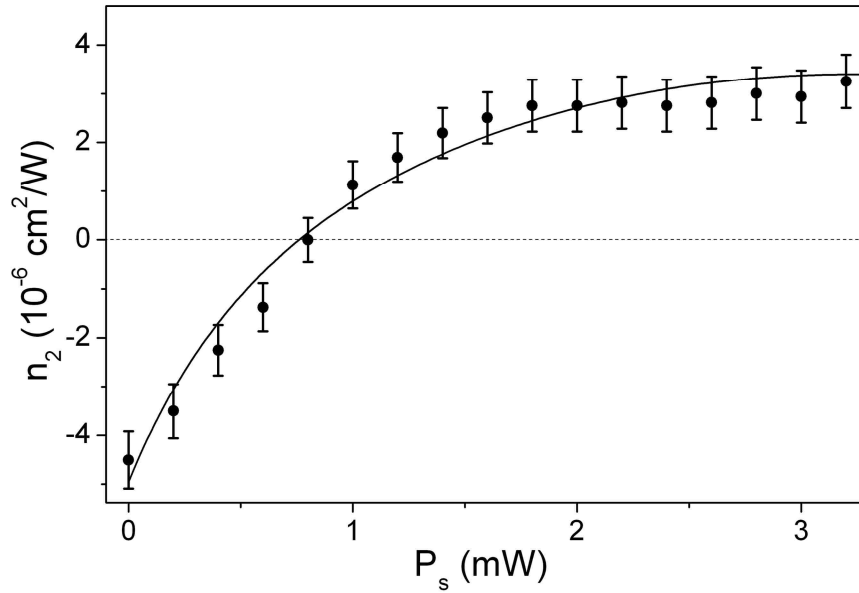


Figure 4.4: Experimentally measured (dots with error bars) and theoretically calculated (solid line) self-Kerr nonlinear coefficient n_2 as a function of P_s at $\Delta_p/2\pi = 14$ MHz. Other parameters are the same as in Fig. 4.3.

Actually Eq. (4.7) is a general solution which includes the cases for two-level, three-level lambda-type, and four-level N-type systems. There are a large number of parameters that can be adjusted in Eq. (4.7). We can also calculate the theoretical curve for the self-Kerr nonlinearity as a function of the switching frequency detuning Δ_s . However, experimental measurements for such detuning case can become quite complicated due to the closely-lying hyperfine levels of the rubidium D₂ line, which are all within the Doppler-broadened spectrum. We would also like to point out that the self-Kerr nonlinearity studied here is different from the cross-Kerr nonlinearity studied in the earlier works [105,106]. The cross-Kerr nonlinearity is proportional to $n_2^s I_s$, which corresponds to the term of $|\Omega_s|^2$ in the first-order solutions in Eq. 4.2, while the self-Kerr nonlinearity we studied here is proportional to $n_2^p I_p$, which is the feature of the third-order solutions for the probe beam. These two different kinds of Kerr nonlinearities produce different phenomena and therefore can have very different applications [17,103], for example, cross-Kerr nonlinearity can be used to control light with light [74] and self-Kerr nonlinearity is essential for spatial solitons [103].

4.2 Noise correlations in a doubly-resonant optical parametric oscillator

Simultaneous generations of correlated and entangled photon pairs have been extensively studied in various systems in recent years, since they are essential for applications in quantum communication and computation [108]. A common way to generate strongly correlated and entangled photon pairs or light beams in either below [109] or above [110,111] the threshold condition is to use optical parametric oscillation (OPO) system based on the $\chi^{(2)}$ parametric

down-conversion process in nonlinear crystals. In the multilevel atomic systems, the $\chi^{(3)}$ processes, such as FWM via atomic spin coherence and Stokes & anti-Stokes photons, have been shown to play key roles in producing correlated and entangled photons [111-116]. Bright correlated photon pairs have been generated in cold, as well as hot, atoms with or without an optical cavity [114-116]. Meanwhile, intensity correlations have also been widely studied in various situations, such as in EIT configuration with a magnetic field [117], atomic optical parametric oscillation (AOPO) [118], and FWM processes [119].

In this section, I will present an experimental study of simultaneously generating the bright Stokes and anti-Stokes fields by utilizing only one pump field in a Doppler-broadened atomic medium contained in an optical ring cavity [41]. The phenomenon of vacuum-induced absorption (VIA) has been observed rather than the vacuum-induced transparency (VIT) as reported in Ref. [120], in which a cavity with much higher finesse was used. The correlations and anti-correlations of the intensity noises between the two generated (Stokes and anti-Stokes) fields and the pump field can be investigated by using an external FP cavity to separate the generated Stokes and anti-Stokes fields. This is different from Refs. [118,121], since both the Stokes and anti-Stokes fields are on resonance with the cavity and the three-field correlations are considered in the current study.

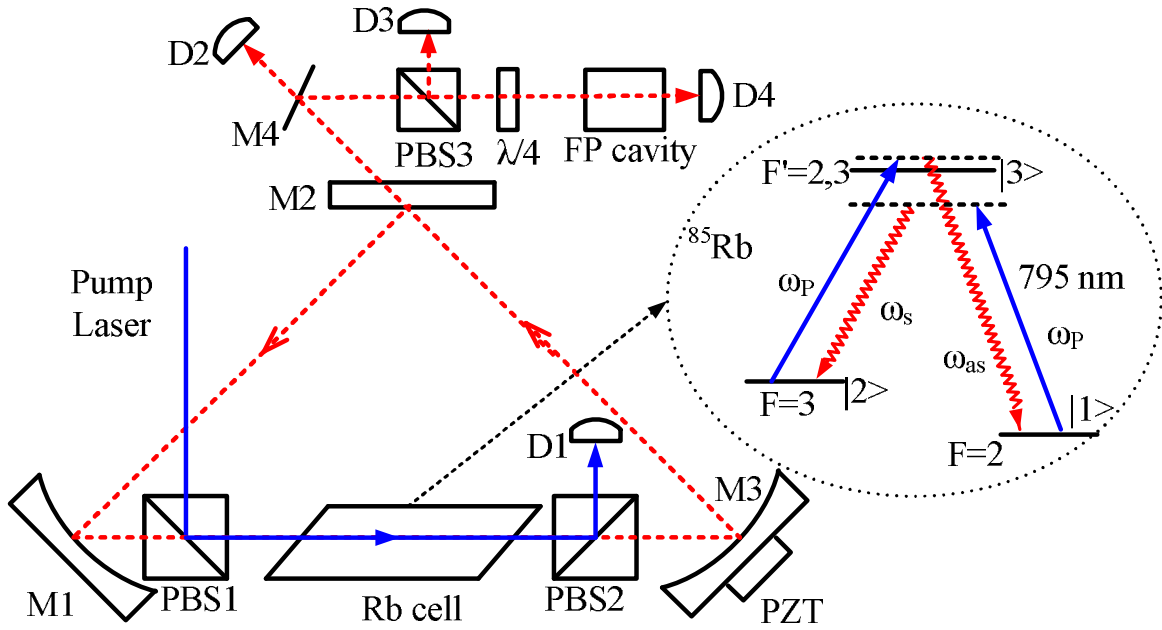


Figure 4.5: Experimental setup. PBS1-PBS3: polarization beam splitters; M1-M3: cavity mirrors; M4: flip mirror; D1-D4: detectors; and PZT: piezoelectric transducer. Bubble: ^{85}Rb D1 line energy levels and the laser coupling configuration.

The experimental setup is shown in Fig. 4.5. The optical ring cavity and the atomic vapor cell are the same as used in Section 2.2. The pump field is injected into the cavity through PBS1, and is detected by D1 after interacting with the atoms. The cavity output is directly detected by D2 with M4 down. The FP cavity, PBS3, $\lambda/4$ waveplate, and D3&D4 are used to investigate the spectral components of the cavity output field with M4 mirror up in position.

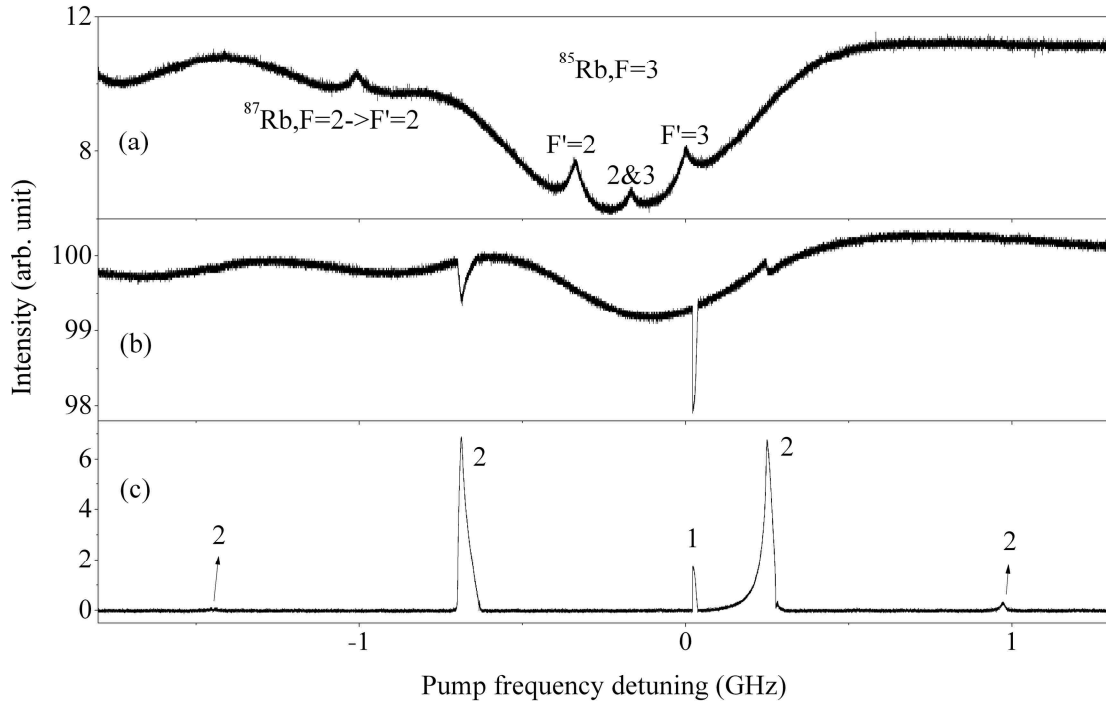


Figure 4.6: (a) Saturated absorption spectrum as a reference from another Rb cell (not shown in Fig. 4.5); (b) absorption spectrum detected by D1 (see Fig. 4.5); (c) cavity transmission detected by D2. The experimental parameters are: $P_p = 18$ mW and $T = 80^\circ\text{C}$.

The cavity transmission spectrum is measured with the pump field frequency scanning across the transition $F=3 \rightarrow F'$ in ^{85}Rb D1 line. No cavity transmission can be observed by D2 without heating up the Rb vapor cell. By increasing the Rb cell temperature to $\sim 80^\circ\text{C}$, corresponding to an atomic density of $\sim 1.5 \times 10^{12} \text{ cm}^{-3}$, several distinct peaks start to appear in the cavity transmission spectrum as shown in Fig. 4.6(c), and at the same time, some absorption dips emerge in the free space spectrum detected by D1 as shown in Fig. 4.6(b). Figure 4.6(a) is the saturated absorption spectrum of the Rb atoms in the same spectral range used as a

reference from an additional Rb atomic cell. Since it is important to identify the spectral components in the cavity transmission peaks, a 10 GHz FP cavity (Thorlabs SA210) is used to carefully analyze the spectral components in each peak. The cavity output frequency can be made to stand on each peak by locking both the pump field frequency and the cavity length properly. By scanning the FP cavity length, we find that peaks 1 and 2 in Fig. 4.6(c) have different frequency components. The frequencies of all peaks labeled 2 are the same as the pump field, and they are separated by ~ 822 MHz, which is the FSR of the optical ring cavity without the medium. While there are two different frequencies in peak 1, either up- or down-shifted by ~ 3 GHz from the pump frequency, which is the ^{85}Rb ground-state hyperfine splitting frequency, as shown in Fig. 4.7. We attribute the appearances of the peaks labeled 2 as either Raman scattering among the Zeeman sublevels [122] or Faraday rotation [123]. While the peak 1 is from the FWM processes, for which the frequency relationship is satisfied between the Stokes, anti-Stokes, and the pump fields, i.e. $\omega_{as} + \omega_s = 2\omega_p$. In Fig. 4.6(b), one can see that absorption is increased at the position of peak 1, which can be named as VIA with respect to the VIT reported in Ref. [120], since the Stokes and anti-Stokes fields are generated initially from vacuum and they then act to enhance the absorption of the pump field. The reason for an enhanced absorption instead of an enhanced transparency can be understood as following: the Stokes and anti-Stokes fields are first generated from spontaneous Raman scattering, then the stimulated Raman scattering or FWM process becomes dominant due to the match to the cavity modes, which promotes and induces the absorption of the strong pump field. Under the current conditions, the generated Stokes and anti-Stokes fields are always much weaker than the

pump field, which is different from the experiment reported in Ref. [120]. In that experiment, the cavity finesse is more than two orders of magnitude higher than the cavity used in the current experiment, hence, the intracavity field grown from the spontaneous Raman scattering has become much stronger than the pump (probe in Ref. [120]) field, therefore, transparency can be observed owing to the normal EIT condition.

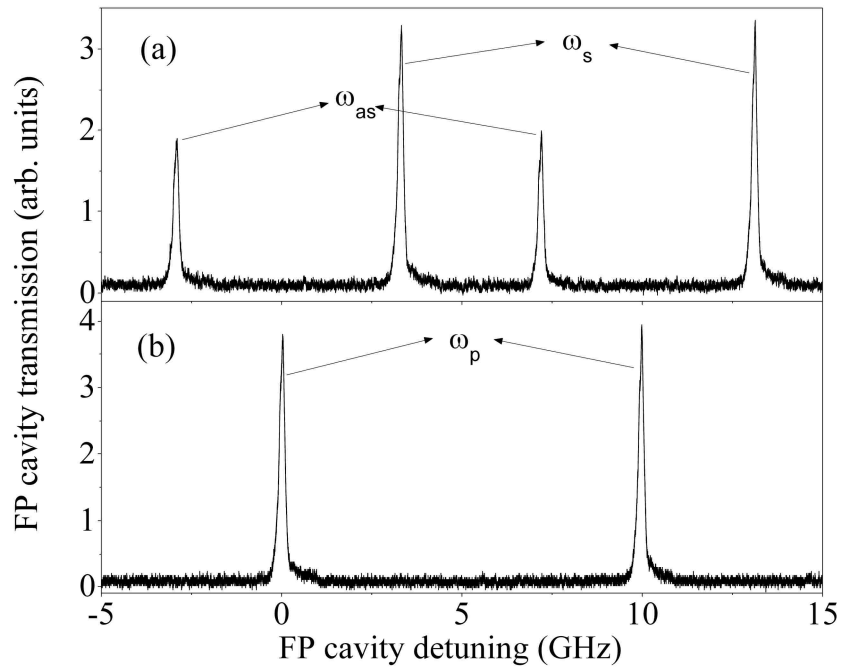


Figure 4.7: FP cavity transmission spectra at fixed pump frequencies. (a) and (b) correspond to peaks 1 and 2 in Fig. 4.6, respectively.

The oscillation thresholds for both Stokes and anti-Stokes fields at a higher temperature ($T \sim 95$ °C) are also measured. When the pump power is lower than 4.5 mW, there is no detectable cavity output to indicate the below threshold condition. By increasing the pump power, the Raman gain overcomes the

losses in the cavity, and the system starts to oscillate like an OPO, as shown in Fig. 4.8. No saturation behavior has been observed at the maximum pump power under the current experimental condition, and it is clear that both Stokes and anti-Stokes fields have similar threshold behavior.

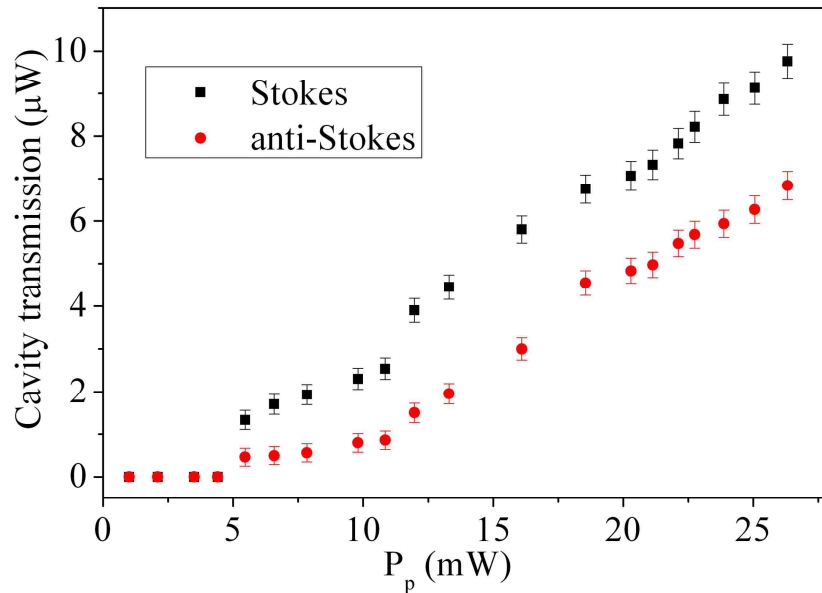


Figure 4.8: The cavity transmission powers of the Stokes and anti-Stokes fields, respectively, as a function of the pump laser power.

The noise correlation and anti-correlation properties between the Stokes, anti-Stokes, and the pump fields under far above-threshold condition are also studied. By using another home-made FP cavity (FSR = 750 MHz) and fixing the FP cavity length at the anti-Stokes peak, the anti-Stokes field passes through the FP cavity and is detected by D4, while the Stokes field is reflected and detected by D3. The temporal signal traces of the Stokes, anti-Stokes, and pump fields are depicted in Fig. 4.9(a), respectively. The cross-correlation function $G_{ij}^{(2)}(\tau)$ between

the intensity noises of any two fields can be calculated by [99]

$$G_{i,j}^{(2)}(\tau) = \frac{\langle \delta I_i(t) \delta I_j(t+\tau) \rangle}{\sqrt{\langle [\delta I_i(t)]^2 \rangle \langle [\delta I_j(t+\tau)]^2 \rangle}}, \quad (4.9)$$

where $\delta I_{ij} = I_{ij} - \langle I_{ij} \rangle$ with $\langle \rangle$ being the temporal averaging; and τ is the selected time delay between the two signals. $G_{i,j}^{(2)}(\tau) = 1$ (or -1) represents that the two fields, i.e., fields i and j , are perfectly correlated (or anti-correlated).

The cross-correlation functions $G_{ij}^{(2)}(\tau)$ for the Stokes and the anti-Stokes, the Stoke and the pump, and the anti-Stokes and the pump fields are shown in Figs. 4.9(b-d), respectively. The degrees of cross correlations at zero time delay are calculated to be $G_{s,as}^{(2)}(0) \approx 0.95$, $G_{p,s}^{(2)}(0) \approx -0.84$, and $G_{p,as}^{(2)}(0) \approx -0.87$, respectively, which implies that the fields are highly correlated or anti-correlated. The oscillations appearing in Figs. 4.9(b-d) are due to the unwanted frequency modulation introduced due to the optical ring cavity frequency locking. By analyzing the frequency components using the fast Fourier transform (FFT), the noise power as a function of frequency is plotted in Fig. 4.10. One can see that the noise peak at ~ 14 kHz is the exact frequency modulation used for the cavity locking.

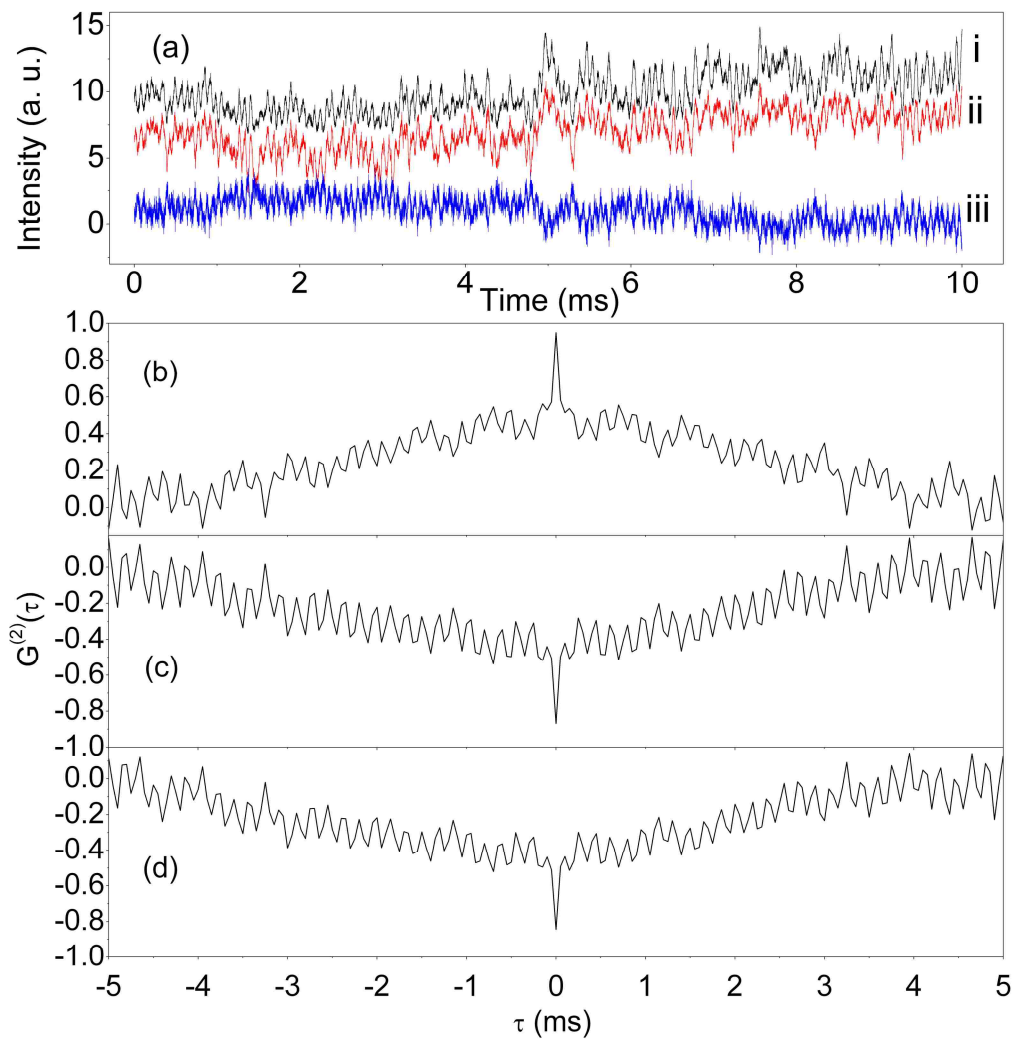


Figure 4.9: (a) Typical temporal waveforms of the (i) Stokes (black curve), (ii) anti-Stokes (red curve), and (iii) pump (blue curve) beams. Cross correlations $G^{(2)}(\tau)$ for (b) the Stokes and the anti-Stokes; (c) the Stokes and the pump; and (d) the anti-Stokes and the pump fields, respectively. The experimental parameters are: $T = 95 \text{ }^\circ\text{C}$ and $P_p = 25 \text{ mW}$.

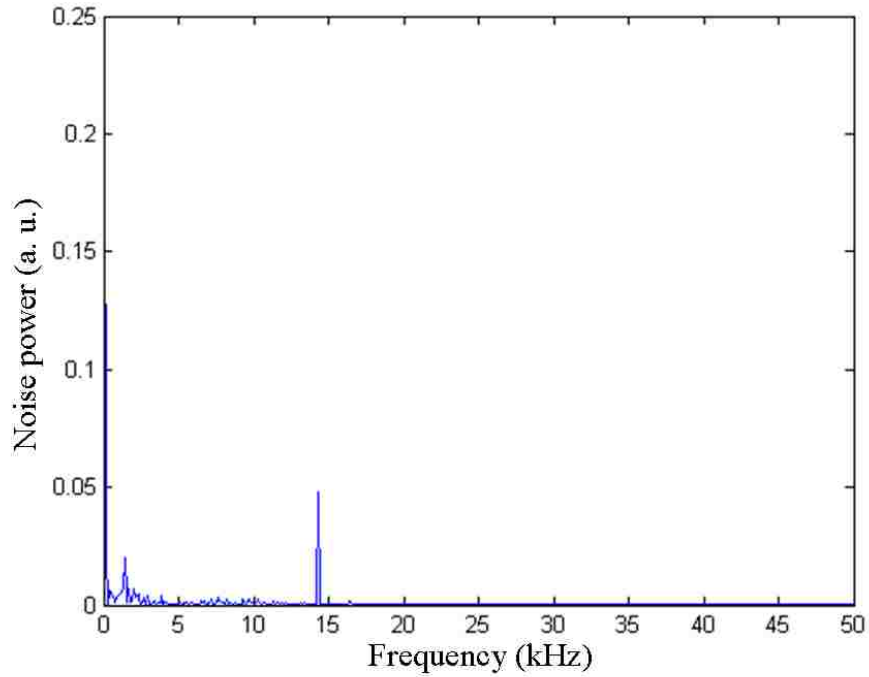


Figure 4.10: Noise power as a function of frequency from FFT.

The delay between the Stokes and anti-Stokes fields originating from the time it takes to convert the atomic spin coherence into an anti-Stokes light pulse is not shown here since the time scale in the current experiment (~ 1 ms) is much larger than the typical delay time (~ 1 μ s) [37]. The physical picture of the above results can be understood as following: one atom absorbs two pump photons and then emits one Stokes photon and one anti-Stokes photon almost simultaneously; therefore, the Stokes and anti-Stokes fields should be correlated just as in the OPO with a $\chi^{(2)}$ nonlinear crystal, while the Stokes (or anti-Stokes) and the pump fields should be anti-correlated. Although quantum correlations have not been measured in the current setup, we believe that this system should be a good candidate for multi-photon correlation source in quantum information processing as predicted in Ref. [124].

Chapter 5 Parity-time symmetry and photonic structures in atomic systems

5.1 Generation of parity-time symmetric potentials in an N-type atomic system

There are two basic axioms in quantum theory, one is that the energy levels must be real and the other is that the time evolution must be unitary. A simple condition is that when every element in the matrix of the Hamiltonian is real and symmetric, these two laws are guaranteed, however, this is not the most general condition. A more general condition is known as Hermiticity, which can be found in all the quantum mechanics text books. However, about 25 years ago, a new group of Hamiltonians have been discovered, which are not Hermitian, but they can also satisfy these two laws. This new kind of Hamiltonian is called PT symmetric. Non-Hermitian PT-symmetric Hamiltonians have attracted considerable attention since they were first proposed by Bender and Boettcher in 1998 [125]. Under certain conditions, such PT-symmetric Hamiltonians display entirely real spectra—a property often thought to belong exclusively to Hermitian systems [126]. Quite recently, this counter-intuitive behavior has been theoretically and experimentally demonstrated in a number of optical settings that judiciously engage both gain and loss processes [127-137]. This was accomplished by exploiting the mathematical isomorphism existed between the quantum Schrödinger and the paraxial wave equations [127].

Along different lines, in multilevel atomic media, both the linear and nonlinear optical properties of EIT phenomena have been intensively investigated in the past two decades [2]. A host of intriguing spatial phenomena have been observed in EIT-related systems, including

electromagnetically induced focusing and waveguiding [101, 138-141], as well as self-imaging [142], grating behavior [143] and soliton propagations [144].

In this section, I will present a theoretical proposal to show that PT-symmetric conditions can be achieved in an atomic assemble involving EIT-related four-level atoms by spatially engineering the complex refractive indices of the coherently-prepared atomic medium. In optical regime, PT symmetric condition demands that $n(x) = n^*(-x)$, i.e. the real and imaginary parts of the refractive index profiles must be symmetric and anti-symmetric functions of the transverse coordinate x , respectively [127-137]. To illustrate the basic properties regarding PT symmetry, let's see a simple coupled waveguides model in the following.

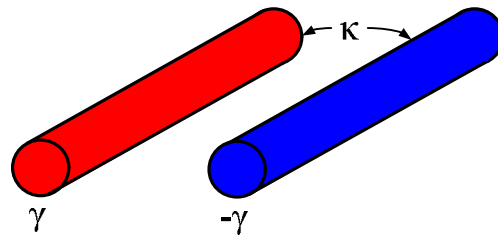


Figure 5.1: Coupled waveguides model.

The coupled waveguides model is shown in Fig. 5.1. The two waveguides are coupled with a coefficient of κ , and one waveguide has absorption γ and the other has gain $-\gamma$. These two waveguides form a basic PT symmetric system. The coupled mode equations for the two waveguides can be obtained as [145]

$$\begin{cases} i \frac{d\psi_1}{dz} + \kappa\psi_2 - i\gamma\psi_1 = 0 \\ i \frac{d\psi_2}{dz} + \kappa\psi_1 + i\gamma\psi_2 = 0 \end{cases} \quad (5.1)$$

with z as the propagating direction and ψ_i ($i=1,2$) as the waveguide modes. Then the Hamiltonian for the above system can be written as

$$H = \begin{pmatrix} i\gamma & -\kappa \\ -\kappa & -i\gamma \end{pmatrix}, \quad (5.2)$$

and the eigenvalues are given as

$$E_n = \pm \sqrt{\kappa^2 - \gamma^2}. \quad (5.3)$$

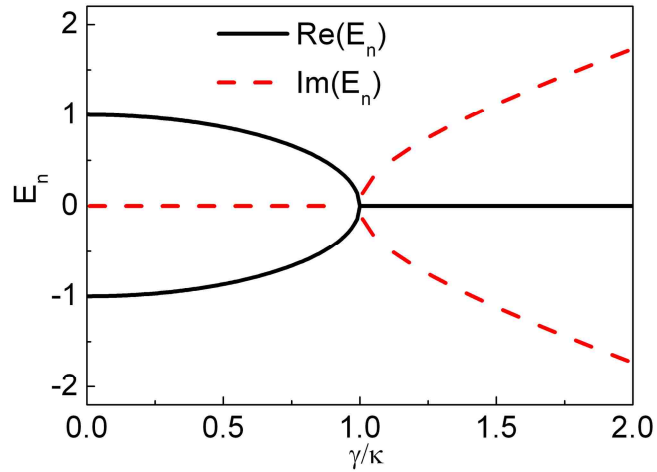


Figure 5.2: Eigenvalues for the coupled waveguides system [129].

Equation (5.3) is plotted in Fig. 5.2. From Eq. (5.3) or Fig. 5.2, one can find that the eigenvalues are real if $\kappa \geq \gamma$, and the eigenvalues become complex if $\kappa < \gamma$. Therefore,

$\gamma/\kappa=1$ is called the PT-symmetric threshold and above the threshold case is called PT symmetry breaking. In more sophisticated systems, PT-symmetric threshold is determined by many parameters, and gain/loss ratio is one of them [127-137].

The realization of PT symmetry in atomic media offers several advantages over solid-state systems. For example, optical structures like coupled waveguide systems can be easily reconfigured, tuned, and effectively controlled in an atomic medium through various external parameters, i.e., frequency detunings and Rabi frequencies of the coupling and pump fields. In addition, by introducing or interfering coupling beams or by using spatial light modulators, PT-symmetric optical lattices can be readily established in the spatial domain. Recently, several PT-symmetric optical configurations in solid-state systems have been suggested as means to realize nonreciprocal energy transport [146,147], perfect laser absorbers [148], laser amplifiers [149], etc. To date, all experimental studies carried out in PT-symmetric optics have relied on gain/loss arrangements using solid-state materials [135-137]. Therefore, the implementation of PT-symmetric potentials in atomic media will pave the way for new avenues in exploring such interesting phenomena.

A four-level N-type atomic system is considered, as shown in Fig. 5.3(a). The signal, coupling, and pump fields drive the atomic transitions $|1\rangle\text{-}|3\rangle$, $|2\rangle\text{-}|3\rangle$, and $|1\rangle\text{-}|4\rangle$, respectively. The four-level N-type systems with active Raman gain [150] are distinct from the other type of N-type systems that are based on two-photon absorption [18], which has been briefly described in Section 1.1. Throughout this work, and without any loss of generality, we focus our attention

on the Rubidium N-type atomic system with active Raman gain. By choosing appropriate parameters, the two coupling (blue, ii) and two pump (green, iii) beams, which propagate in the z direction, form a coupled waveguide structure, with one providing gain while the other having absorption. The signal (red, i) beam propagates in the same direction along with the coupling and pump beams, as shown in Fig. 5.3(b).

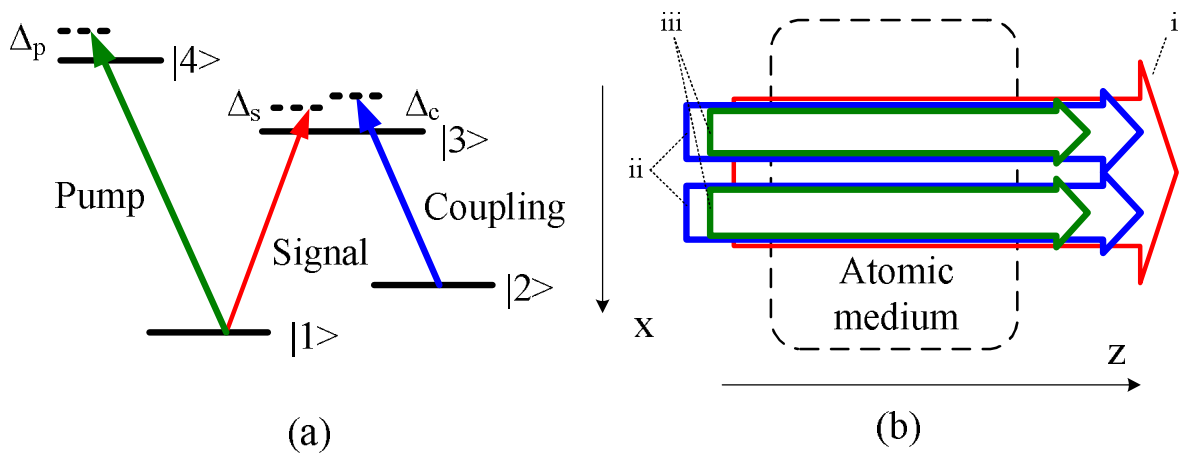


Figure 5.3: (a) The relevant four-level N-type atomic system. (b) The schematic diagram with signal (red, i), coupling (blue, ii), and pump (green, iii) fields. X and Z represent the transverse and longitudinal directions of propagation, respectively.

Under the rotating-wave approximation, the density-matrix equations for the four-level N-type atomic system are given by [150]

$$\begin{aligned}
\dot{\rho}_{22} &= \Gamma_{42}\rho_{44} + \Gamma_{32}\rho_{33} - \Gamma_{21}\rho_{22} + \frac{i}{2}(\rho_{32}\Omega_c^* - \rho_{23}\Omega_c), \\
\dot{\rho}_{33} &= \Gamma_{43}\rho_{44} - \Gamma_{32}\rho_{33} - \Gamma_{31}\rho_{33} + \frac{i}{2}(\rho_{23}\Omega_c - \rho_{32}\Omega_c^* + \rho_{13}\Omega_s - \rho_{31}\Omega_s^*), \\
\dot{\rho}_{44} &= -(\Gamma_{43} + \Gamma_{42} + \Gamma_{41})\rho_{44} + \frac{i}{2}(\rho_{14}\Omega_p - \rho_{41}\Omega_p^*), \\
\dot{\rho}_{21} &= -\tilde{\gamma}_{21}\rho_{21} + \frac{i}{2}\rho_{31}\Omega_c^* - \frac{i}{2}\rho_{24}\Omega_p - \frac{i}{2}\rho_{23}\Omega_s, \\
\dot{\rho}_{31} &= -\tilde{\gamma}_{31}\rho_{31} + \frac{i}{2}\rho_{21}\Omega_c - \frac{i}{2}\rho_{34}\Omega_p + \frac{i}{2}(\rho_{11} - \rho_{33})\Omega_s, \\
\dot{\rho}_{41} &= -\tilde{\gamma}_{41}\rho_{41} - \frac{i}{2}\rho_{43}\Omega_s + \frac{i}{2}(\rho_{11} - \rho_{44})\Omega_p, \\
\dot{\rho}_{32} &= -\tilde{\gamma}_{32}\rho_{32} + \frac{i}{2}(\rho_{22} - \rho_{33})\Omega_c + \frac{i}{2}\rho_{12}\Omega_s, \\
\dot{\rho}_{42} &= -\tilde{\gamma}_{42}\rho_{42} - \frac{i}{2}\rho_{43}\Omega_c + \frac{i}{2}\rho_{12}\Omega_p, \\
\dot{\rho}_{43} &= -\tilde{\gamma}_{43}\rho_{43} + \frac{i}{2}\rho_{13}\Omega_p - \frac{i}{2}\rho_{42}\Omega_c^* - \frac{i}{2}\rho_{41}\Omega_s^*,
\end{aligned} \tag{5.4}$$

where $\Omega_s = \mu_{13}E_s/\hbar$, $\Omega_c = \mu_{23}E_c/\hbar$, and $\Omega_p = \mu_{14}E_p/\hbar$ are the Rabi frequencies of the signal, coupling, and pump fields, respectively. For simplicity we define $\tilde{\gamma}_{21} = \gamma_{21} - i(\Delta_s - \Delta_c)$, $\tilde{\gamma}_{31} = \gamma_{31} - i\Delta_s$, $\tilde{\gamma}_{41} = \gamma_{41} - i\Delta_p$, $\tilde{\gamma}_{32} = \gamma_{32} - i\Delta_c$, $\tilde{\gamma}_{42} = \gamma_{42} - i(\Delta_c + \Delta_p - \Delta_s)$, and $\tilde{\gamma}_{43} = \gamma_{43} - i(\Delta_p - \Delta_s)$. Γ_{nm} is the natural decay rate between level $|n\rangle$ and level $|m\rangle$; and $\gamma_{nm} = (\Gamma_n + \Gamma_m)/2$. Here, $\Delta_s = \omega_s - \omega_{31}$, $\Delta_c = \omega_c - \omega_{32}$, and $\Delta_p = \omega_p - \omega_{41}$ are the frequency detunings for the signal, coupling, and pump fields, respectively. The susceptibility of the atomic medium can be obtained through the expression $\chi = \frac{2N\mu_{13}}{\varepsilon_0 E_s} \rho_{31}$. Given that

$n = \sqrt{1 + \chi} \approx 1 + \chi/2$, $\chi = \chi' + i\chi''$, and $n = n_0 + n_R + in_I$, the real and imaginary parts of the refractive index can be written as $n_R \approx \frac{1}{2}\chi' = \frac{N\mu_{13}}{\varepsilon_0 E_s} \text{Re}(\rho_{31})$ and $n_I \approx \frac{1}{2}\chi'' = \frac{N\mu_{13}}{\varepsilon_0 E_s} \text{Im}(\rho_{31})$.

Here, $n_0 = 1$ is the background index of the atomic medium.

Usually, the general result for the linear susceptibility of such four-level N-type atomic system with active Raman gain can not be obtain in a compact form. In order to obtain an analytical solution, we can assume that all the atoms are at level $|2\rangle$, i.e., $\rho_{22} \approx 1$, $\rho_{11} \approx 0$, $\rho_{33} \approx 0$, and $\rho_{44} \approx 0$. Since the signal field is relatively weak compared with the coupling and pump fields ($\Omega_s \ll \Omega_c, \Omega_p$), by solving Eq. (5.4) under the steady-state limit, the density-matrix element ρ_{13} can be obtained as [151]

$$\rho_{31} = \frac{-i\Omega_s\Omega_c^2(\Omega_c^2 - \Omega_p^2 + 4\tilde{\gamma}_{42}^*\tilde{\gamma}_{43}^*)}{2\tilde{\gamma}_{32}^*[(\Omega_c^2 - \Omega_p^2)^2 + 4(\tilde{\gamma}_{21}\tilde{\gamma}_{31} + \tilde{\gamma}_{42}^*\tilde{\gamma}_{43}^*)\Omega_c^2 + 4(\tilde{\gamma}_{31}\tilde{\gamma}_{43}^* + \tilde{\gamma}_{21}\tilde{\gamma}_{42}^*)\Omega_p^2 + 16\tilde{\gamma}_{21}\tilde{\gamma}_{31}\tilde{\gamma}_{42}^*\tilde{\gamma}_{43}^*]}. \quad (5.5)$$

Such assumption is valid when coupling frequency detuning Δ_c is large. However, due to the near resonant cases are considered in this section, we will use numerical method in the following calculations.

We begin by considering the realization of a dual channel PT-symmetric potential (two waveguides as shown in Fig. 5.3(b)) that could allow exchange of optical energy between the two channels. This is possible by employing two different coupling fields side by side-each having an identical Gaussian intensity profile while the susceptibility of the signal field varies in the x direction as a function of the coupling field intensity. Since the coupling fields are from two independent lasers and the overlapped region between them is relatively small, the phase effect between them is not considered here. In this case the total spatial intensity distribution of the coupling beams has the form of

$$I_c(x) = A \left(e^{-\frac{(x-a)^2}{2\sigma^2}} + e^{-\frac{(x+a)^2}{2\sigma^2}} \right), \quad (5.6)$$

where A is a constant, $2a$ is the separation between the centers of the two potential channels, and $2\sqrt{2\ln 2}\sigma$ is the full-width-at-half-maximum (FWHM) of the beam width. Even though the coupling intensity spatial profiles for these two channels are identical, by choosing different coupling frequency detunings (Δ_c), one can actually introduce gain in one waveguide and absorption in the other one. The advantage offered by this scheme is that the refractive index now spatially varies only with the coupling intensity, since all the other parameters are fixed in each waveguide.

In this arrangement, perhaps the most challenging task is to find the proper coupling frequency detunings with proper choice of other parameters for a simultaneous gain and absorption in these two channels, respectively. To do so, we first have to identify the relation between the susceptibility and the coupling frequency detuning. By solving Eq. (5.4) numerically, one can obtain the real (dispersion) and imaginary (gain/absorption) parts of the susceptibility versus the coupling detuning for various coupling intensities as shown in Figs. 5.4(a) and (b), respectively. The parameters used in this example are: $\Delta_s = \Delta_p = 0$, $\Omega_s/2\pi = 0.1$ MHz, $\Omega_p/2\pi = 6$ MHz, $\Gamma_{31}/2\pi = \Gamma_{32}/2\pi = \Gamma_{41}/2\pi = \Gamma_{42}/2\pi = 3$ MHz, $\Gamma_{21} = \Gamma_{43} = 0$, and $\Omega_c/2\pi = 2$, 1, and 0.5 MHz for black (solid), red (dashed), and blue (dotted) curves, respectively.

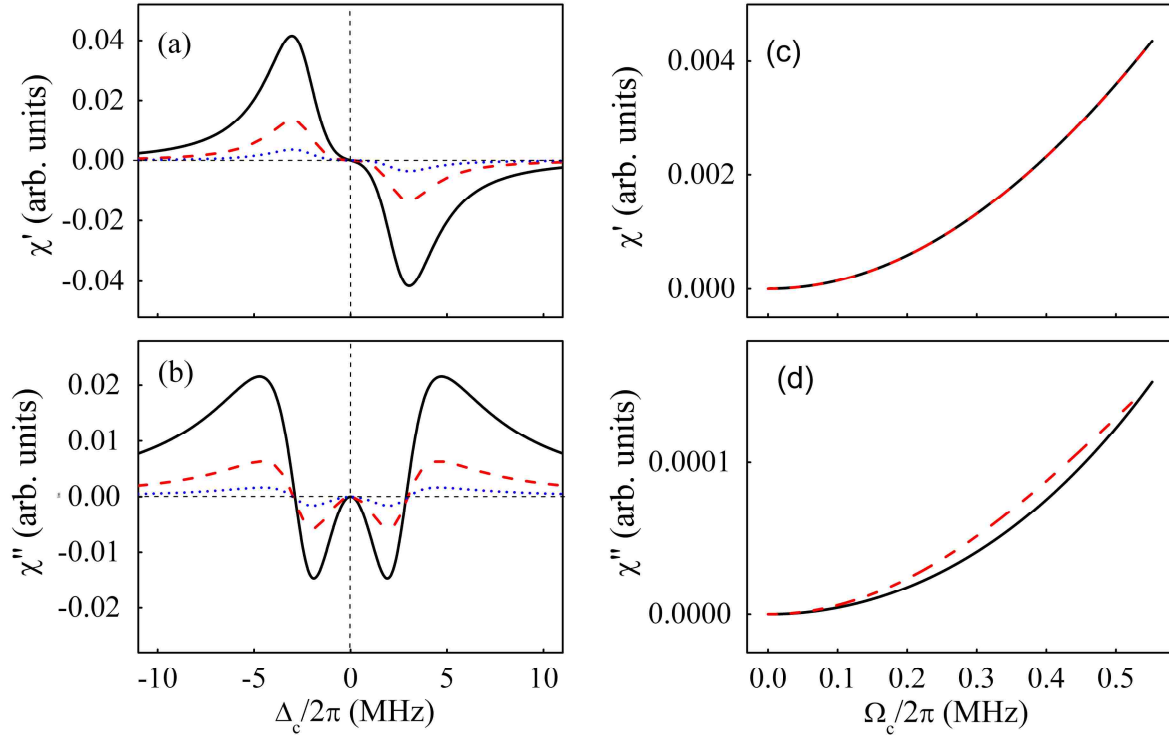


Figure 5.4: (a) The real (dispersion) and (b) imaginary (gain/absorption) parts of the susceptibility versus the coupling frequency detuning. $\Omega_c/2\pi = 2, 1,$ and 0.5 MHz for black (solid), red (dashed), and blue (dotted) curves, respectively. The (c) real and (d) imaginary parts of the susceptibility versus the coupling Rabi frequency. The black (solid) / red (dashed) curves represent χ' and χ'' for the gain/absorption waveguides. The chosen parameters are $\Delta_c/2\pi = -2.939$ and -3.045 MHz for the gain and absorption waveguides, respectively.

To achieve waveguiding, the signal field is focused at the center of each waveguiding channel that is formed by the joint actions of the coupling and pump beams, i.e., the maximum coupling intensity regions. Therefore, the real part of the susceptibility needs to get larger with increasing coupling intensity. For this reason, the coupling detunings should be negative. Also,

we notice that the imaginary part of the susceptibility is close to zero when the coupling detuning is ~ -2.992 MHz, as shown in Fig. 5.4(b), and in the vicinity of this zero point, absorption is induced on the left side, while gain on the right. Such property, commonly referred to as refractive index enhancement with vanishing absorption, has been widely studied in both near-resonant [6,152,153] and far-off resonant [154,155] atomic systems.

Next, we choose two different coupling frequency detunings trying to simultaneously introduce gain and absorption in the two separate waveguides. This implies that the only difference between these two channels is the values of coupling detuning, while all other parameters remain to be identical. To achieve this goal, we need to get the relation between the susceptibility and the coupling Rabi frequency. For example, by choosing $\Delta_c/2\pi = -2.939$ and -3.045 MHz for the two coupling fields, we find that the real parts of the susceptibility associated with these two waveguides overlap quite well, as shown in Fig. 5.4(c). The imaginary parts for the gain and loss waveguides are not matched perfectly, as shown in Fig. 5.4(d) (in order to directly compare the two curves, the curve for the gain waveguide is flipped by multiplying a minus sign for the black solid curve). In Fig. 5.4(c), the black solid and red dashed curves represent the real indices for the formed gain and absorption waveguides, respectively.

Once a relation is established between the susceptibility and the Rabi frequency of the coupling field, one can then obtain the spatial index modulation (or the potential). For the intensity distribution described in Eq. (5.6), and by choosing the FWHM ($2\sqrt{2\ln 2}\sigma$) to be 7

μm when the separation between the two waveguides (2a) is $20 \mu\text{m}$, the intensity-dependent index graphs displayed in Figs. 5.4(c) and (d) can be converted into their corresponding index landscapes, as shown in Fig. 5.5. It is clear that the real part of the refractive index distribution is an even function of position x , whereas, at the same time, the imaginary part is odd. The value of the refractive index can be easily modified by changing the atomic density. Here, we have assumed the atomic density of rubidium atoms to be $\sim 10^{13} \text{ cm}^{-3}$. In this case the maximum contrast in the real part of the refractive index is in the order of 10^{-3} and, thus, each optical potential channel can support only one mode. Interestingly, both the real and imaginary parts scale equally when the atomic density is changed. For realizing the desired PT symmetry it is important that one can control the ratio between the real and imaginary indices since it determines whether the system is at below or above the PT-symmetric threshold [127-137]. In order to change the ratio, the two coupling frequency detunings need to be altered, so as to change the real and imaginary parts simultaneously as dictated by the Kramers-Kronig relations. For the chosen parameters, the real part is less sensitive and changes less than the imaginary part. When the coupling detunings move away from the near zero point ($\Delta_c/2\pi \approx -2.992 \text{ MHz}$), the ratio between the real and imaginary indices can be modified from ~ 500 to 10 . Therefore, the system can operate either below (Fig. 5.5(a)) or above (Fig. 5.5(b)) the threshold point, or can even behave as a passive one without PT symmetry (Fig. 5.5(c)). Here, the ratio between the real and imaginary indices is ~ 38 , 15 , and 410 , for Figs. 5.5(a-c), respectively. Under these conditions the PT-symmetric threshold is ~ 27 - as determined by the complex index profiles of the involved waveguides. It is worth to point out that the realization of transverse spatial

modulation without absorption or gain as shown in Fig. 5.5(c) can be easily converted to periodically controllable photonic structures by using standing-waves along the wave propagation direction [156].

The field modes (eigenvectors) in the coupled waveguide system under different conditions as shown in Figs. 5.5(a-c) are depicted in Figs. 5.5(d-f), respectively. The modes for the below threshold case (Fig. 5.5(a)) should be symmetric and the eigenvalues of the corresponding modes should be real. However, due to the imperfect symmetric real and anti-symmetric imaginary indices of the system, the two modes are slightly asymmetric, as shown in Fig. 5.5(d), and the corresponding eigenvalues have a tiny imaginary part. Such asymmetric modes are not caused by the PT symmetry breaking. When the PT symmetric condition is broken, i.e., the above threshold case, as shown in Fig. 5.5(b), the modes become severely asymmetric and each mode is confined in its corresponding waveguide, i.e., gain or absorption waveguide, respectively, as shown in Fig. 5.5(e). Meanwhile, the eigenvalues become complex and the corresponding imaginary part gives the gain or absorption for each mode. For the passive case (Fig. 5.5(c)), the modes are perfectly symmetric, as shown in Fig. 5.5(f).

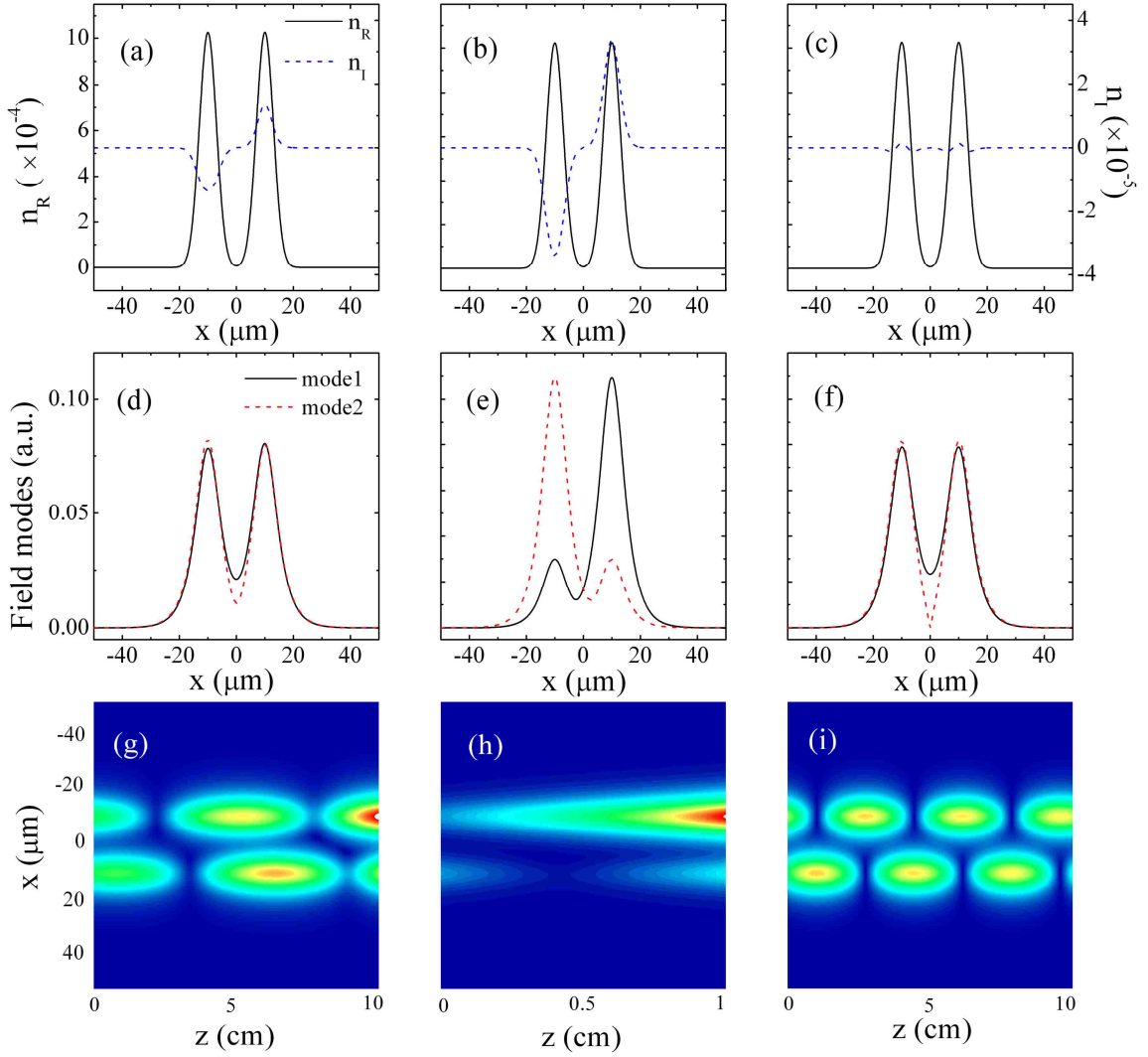


Figure 5.5: The real (solid black curves) and imaginary (dashed blue curves) refractive indices as a function of position x for (a) below threshold, (b) above threshold, and (c) passive cases. The parameters used are $\Delta_c/2\pi = -2.97$ and -3.01 MHz for the gain and loss waveguides in part (a); $\Delta_c/2\pi = -2.94$ and -3.04 MHz for waveguides in (b); and $\Delta_c/2\pi = -2.992$ MHz in (c), respectively. The atomic density is $\sim 10^{13} \text{ cm}^{-3}$ while the other parameters are the same as in Fig. 4. Pictures (d-f) and (g-i) show the field modes and optical beam propagation patterns for the signal beam in the index potentials of (a-c), respectively.

Figures 5.5(g-i) show how a signal beam will propagate in the corresponding index structures as given in Figs. 5.5(a-c), respectively. In the case of the PT-symmetric potential which operates below the symmetry breaking threshold, the light dynamics looks similar to that of a passive coupler, i.e., the optical field oscillates periodically between the two waveguides. However the rate at which energy is transferred crucially depends on the direction of the flow (gain to loss or loss to gain). Furthermore, by increasing the gain/loss contrast, transitions from stable to exponentially growing modes can occur, signifying the onset of PT-symmetry breaking, as shown in Fig. 5.5(h). Finally propagation dynamics of the passive potential of Fig. 5.5(c) is depicted in Fig. 5.5(i). It is clear to see that the period of oscillation is slightly less than that of the corresponding PT-symmetric potential (Fig. 5.5(g)).

Note that as opposed to use Gaussian profiles assumed here, one could use Bessel-Gauss beams to overcome the severe diffraction effect in setting up this type of PT-symmetric potentials [157]. The undepleted approximation is used by assuming that the pump and coupling fields are not severely absorbed during their propagations in the medium. Also, either single- or multi-mode signal beam can be supported in this system, which depends on the properties of the induced waveguides, such as their widths and refractive indices.

Perfect situations are usually considered when the optical properties of PT-symmetric systems are studied, i.e., perfectly symmetric real and anti-symmetric imaginary parts of the refractive index. However, when constructing a real optical PT-symmetric potential in a practical system, such ideal conditions are difficult to reach, especially with the atomic media.

Here, we would like to consider how imperfect symmetric and anti-symmetric parts of the index will affect the desired PT-symmetric properties. Let's define the deviation from a perfect symmetry/anti-symmetric function as

$$\Delta(x) = n(x) - n^*(-x) \quad (5.7)$$

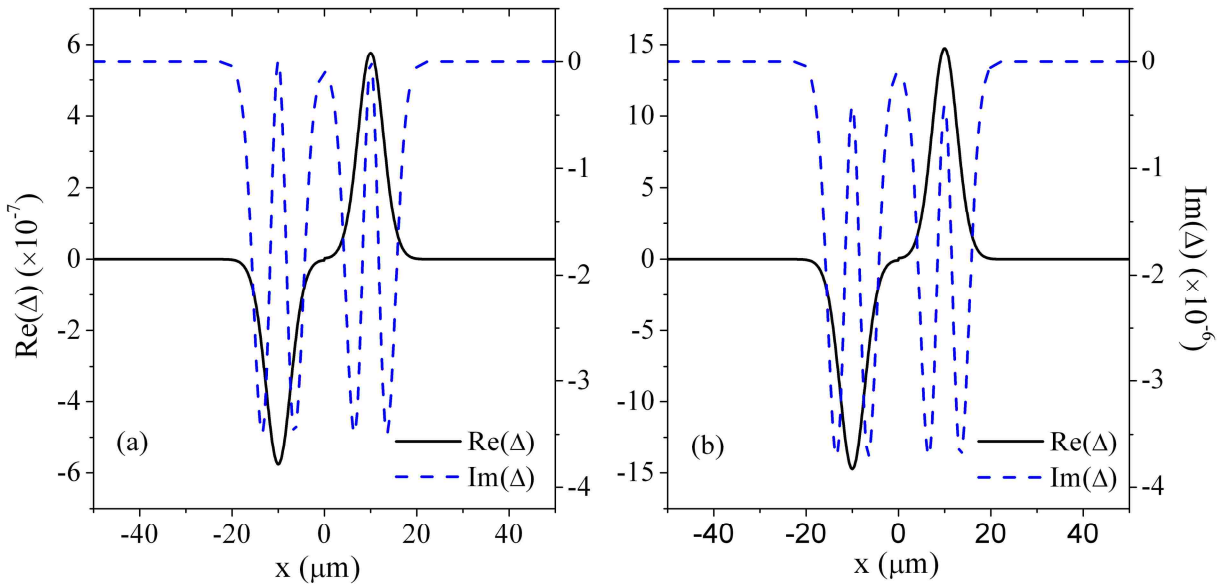


Figure 5.6: The asymmetric function for the real (solid black curves) and imaginary (dashed blue curves) parts of the refractive index calculated using realistic parameters for (a) below and (b) above threshold cases, as shown in Figs. 5.5(a) and (b), respectively.

Making $\Delta(x)$ close to zero is the goal when optimizing parameters. Figure 5.6 shows the deviation from the symmetric/anti-symmetric functions for the real (solid black curves) and imaginary (dashed blue curves) parts of the refractive index for (a) below and (b) above threshold cases shown in Figs. 5.5(a) and (b), respectively. From Fig. 5.6, one can see that the

degrees of asymmetry for the real and imaginary parts are several percents, and therefore should have no significant impact in practical systems.

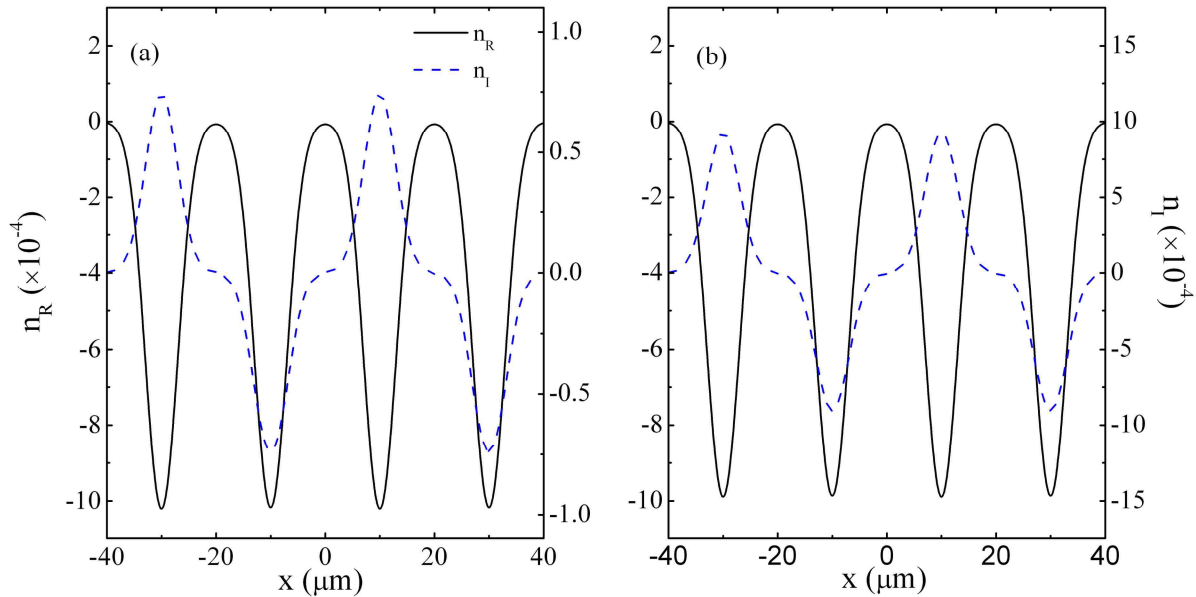


Figure 5.7: The real (solid black curves) and imaginary (dashed blue curves) parts of the refractive index for periodic lattices as a function of position x when the coupling intensity and coupling detuning are spatially modified. (a) and (b) are the below and above PT symmetric threshold cases, respectively. Notice the difference in the scales of n_I for figures (a) and (b).

Next, we consider the cases for positive coupling detunings, so that the real part of the refractive index becomes smaller as the coupling intensity increases. We also introduce additional coupling beams in order to realize an optical lattice potential, as shown in Fig. 5.7(a), since optical lattices are more promising for realizing PT symmetry in atomic media than coupled waveguides because they possess much richer phenomena and have no problems caused

by diffraction in the medium. Unlike the configuration discussed previously, each waveguide channel in this lattice case is composed of half gain and half loss. The ratio between the real and imaginary indices in Fig. 5.7(a) is now ~ 6.9 , which is below PT-symmetric threshold. To achieve this, we simply move the coupling detuning farther away from the zero point ($\Delta_c/2\pi \approx 1.7155$ MHz). However, this leads to an increase in the asymmetry of the real index. To balance the real and imaginary parts, different pump intensities for the gain and absorption regimes are now necessary. The parameters used in Fig. 5.7(a) are $\Delta_c/2\pi = 2.882$ (3.102) MHz and $\Omega_p/2\pi = 6$ MHz for the gain (absorption) regime. The other parameters are the same as in Fig. 5.5. By properly choosing the coupling detunings and the pump intensities, the ratio between the imaginary and the real parts can be controlled in the similar way as used in Fig. 5.5. Figure 5.7(b) shows the above threshold case and the ratio between the real and imaginary indices is ~ 0.5 .

The band structure of this lattice reveals an interesting property which has not been observed in other periodic lattices, i.e., by increasing the gain/loss contrast, the first band (curve i in Fig. 5.8(a)) remains intact from symmetry breaking, as shown in Fig. 5.8. Instead, the band merging effect starts from the higher-order bands. This is due to the fact that the gain and loss regions are mostly confined to the two sides of each waveguide channel and thus have a minimum overlap with the lowest-order Floquet-Bloch mode of the first band (that is mostly confined to the center of each channel). On the other hand, the second-band Floquet-Bloch wave functions overlap more effectively with these gain and loss regions and therefore this

band is the first one to break its PT symmetry. The major difference between the below (Fig. 5.8(a)) and the above (Fig. 5.8(b)) PT-symmetric threshold cases can be seen from the corresponding imaginary parts. In Fig. 5.8(a), the imaginary parts are kept zero for all the eigenvalues, while in Fig. 5.8(b), the imaginary parts become non-zero.

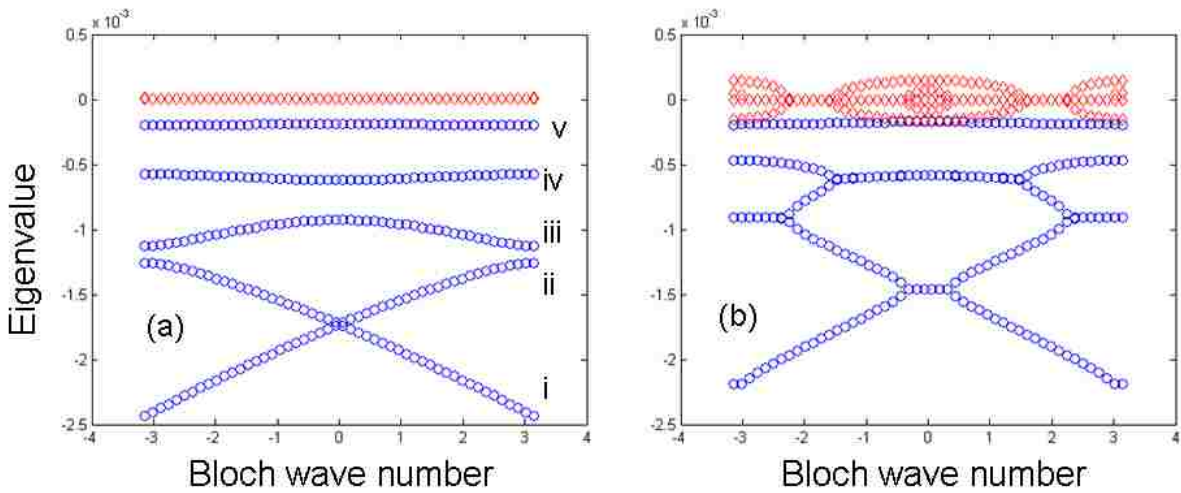


Figure 5.8: (a) and (b) are the band structures within the Brillouin zone for the cases as shown in Figs. 5.7(a) and (b), respectively. The blue circles are the real parts of the first five bands and the red diamonds are for the imaginary parts.

The relation between the coupling efficiency and the separation of adjacent channels has been studied in Ref. [127] for coupled waveguide systems. We can also reduce the separation between the two coupled waveguides to get a stronger coupling efficiency. In such a case, the imaginary part displays a discontinuity between the induced gain and absorption regions, as shown in Fig. 5.9. This is because that although the spatial variation of the coupling intensity is continuous between the gain/loss regions, the coupling frequency detuning is not. The

frequency detunings of the two coupling beams change independently in the gain and absorption regions to achieve the required gain and absorption values.

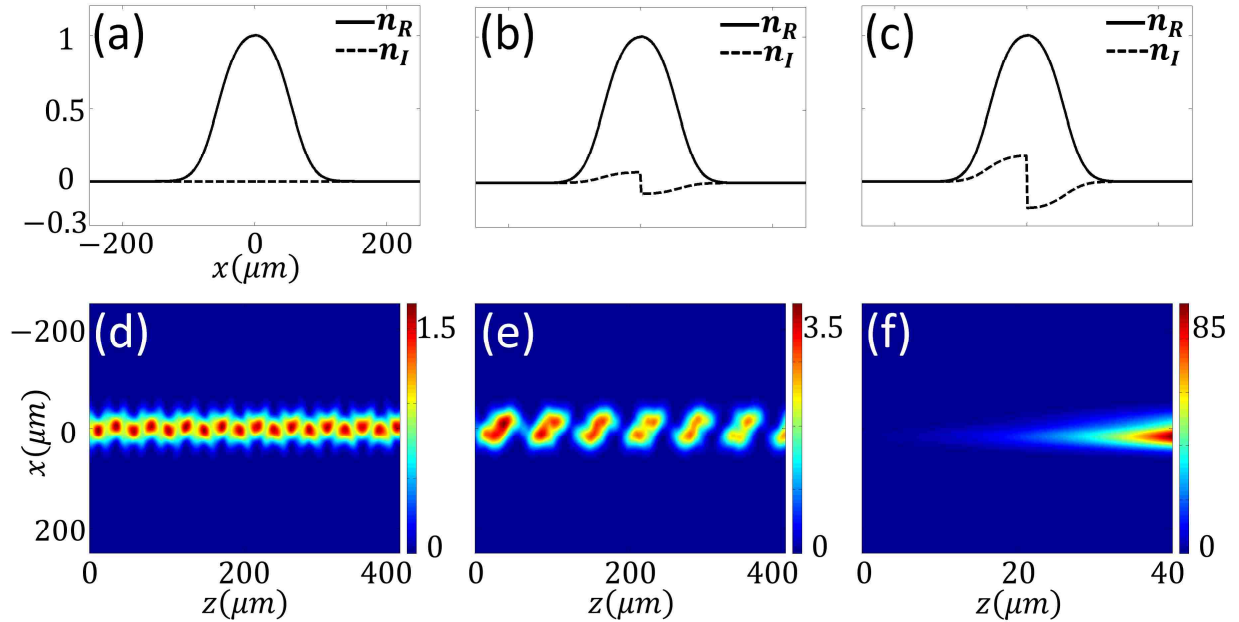


Figure 5.9: The real (solid black curves) and imaginary (dashed blue curves) refractive indices as a function of position x for (a) passive waveguide, (b) PT waveguide operating below symmetry breaking threshold, (c) PT waveguide above threshold. (d-f) Beam dynamics for each case.

Instead of using continuously-varying coupling intensity and discontinuously-varying the coupling frequency detuning to generate the optical lattice potentials, an alternative way is to use continuously-varying coupling and pump intensities. For example, the coupling and pump beam intensities are spatially modified as cosine and sine functions, respectively, while the other parameters remain uniform in space. In such case, a PT-symmetric optical lattice potential

can be established as shown in Fig. 5.10. The parameters used in generating Fig. 5.10 are $\Omega_c/2\pi = 0.5+0.4\cos(x/x_0)$ MHz, $\Omega_p/2\pi = 6.1+0.2\sin(x/x_0)$ MHz, $\Delta_c/2\pi = -2.98$ MHz, $\Delta_p/2\pi = -0.66$ MHz, and $x_0 = 1 \mu\text{m}$ is a scale factor. All other parameters are the same as in Fig. 5.5. The ratio between the real and imaginary indices in Fig. 5.10 is now ~ 7.6 , which is the below threshold case.

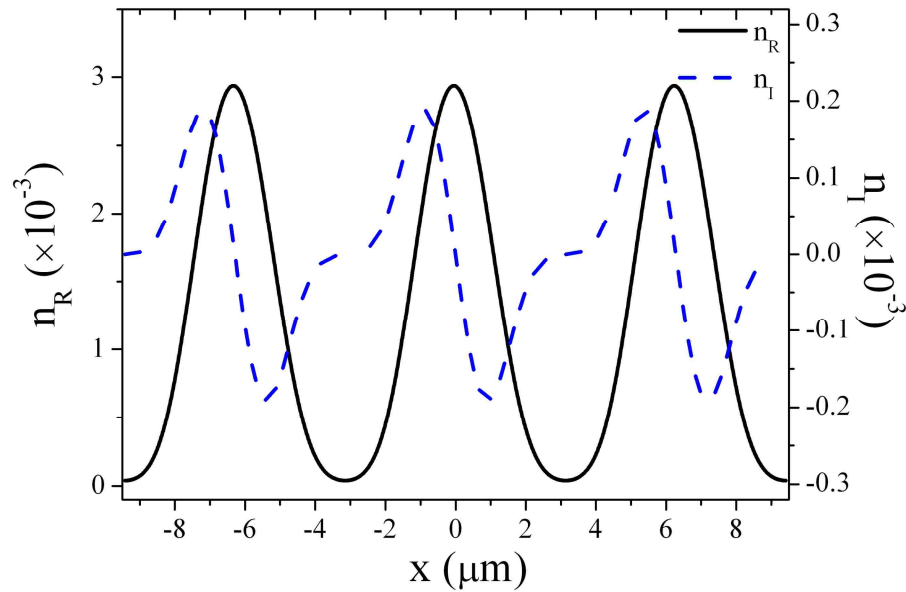


Figure 5.10: The real (solid black curves) and imaginary (dashed blue curves) parts of the refractive index for periodic lattices as a function of position x when the coupling and pump intensities are spatially modified.

The band structures of such optical lattice are also analyzed and shown to be consistent with previous studies (e.g. Ref. [128]). It is worth noting that if standing-wave coupling and pump fields in the z -direction have a fixed relative phase between them, then a periodic

photonic structure having PT-symmetry can be implemented [158]. Moreover, the lattice potential can be extended to two-dimensions (2D) when the coupling and pump intensities are simultaneously modulated in x and y directions. Figure 5.11 depicts a typical 2D PT-symmetric lattice potential for the parameters used in Fig. 5.10.

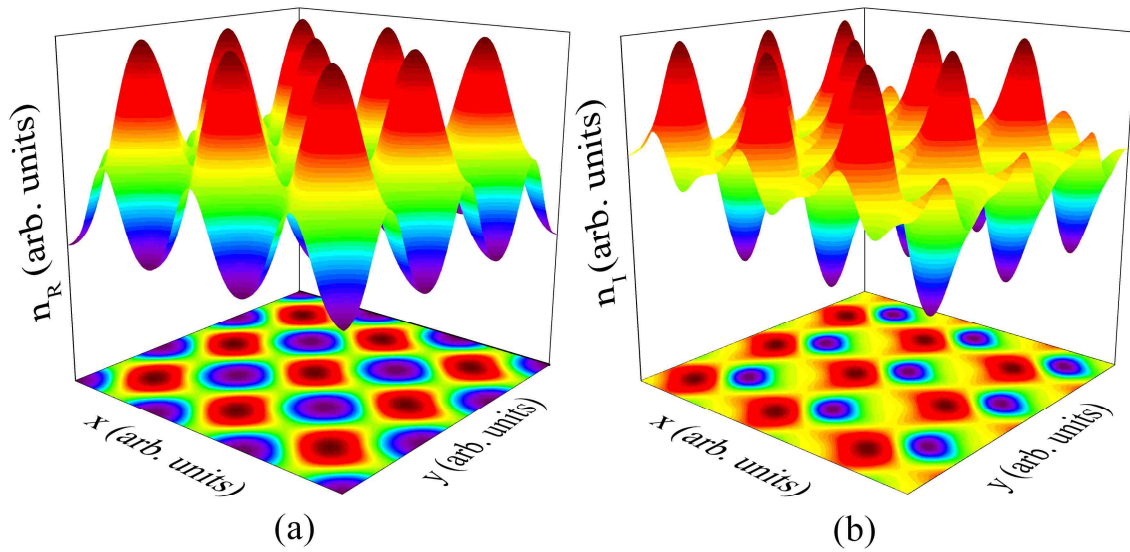


Figure 5.11: (a) Real and (b) imaginary indices for a 2D PT-symmetric lattice potential.

To achieve a stable and accurate PT-symmetric potential, fine manipulations of the complex refractive indices are required. Since most atomic parameters can be continuously modified in the current system, the PT-symmetric potentials can always be optimized even under some non-ideal approximations, for example, when the atomic diffusion and the validity of the paraxial approximation in vapor are included. In real experiment, the intensities and the phases can be monitored at the output of each waveguide channel. Depending on the longitudinal length of the lattice and system parameters, the output field patterns can be predicted either for

single or multiple channel excitations [128]. Therefore, the signature of PT symmetry can be verified through measuring the predicted unusual output phase and intensity patterns induced by secondary emission and double refraction.

The four-level N-type system described above is quite easy to realize in real atomic media and can be easily implemented under realistic experimental conditions, in contrast to the case when a mixture of isotopes is used to provide the gain/loss mechanisms, in which very large laser powers are needed and the system can only operate below PT-symmetric threshold with a relatively restricted ratio between the real/imaginary indices [159]. In addition, in the proposed scheme, only weak light intensities are required since all laser fields operate near atomic resonances. Moreover, different types of PT-symmetric potentials have been suggested that could operate either below or above the PT-symmetric threshold, depending on relevant atomic parameters. The ability to spatially modify the complex refractive index in coherent atomic media may lead to new routes in studying and observing PT-related phenomena and processes, and find applications in quantum switching, routing, and information processing. The future theoretical work based on this model can include Doppler broadening effect and also can study the influence of the decay rates on the degree of asymmetry.

5.2 Observation of discrete diffraction pattern in an optically induced lattice

By setting the ultimate goal to experimentally realize the PT-symmetric potentials in the coherently-prepared atomic medium as described in the previous section, we first begin our

experiment with the passive lattice case, i.e., without gain. The methods of using optical fields to make waveguide arrays or lattices have been realized in photorefractive crystal, and solitons have been demonstrated in such induced-lattice systems [160-167]. The electromagnetically induced waveguides [101,138-141], electromagnetically induced grating [168-173], and photonic band gaps [174,175] in EIT-based atomic media have also been studied before. EIT has also been used to control the motion of optical vortex arrays [176]. We have utilized EIT to spatially modify the refractive index in the Doppler-broadened rubidium atoms to construction an electromagnetically induced lattice (EIL) [172] in the transverse direction, and demonstrate that discrete diffraction patterns [177,178] can be observed when a weak probe beam propagates through such EIL. In this section, I will present some preliminary results obtained along this direction, but in a simpler ladder-type atomic system.

A ladder-type configuration is used in the experiment, as shown in Fig. 5.12(a) [5]. The probe field drives near the D_2 line and has a blue detuning of several hundreds MHz regarding to the $5S_{1/2}, F=3 \rightarrow 5P_{3/2}, F'=4$ transition of ^{85}Rb at wavelength 780 nm. The coupling field drives the $5P_{3/2} \rightarrow 5D_{5/2}$ transition (~ 775.987 nm). Two elliptical-shaped coupling beams incident into the Rb cell with an angle 2θ , and two standing-waves are generated in their intersection, one in transverse direction and another in the longitudinal direction, as shown in Fig. 5.12(b) and the snapshot (Fig. 5.12(c)). In this section, we only consider the standing-wave in transverse plane, whose period is determined by $d_1 = \lambda / 2 \sin \theta$. A Gaussian shaped probe beam counter-propagates with the two strong coupling beams and overlaps well with the optical

lattice induced by these two coupling beams.

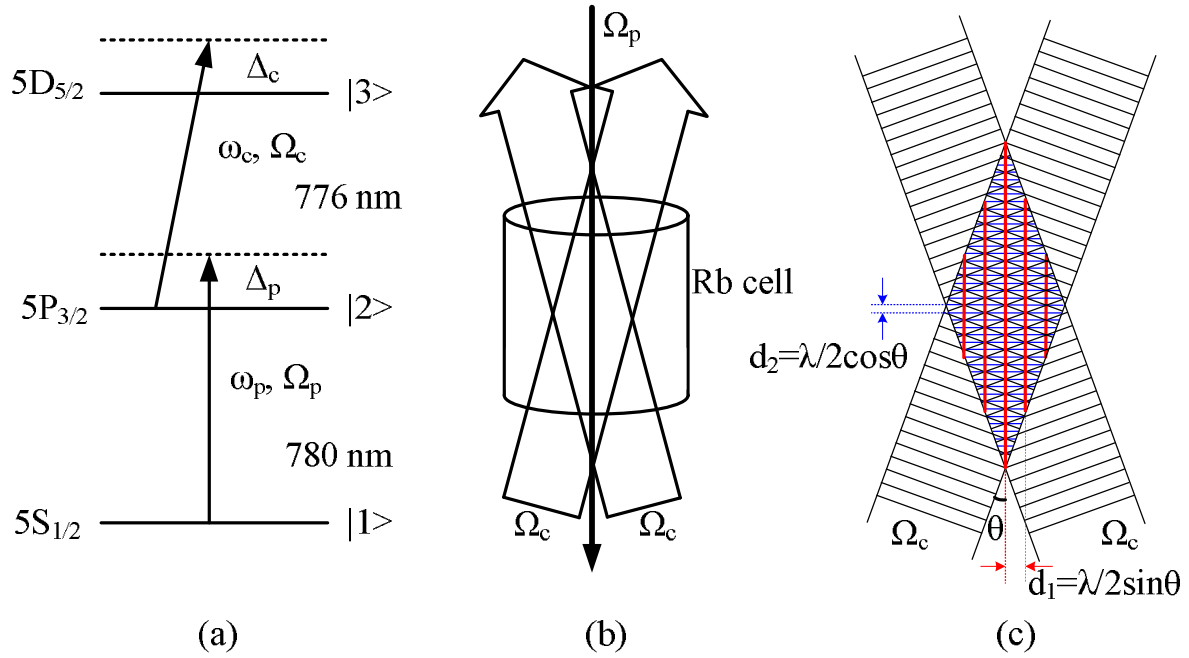


Figure 5.12: (a) Relevant energy levels of the ladder-type atomic system in Rb⁸⁵. (b) The schematic for generating an EIL in a hot rubidium vapor cell. (c) Snapshot of the EIL in (b).

The refractive index for the probe field depends on the intensity of the coupling field under EIT condition [27], as shown in the previous section. The ladder-type configuration used in the current experiment always shows absorption rather than gain, which is different from the N-type configuration shown in the previous section. We use the density-matrix method to theoretically model the ladder system as shown in Fig. 5.12(a). In order to reduce the absorption, we choose the coupling detuning to be $\Delta_c = -400$ MHz and probe detuning $\Delta_p = 390$ MHz. The real and imaginary (absorption) parts of the refractive index as a function of the transverse coordinate x are shown in Fig. 5.13, which shows an one-dimensional (1D) lattice with both the

real refractive index and absorption spatially modulated. To investigate the waveguide effect, the absorption needs to be suppressed. However, in the current atomic configuration, absorption can not be neglected. By choosing a relatively large single-photon coupling detuning, one can see from Fig. 5.13 that the contrast value of the absorption is about half of the real part value of the refractive index.

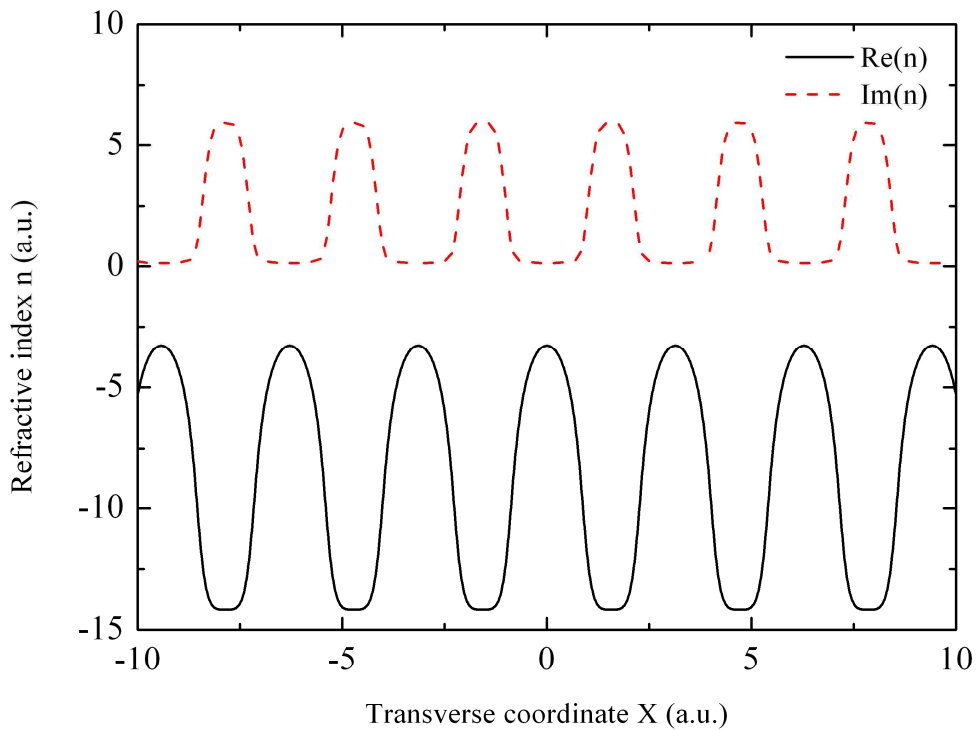


Figure 5.13: Theoretical plots of the spatially-modified real (solid black line) and imaginary (red dashed line) parts of the refractive index, respectively.

The discrete diffraction of a Gaussian beam propagating in such optical lattice can be simulated by the beam propagation method, which is given in Fig. 5.14. The parameters used in

the calculation are as following: the lattice space is $100 \mu\text{m}$ and the complex refractive index is

$$n = (10^{-5} + 0.5 \times 10^{-5} i) \cos x.$$

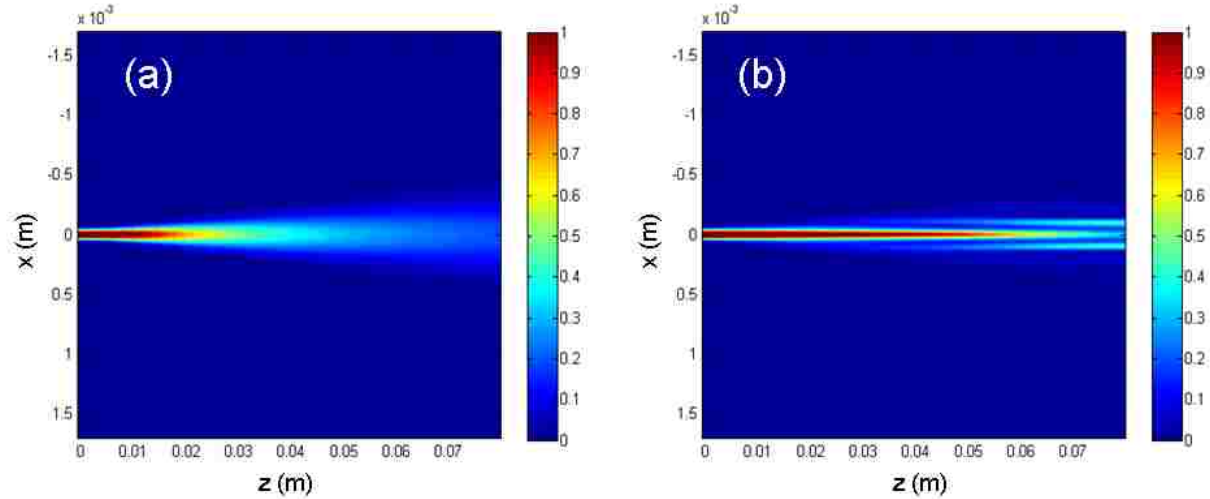


Figure 5.14: Theoretical simulation of probe beam propagation. (a) Free space diffraction of a Gaussian beam; (b) discrete diffraction of the weak Gaussian beam in an optical lattice.

Without the optical lattice induced by the two coupling fields, the output of the probe field through the Rb cell has a Gaussian shape, as shown in Fig. 5.14(a). When the 1D lattice is introduced, the discrete diffraction pattern can be clearly observed, as shown in Fig. 5.14(b). The propagating field is normalized for each step in the calculation owing to the absorption. Several crucial experimental parameters need to be carefully tuned in order to observe the discrete diffraction pattern. First, the pattern is very sensitive to the two-photon frequency detuning rather than the one-photon detuning. A clear discrete diffraction pattern only exists in a frequency window ~ 50 MHz near the two-photon (EIT) resonance. Second, the lattice space should be carefully adjusted to match the maximum refractive index contrast under current

experimental conditions. Third, in order to get as large refractive index contrast as possible, a straightforward way is to increase the atomic density in the Rb cell, hence, a high temperature (~ 100 °C) is used in the experiment, and the maximum index contrast obtainable under the current experimental conditions is estimated to be $\sim 10^{-5}$. However, under a high temperature condition, FWM process is likely to occur, hence, the probe field should be kept as low as possible. Certain careful balances have to be excised to observe the discrete diffraction pattern with weak probe beam.

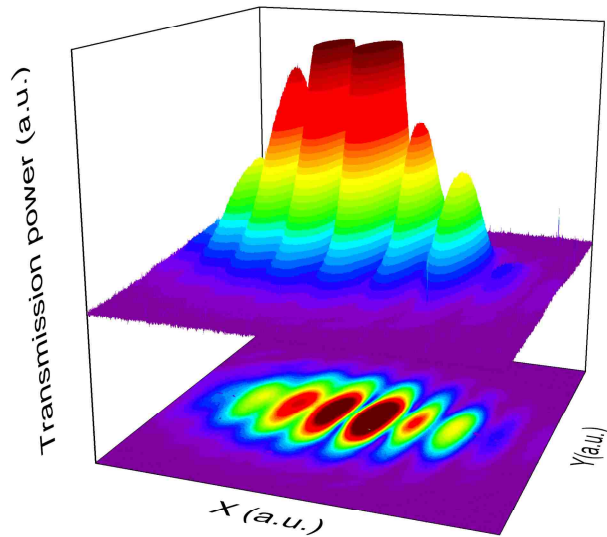


Figure 5.15: Experimental observation of the discrete diffraction pattern at the output of the vapor cell.

Figure 5.15 shows the experimental measured discrete diffraction pattern at the output of the atomic vapor cell. The two coupling beams are from the same Ti sapphire ring laser

separated by a beam splitter. Each coupling beam has the same power varies from 5 to 50 mW and the same size ($3.26 \times 0.90 \text{ mm}^2$). Generally, the larger coupling power makes the diffraction pattern easier to be observed. The probe beam power varies from 100 μW to 1 mW.

Typically, the lattice spacing can be controlled by the angle between two coupling beams and the complex refractive index can be controlled by the atomic detunings and the atomic density. The implementations of such controllable optically induced lattice in coherently-prepared atomic media offer novel platforms for further investigations in PT symmetry and other fascinating phenomena.

Chapter 6 Conclusions and outlook

In this thesis, I have described several studies of EIT-related phenomena in multilevel atomic systems. The optical properties of such multilevel atomic media under EIT condition can be significantly modified, for example, the steep normal linear dispersion and greatly enhanced nonlinearity with a negligible absorption near atomic resonance [2]. The most popular configuration for studying EIT-related effects is the so-called three-level lambda-type scheme, however, when an additional optical field is applied, several other schemes can be generated, such as four-level N-type and double-lambda-type systems, and each specific scheme has its own unique features and applications.

In Chapter 1, the basic properties and physical mechanisms about EIT and optical cavity are presented. When an EIT-related medium is placed inside an optical cavity, the optical properties of the cavity can be dramatically modified [2]. FWM processes in multilevel systems are also briefly introduced and the efficiency of FWM process can be greatly improved under EIT condition [31].

In Chapter 2, I have presented our studies on the cavity transmission spectra with three-level lambda-type, four-level N-type and double-lambda-type atoms inside an optical ring cavity, respective. In the three-level lambda-type atom-cavity system, side peak splitting and anti-crossing phenomenon can be observed under certain conditions [49]. By analyzing the intracavity dispersion and absorption properties, the cavity transmission spectra can be

theoretically studied under various conditions, e.g. coupling and cavity detunings, besides the on resonance case, and the theoretical results have been used to explain the experimentally measured data quite well. However, we only considered the case of one longitudinal cavity mode interacting with intracavity multilevel atoms. When multiple longitudinal modes are included, the cavity transmission spectra can be more complicated [179]. Future studies can include transverse modes, and explore the cavity output spatial imaging modifications under different EIT conditions. In the four-level N-type atom-cavity system, we demonstrated that the dark-state polariton peak is absorbed and then splits into two peaks when the power of the third field (switching field) is increasing [25]. An all-optical switch is realized with this interesting feature, and the extinction ratio can be much higher than the switching made with an N-type atomic system in free space [19]. More interesting phenomena can be observed when the coupling, switching, and cavity detunings are non-zeros, which need to be further investigated. In a double-lambda-type atom-cavity system, the dark-state polariton peak can be dramatically amplified by a FWM process [42]. In addition, ac-Stark effect has been investigated, which is influenced by both pump fields. Besides the above atomic systems, more other interesting atomic configurations coupled with an optical cavity can be studied in the future, e.g. M-type, Y-type, inverted-Y-type, etc.

In Chapter 3, I have shown our experimental observation of a novel type OM based on EIT, and the realization of optical multistate switch is realized by adding a pulse sequence on the probe field [94]. Such OM generated in a system with multilevel atomic medium inside an

optical ring cavity is closely related to OB [73] and can be changed to OB by simply tuning some experimental parameters, such as the power of the control field. In addition, OMs on both the signal and the generated Stokes fields in such multilevel atomic medium are experimentally observed simultaneously from two outputs of the cavity, and a dual-channel optical multistate switch is also realized. Such implemented optical switching has greatly improved communication capacity as compared to the regular binary switch based on OB [88]. More interesting properties of such OM, dependent on various other experimental parameters besides the power of the control field, have not been fully studied in the current experimental system yet. Four-state OM and more complicated hysteresis curves were also observed during experiments even though only three-state OM has been presented in this thesis. Such OM system can be theoretically modeled as a triple-well potential system, which can give more interesting phenomena and applications comparing to an OB system, which has been modeled as a double-well potential system [95]. Stochastic resonance [180], chaos [181], and quantum tunneling effects [95] are worth to be further studied in such new triple-well systems.

Chapter 4 presents two independent experimental studies. The first one is on measuring self-Kerr nonlinearity in an N-type atomic system by utilizing the cavity scanning method developed in our lab [26]. The cavity scanning technique was used to measure the self-Kerr nonlinearity efficient in a three-level lambda-type atomic system [26], and it can also be applied on other interesting atomic configurations, such as M-type, Y-type, inverted-Y-type and so on. In the N-type system, the slope of the self-Kerr nonlinearity near the atomic resonance can

change from negative to positive by simply increasing the power of the switching field, and the values of the self-Kerr nonlinearity coefficient at certain probe detunings can also be significantly modified by only changing the switching field power. The other experimental study is on the AOPO in the double-lambda atomic system, in which VIA effect and classical noise correlations are studied [41]. Both Stokes and anti-Stokes fields are generated by only using one pump field in a Doppler-broadened atomic medium confined in an optical ring cavity when the pump power exceeds certain threshold value, both Stokes and anti-Stokes fields will oscillate in the cavity. The pump and the generated Stokes and anti-Stokes fields should be quantum correlated and entangled in principle [124], which needs to be experimentally demonstrated and verified in the future.

In Chapter 5, I have described a theoretical model to show that an N-type atomic system with active Raman gain can be used to generate PT-symmetric potentials [27]. This is the first approach to generate PT symmetric potentials in a near-resonant atomic medium by spatially modifying the complex refractive index of the atomic medium. Such N-type atomic system can enhance the refractive index without absorption due to the balanced actions between the gain and absorption, which can also be very useful in generating optically controllable periodic photonic structures with zero absorption [156]. The generated PT-symmetric potential system has also interesting band structures, similar to the ones studied in Ref. [128], which require further investigations. When self-Kerr nonlinearity is considered in such N-type system, more interesting effects can occur. Optical diode is also possible owing to the nonreciprocal feature in

PT-symmetric potentials [146]. To realize the above proposal, we have experimentally generated an optically induced lattice in a ladder-type system. Discrete diffraction patterns have been observed which can be explained in either waveguide arrays [160] or grating [168] theories. The implementations of such controllable optically induced lattice in coherently-prepared atomic media offer novel platforms for further investigations in phenomena related to PT symmetry. Moreover, many other fascinating phenomena can be explored in such systems, such as solitons [144], quantum random walk [182], Talbot effect [183-186], and so on.

Bibliography

- [1] D. Suter, *the Physics of Laser-Atom Interactions* (Cambridge University Press 2005).
- [2] M. Fleischhauer, A. Imamoglu, and J. Marangos, “Electromagnetically induced transparency: Optics in coherent media”, *Rev. Mod. Phys.* **77**, 633 (2005).
- [3] S. E. Harris, J. E. Field, and A. Imamoglu, “Nonlinear optical processes using electromagnetically induced transparency”, *Phys. Rev. Lett.* **64**, 1107 (1990).
- [4] M. Xiao, Y. Li, S. Jin, and J. Gea-Banacloche, “Measurement of dispersive properties of electromagnetically induced transparency in rubidium atoms”, *Phys. Rev. Lett.* **74**, 666 (1995).
- [5] J. Gea-Banacloche, Y. Li, S. Jin, and M. Xiao, “Electromagnetically induced transparency in ladder-type inhomogeneously broadened media: Theory and experiment”, *Phys. Rev. A* **51**, 576 (1995).
- [6] M. O. Scully, “Enhancement of the index of refraction via quantum coherence”, *Phys. Rev. Lett.* **67**, 1855 (1991).
- [7] A. Imamoglu and S. E. Harris, “Lasers without inversion: interference of dressed lifetime-broadened states”, *Opt. Lett.* **14**, 1344 (1989).
- [8] E. A. Wilson, N. B. Manson, and C. Wei, “Perturbing an electromagnetic induced transparency within an inhomogeneously broadened transition”, *Phys. Rev. A* **67**, 023812 (2003).
- [9] A. Kasapi, “Three-dimensional vector model for a three-state system”, *J. Opt. Soc. Am. B* **13**, 1347 (1996).
- [10] M. O. Scully and M. S. Zubairy, *Quantum Optics* (Cambridge University Press, 1997).
- [11] L. V. Hau, S. E. Harris, Z. Dutton, and C. H. Behroozi, “Light speed reduction to 17 meters per second in an ultracold atomic gas”, *Nature* **397**, 594 (1999).
- [12] M. M. Kash, V. A. Sautenkov, A. S. Zibrov, L. Hollberg, G. R. Welch, M. D. Lukin, Y. Rostovtsev, E. S. Fry, and M. O. Scully, “Ultraslow Group Velocity and Enhanced Nonlinear Effects in a Coherently Driven Atomic Gas”, *Phys. Rev. Lett.* **82**, 5229 (1999).
- [13] D. F. Phillips, A. Fleischhauer, A. Mair, R. L. Walsworth, and M. D. Lukin, “Storage of light in atomic vapor”, *Phys. Rev. Lett.* **86**, 783 (2001).

- [14] C. Liu, Z. Dutton, C. H. Behroozi, and L. V. Hau, “Observation of coherent optical information storage in an atomic medium using halted light pulses”, *Nature* **409**, 490 (2001).
- [15] J. Appel, E. Figueroa, D. Korystov, M. Lobino, and A. I. Lvovsky, “Quantum memory for squeezed light”, *Phys. Rev. Lett.* **100**, 093602 (2008).
- [16] K. S. Choi, H. Deng, J. Laurat, and H. J. Kimble, “Mapping photonic entanglement into and out of a quantum memory”, *Nature* **452**, 67 (2008).
- [17] H. Schmidt and A. Imamoglu, “Giant Kerr nonlinearities obtained by electromagnetically induced transparency”, *Opt. Lett.* **21**, 1936 (1996).
- [18] S. E. Harris and Y. Yamamoto, “Photon switching by quantum interference”, *Phys. Rev. Lett.* **81**, 3611 (1998).
- [19] M. Yan, E. G. Rickey, and Y. Zhu, “Observation of absorptive photon switching by quantum interference”, *Phys. Rev. A* **64**, 041801(R) (2001).
- [20] D. A. Braje, V. Balić, G. Y. Yin, and S. E. Harris, “Low-light-level nonlinear optics with slow light”, *Phys. Rev. A* **68**, 041801(R) (2003).
- [21] Y.-F. Chen, Z.-H. Tsai, Y.-C. Liu, and I. A. Yu, “Low-light-level photon switching by quantum interference”, *Opt. Lett.* **30**, 3207 (2005).
- [22] W. Jiang, Q.-F. Chen, Y.-S. Zhang, and G.-C. Guo, “Optical pumping-assisted electromagnetically induced transparency”, *Phys. Rev. A* **73**, 053804 (2006).
- [23] M. G. Bason, A. K. Mohapatra, K. J. Weatherill, and C. S. Adams, “Narrow absorptive resonances in a four-level atomic system”, *J. Phys. B* **42**, 075503 (2009).
- [24] T. Y. Abi-Salloum, B. Henry, J. P. Davis, and F. A. Narducci, “Resonances and excitation pathways in four-level N-scheme atomic systems”, *Phys. Rev. A* **82**, 013834 (2010).
- [25] J. Sheng, X. Yang, U. Khadka, and M. Xiao, “All-optical Switching in an N-type Four-level Atom-cavity System”, *Opt. Express* **19**, 17059 (2011).
- [26] J. Sheng, X. Yang, H. Wu, and M. Xiao, “Modified self-Kerr-nonlinearity in a four-level N-type atomic system”, *Phys. Rev. A* **84**, 053820 (2011).
- [27] J. Sheng, M.-A. Miri, D. N. Christodoulides, and M. Xiao, “PT-symmetric optical potentials in a coherent atomic medium”, *Phys. Rev. A* **88**, 041803(R) (2013).

- [28] Y. Gu, L. Wang, K. Wang, C. Yang and Q. Gong, “Coherent population trapping and electromagnetically induced transparency in a five-level M-type atom”, *J. Phys. B: At. Mol. Opt. Phys.* **39**, 463 (2006).
- [29] A. Joshi and M. Xiao, “Electromagnetically Induced Transparency and Its Dispersion Properties in a Four-Level Inverted-Y Atomic System”, *Phys. Lett. A* **317**, 370 (2003); J. Wen, S. Du, Y. Zhang, M. Xiao, and M.H. Rubin, “Nonclassical Light Generation via a Four-level Inverted-Y System”, *Phys. Rev. A* **77**, 033816 (2008).
- [30] E. Paspalakis and P. L. Knight, “Electromagnetically induced transparency and controlled group velocity in a multilevel system”, *Phys. Rev. A* **66**, 015802 (2002); S. Rebić, D. Vitali, C. Ottaviani, P. Tombesi, M. Artoni, F. Cataliotti, and R. Corbalán, “Polarization phase gate with a tripod atomic system”, *Phys. Rev. A* **70**, 032317 (2004); D. Petrosyan and Y. P. Malakyan, “Magneto-optical rotation and cross-phase modulation via coherently driven four-level atoms in a tripod configuration”, *Phys. Rev. A* **70**, 023822 (2004).
- [31] P. R. Hemmer, D. P. Katz, J. Donoghue, M. Cronin-Golomb, M. S. Shahriar, and P. Kumar, “Efficient low-intensity optical phase conjugation based on coherent population trapping in sodium”, *Opt. Lett.* **20**, 982 (1995).
- [32] M. Jian, H. Xia, G. Y. Yin, A. J. Merriam, and S. E. Harris, “Efficient nonlinear frequency conversion with maximal atomic coherence”, *Phys. Rev. Lett.* **77**, 4326 (1996).
- [33] Y. Li and M. Xiao, “Enhancement of Non-Degenerate Four-Wave Mixing Using Electromagnetically Induced Transparency in Rubidium Atoms”, *Opt. Lett.* **21**, 1064 (1996); B. Lu, W. H. Burkett, and M. Xiao, “Nondegenerate Four-Wave Mixing in a Double- Λ System under the Influence of Coherent Population Trapping”, *Opt. Lett.* **23**, 804 (1998).
- [34] M. D. Lukin, A. B. Matsko, M. Fleischhauer, and M. O. Scully, “Quantum noise and correlations in resonantly enhanced wave mixing based on atomic coherence”, *Phys. Rev. Lett.* **82**, 1847 (1999).
- [35] M. Fleischhauer, M. D. Lukin, A. B. Matsko, and M. O. Scully, “Threshold and linewidth of a mirrorless parametric oscillator”, *Phys. Rev. Lett.* **84**, 3558 (2000).
- [36] V. Balic, D. A. Braje, P. Kolchin, G. Y. Yin, and S. E. Harris, “Generation of paired photons with controllable waveforms”, *Phys. Rev. Lett.* **94**, 183601 (2005).
- [37] C. H. van der Wal, M. D. Eisaman, A. Andr, R. L. Walsworth, D. F. Phillips, A. S. Zibrov, and M. D. Lukin, “Atomic memory for correlated photon states”, *Science* **301**, 196 (2003).

- [38] K. Harada, T. Kanbashi, M. Mitsunaga, and K. Motomura, “Competition between electromagnetically induced transparency and stimulated Raman scattering”, *Phys. Rev. A* **73**, 013807 (2006).
- [39] V. Boyer, A. M. Marino, R. C. Pooser, and P. D. Lett, “Entangled Images from Four-Wave Mixing”, *Science* **321**, 544 (2008).
- [40] R. M. Camacho, P. K. Vudyasetu, and J. C. Howell, “Four-wave-mixing stopped light in hot atomic rubidium vapour”, *Nature Photonics* **3**, 103 (2009).
- [41] J. Sheng, H. Wu, X. Yang, U. Khadka, and M. Xiao, “Noise correlations in a doubly-resonant atomic optical parametric oscillator”, *Opt. Lett.* **37**, 1655 (2012).
- [42] J. Sheng and M. Xiao, “Amplification of the intracavity dark-state field by a four-wave mixing process”, *Laser Physics Letters* **10**, 055402 (2013).
- [43] R. W. Boyd, *Nonlinear Optics* (Academic, New York, 1992).
- [44] H.-A. Bachor and T. C. Ralph, *a Guide to Experiments in Quantum Optics* (Wiley-VCH, Weinheim, 2004).
- [45] *Cavity Quantum Electrodynamics*, edited by P. R. Berman (Academic, San Diego, CA, 1994).
- [46] H. J. Kimble, “Strong interactions of single atoms and photons in cavity QED”, *Phys. Scr. T* **76**, 127 (1998).
- [47] G. S. Agarwal, “Spectroscopy of strongly coupled atom-cavity systems: A topical review”, *J. Mod. Opt.* **45**, 449 (1998).
- [48] Y. Zhu, D. J. Gauthier, S. E. Morin, Q. Wu, H. J. Carmichael, and T. W. Mossberg, “Vacuum Rabi splitting as a feature of linear-dispersion theory: Analysis and experimental observations”, *Phys. Rev. Lett.* **64**, 2499 (1990).
- [49] J. Sheng, H. Wu, M. Mumba, J. Gea-Banacloche, and M. Xiao, “Understanding cavity resonances with intracavity dispersion properties”, *Phys. Rev. A* **83**, 023829 (2011).
- [50] M. G. Raizen, R. J. Thompson, R. J. Brecha, H. J. Kimble, and H. J. Carmichael, “Normal-mode splitting and linewidth averaging for two-state atoms in an optical cavity”, *Phys. Rev. Lett.* **63**, 240 (1989).
- [51] R. J. Thompson, G. Rempe, and H. J. Kimble, “Observation of normal-mode splitting for

- an atom in an optical cavity”, *Phys. Rev. Lett.* **68**, 1132 (1992).
- [52] J. J. Childs, K. An, M. S. Otteson, R. R. Dasari, and M. S. Feld, “Normal-Mode Line Shapes for Atoms in Standing-Wave Optical Resonators”, *Phys. Rev. Lett.* **77**, 2901 (1996).
- [53] J. Gripp, S. L. Mielke, and L. A. Orozco, “Evolution of the vacuum Rabi peaks in a detuned atom-cavity system”, *Phys. Rev. A* **56**, 3262 (1997).
- [54] A. Boca, R. Miller, K. M. Birnbaum, A. D. Boozer, J. McKeever, and H. J. Kimble, “Observation of the Vacuum Rabi Spectrum for One Trapped Atom”, *Phys. Rev. Lett.* **93**, 233603 (2004).
- [55] P. Maunz, T. Puppe, I. Schuster, N. Syassen, P. W. H. Pinkse, and G. Rempe, “Normal-Mode Spectroscopy of a Single-Bound-Atom–Cavity System”, *Phys. Rev. Lett.* **94**, 033002 (2005).
- [56] A. K. Tuchman, R. Long, G. Vrijsen, J. Boudet, J. Lee, and M. A. Kasevich, “Normal-mode splitting with large collective cooperativity”, *Phys. Rev. A* **74**, 053821 (2006).
- [57] F. Brennecke, T. Donner, S. Ritter, T. Bourdel, M. Kohl, and T. Esslinger, “Cavity QED with a Bose–Einstein condensate”, *Nature* **450**, 268 (2007).
- [58] J. M. Fink, M. Goppl, M. Baur, R. Bianchetti, P. J. Leek, A. Blais, and A. Wallraff, “Climbing the Jaynes–Cummings ladder and observing its nonlinearity in a cavity QED system”, *Nature* **454**, 315 (2008).
- [59] M. Khudaverdyan, W. Alt, T. Kampschulte, S. Reick, A. Thobe, A. Widera, and D. Meschede, “Quantum Jumps and Spin Dynamics of Interacting Atoms in a Strongly Coupled Atom-Cavity System”, *Phys. Rev. Lett.* **103**, 123006 (2009).
- [60] Y. Choi, S. Kang, S. Lim, W. Kim, J. Kim, J. Lee, and K. An, “Quasieigenstate Coalescence in an Atom-Cavity Quantum Composite”, *Phys. Rev. Lett.* **104**, 153601 (2010).
- [61] J. Gea-Banacloche, H. Wu, and M. Xiao, “Transmission Spectrum of Doppler-broadened, Two-level Atoms in a Cavity in the Strong Coupling Regime”, *Phys. Rev. A* **78**, 023828 (2008).
- [62] E.T. Jaynes and F.W. Cummings, “Comparison of quantum and semiclassical radiation theories with application to the beam maser”, *Proc. IEEE* **51**, 89 (1963).
- [63] H. Wu, J. Gea-Banacloche, and M. Xiao, “Observation of Intracavity

- Electromagnetically-induced Transparency and Polariton Resonances in a Doppler-broadened Medium”, *Phys. Rev. Lett.* **100**, 173602 (2008).
- [64] M. Fleischhauer and M. D. Lukin, “Dark-state polaritons in electromagnetically induced transparency”, *Phys. Rev. Lett.* **84**, 5094 (2000).
- [65] G. Hernandez, J. Zhang, and Y. Zhu, “Vacuum Rabi splitting and intracavity dark state in a cavity-atom system,” *Phys. Rev. A* **76**, 053814 (2007).
- [66] M. Albert, A. Dantan, and M. Drewsen, “Cavity electromagnetically induced transparency and all-optical switching using ion Coulomb crystals”, *Nature Photon.* **5**, 633 (2011).
- [67] M. Mücke, E. Figueroa, J. Bochmann, C. Hahn, K. Murr, S. Ritter, C. J. Villas-Boas, and G. Rempe, “Electromagnetically induced transparency with single atoms in a cavity”, *Nature* **465**, 755 (2010).
- [68] Y. Wang, J. Zhang, and Y. Zhu, “Observation of dressed intracavity dark states,” *Phys. Rev. A* **85**, 013814 (2012).
- [69] H. Wu, J. Gea-Banacloche, and M. Xiao, “Splitting of atom-cavity polariton peaks for three-level atoms in an optical cavity,” *Phys. Rev. A* **80**, 033806 (2009).
- [70] M. D. Lukin, M. Fleischhauer, and M. O. Scully, “Intracavity electromagnetically induced transparency,” *Opt. Lett.* **15**, 295 (2000).
- [71] J. Zhang, G. Hernandez, and Y. Zhu, “Suppressing normal mode excitation by quantum interference in a cavity-atom system,” *Opt. Express* **16**, 7860 (2008).
- [72] W. Happer and B. S. Mathur, “Effective Operator Formalism in Optical Pumping”, *Phys. Rev.* **163**, 12 (1967).
- [73] L. A. Lugiato, in *Progress in Optics*, edited by E. Wolf (North-Holland, Amsterdam, 1984), Vol. XXI, p. 69.
- [74] H. M. Gibbs, *Optical Bistability: Controlling Light with Light* (Academic, New York, 1985).
- [75] H. M. Gibbs, S. L. McCall, and T. N. C. Venkatesan, “Differential Gain and Bistability Using a Sodium-Filled Fabry-Perot Interferometer”, *Phys. Rev. Lett.* **36**, 1135 (1976).
- [76] H. Wang, D. J. Goorskey, and M. Xiao, “Bistability and instability of three-level atoms inside an optical cavity”, *Phys. Rev. A* **65**, 011801(R) (2001).
- [77] A. Joshi, A. Brown, H. Wang, and M. Xiao, “Controlling optical bistability in a three-level

- atomic system”, *Phys. Rev. A* **67**, 041801 (2003).
- [78] M. Kitano, T. Yabuzaki, and T. Ogawa, “Optical Tristability”, *Phys. Rev. Lett.* **46**, 926 (1981).
- [79] S. Cecchi, G. Giusfredi, E. Petriella, and P. Salieri, “Observation of Optical Tristability in Sodium Vapors”, *Phys. Rev. Lett.* **49**, 1928 (1982).
- [80] E. Giacobino, “Tristability and bifurcations in sodium vapor”, *Opt. Commun.* **56**, 249 (1985).
- [81] J. Nalik, W. Lange, and F. Mitschke, “Complexity out of a simple structure: The intricate multistable behaviour of an optical resonator filled with sodium atoms”, *Appl. Phys. B* **49**, 191 (1989).
- [82] G. Giusfredi, P. Salieri, S. Cecchi, and F. T. Arecchi, “Multistability in a sodium filled Fabry-Perot: D1 line, hyperfine and Zeeman pumping”, *Opt. Commun.* **54**, 39 (1985).
- [83] N. A. Gippius, I. A. Shelykh, D. D. Solnyshkov, S. S. Gavrilov, Y. G. Rubo, A. V. Kavokin, S. G. Tikhodeev, and G. Malpuech, “Polarization Multistability of Cavity Polaritons”, *Phys. Rev. Lett.* **98**, 236401 (2007).
- [84] T. K. Parařso, M. Wouters, Y. Léger, F. Morier-Genoud, B. Deveaud-Plédran, “Multistability of a coherent spin ensemble in a semiconductor microcavity”, *Nat. Mater.* **9**, 655 (2010).
- [85] H. Wang, D. J. Goorskey, and M. Xiao, “Enhanced Kerr Nonlinearity via Atomic Coherence in a Three-Level Atomic System”, *Phys. Rev. Lett.* **87**, 073601 (2001).
- [86] W. Harshwardhan and G. S. Agarwal, “Controlling optical bistability using electromagnetic-field-induced transparency and quantum interferences”, *Phys. Rev. A* **53**, 1812 (1996).
- [87] A. Joshi and M. Xiao, “Optical Multistability in Three-Level Atoms Inside an Optical Ring Cavity”, *Phys. Rev. Lett.* **91**, 143904 (2003).
- [88] A. Brown, A. Joshi, and M. Xiao, “Controlled steady-state switching in optical bistability”, *Appl. Phys. Lett.* **83**, 1301 (2003).
- [89] R. Bonifacio and L. A. Lugiato, “Cooperative effects and bistability for resonance fluorescence”, *Opt. Commun.* **19**, 172 (1976); R. Bonifacio and L. A. Lugiato, “Optical bistability and cooperative effects in resonance fluorescence”, *Phys. Rev. A* **18**, 1129

(1978).

- [90] M A Antón and O. G. Calderón, “Optical bistability using quantum interference in V-type atoms”, *J. Opt. B* **4**, 91 (2002).
- [91] J.-H. Li, X.-Y. Lu, J.-M. Luo, and Q.-J. Huang, “Optical bistability and multistability via atomic coherence in an N-type atomic medium”, *Phys. Rev. A* **74**, 035801 (2006).
- [92] M. Sahrai, S. H. Asadpour, H. Mahrami, and R. SadighiBonabi, “Controlling the optical bistability via quantum interference in a four-level N-type atomic system”, *J. Lumin* **131**, 1682 (2011).
- [93] A. Joshi and M. Xiao, *Controlling Steady-State and Dynamical Properties of Atomic Optical Bistability* (World Scientific Publishing, 2012).
- [94] J. Sheng, U. Khadka, and M. Xiao, “Realization of All-optical Multistate Switching in an Atomic Coherent Medium”, *Phys. Rev. Lett.* **109**, 223906 (2012).
- [95] S. S. Hassan, P. D. Drummond, and D. F. Walls, “Dispersive optical bistability in a ring cavity”, *Opt. Commun.* **27**, 480 (1978); P. D. Drummond, “Quantum optical tunneling: A representation-free theory valid near the state-equation turning points”, *Phys. Rev. A* **33**, 4462 (1986).
- [96] H. Risken, C. Savage, F. Haake, and D. F. Walls, “Quantum tunneling in dispersive optical bistability”, *Phys. Rev. A* **35**, 1729 (1987).
- [97] T. S. El-Bawab, *Optical Switching* (Springer, 2006).
- [98] G. P. Agrawal, “Effect of mode coupling on optical bistability in a bidirectional ring cavity”, *Appl. Phys. Lett.* **38**, 505 (1981).
- [99] X. Yang, J. Sheng, U. Khadka, and M. Xiao, “Generation of correlated and anticorrelated multiple fields via atomic spin coherence”, *Phys. Rev. A* **85**, 013824 (2012).
- [100] Y. Zhang, U. Khadka, B. Anderson, and M. Xiao, “Temporal and Spatial Interference between Four-Wave Mixing and Six-Wave Mixing Channels”, *Phys. Rev. Lett.* **102**, 013601 (2009).
- [101] R. R. Moseley, S. Shepherd, D. J. Fulton, B. D. Sinclair, and M. H. Dunn, “Spatial Consequences of Electromagnetically Induced Transparency: Observation of Electromagnetically Induced Focusing”, *Phys. Rev. Lett.* **74**, 670 (1995).

- [102] M. Jain, A. J. Merriam, A. J. Kasapi, G. Y. Yin, and S. E. Harris, “Elimination of Optical Self-Focusing by Population Trapping”, *Phys. Rev. Lett.* **75**, 4385 (1995).
- [103] Y. Zhang, Z. Wang, Z. Nie, C. Li, H. Chen, K. Lu, and M. Xiao, “Four-Wave Mixing Dipole Soliton in Laser-Induced Atomic Gratings”, *Phys. Rev. Lett.* **106**, 093904 (2011).
- [104] H. Chang, Y. Du, J. Yao, C. Xie, and H. Wang, “Observation of cross-phase shift in hot atoms with quantum coherence”, *Europhys. Lett.* **65**, 485 (2004).
- [105] H. Kang and Y. Zhu, “Observation of Large Kerr Nonlinearity at Low Light Intensities”, *Phys. Rev. Lett.* **91**, 093601 (2003).
- [106] H.-Y. Lo, Y.-C. Chen, P.-C. Su, H.-C. Chen, J.-X. Chen, Y.-C. Chen, I. A. Yu, and Y.-F. Chen, “Electromagnetically-induced-transparency-based cross-phase-modulation at attojoule levels”, *Phys. Rev. A* **83**, 041804(R) (2011).
- [107] H. Wu and M. Xiao, “White-light cavity with competing linear and nonlinear dispersions”, *Phys. Rev. A* **77**, 031801(R) (2008).
- [108] D. Bouweester, A. Ekert, and A. Zeilinger, *The Physics of Quantum Information* (Springer-Verlag, Berlin, 2000).
- [109] Z. Y. Ou, S. F. Pereira, H. J. Kimble, and K. C. Peng, “Realization of the Einstein-Podolsky-Rosen paradox for continuous variables”, *Phys. Rev. Lett.* **68**, 3663 (1992).
- [110] A. Heidmann, R. J. Horowicz, S. Reynaud, E. Giacobino, C. Fabre, and G. Camy, “Observation of Quantum Noise Reduction on Twin Laser Beams”, *Phys. Rev. Lett.* **59**, 2555 (1987)
- [111] A. S. Coelho, F. A. S. Barbosa, K. N. Cassemiro, A. S. Villar, M. Martinelli, and P. Nussenzveig, “Three-Color Entanglement”, *Science* **326**, 823 (2009).
- [112] A. Kuzmich, W. P. Bowen, A. D. Boozer, A. Boca, C. W. Chou, L.-M. Duan & H. J. Kimble, “Generation of nonclassical photon pairs for scalable quantum communication with atomic ensembles”, *Nature* **423**, 731 (2003).
- [113] James K. Thompson, Jonathan Simon, Huanqian Loh, and Vladan Vuletić, “A High-Brightness Source of Narrowband, Identical-Photon Pairs”, *Science* **313**, 74 (2006).
- [114] H. Yan, S. Zhang, J. F. Chen, M. M. T. Loy, G. K. L. Wong, and S. Du, “Generation of Narrow-Band Hyperentangled Nondegenerate Paired Photons”, *Phys. Rev. Lett.* **106**,

033601 (2011).

- [115] V. Boyer, A. Marino, R. Pooser, and P. Lett, “Entangled Images from Four-Wave Mixing”, *Science* **321**, 544 (2008).
- [116] H. Wu and M. Xiao, “Bright correlated twin beams from an atomic ensemble in the optical cavity”, *Phys. Rev. A* **80**, 063415 (2009).
- [117] V. A. Sautenkov, Y. V. Rostovtsev, and M. O. Scully, “Switching between photon-photon correlations and Raman anticorrelations in a coherently prepared Rb vapor”, *Phys. Rev. A* **72**, 065801 (2005).
- [118] J. Okuma, N. Hayashi, A. Fujisawa, M. Mitsunaga, and K. Harada, “Parametric oscillation in sodium vapor by using an external cavity”, *Opt. Lett.* **34**, 698 (2009).
- [119] H. Zheng, U. Khadka, J. Song, Y. Zhang, and M. Xiao, “Three-field noise correlation via third-order nonlinear optical processes”, *Opt. Lett.* **36**, 2584 (2011).
- [120] H. Tanji-Suzuki, W. Chen, R. Landig, J. Simon, and V. Vuletić, “Vacuum-Induced Transparency”, *Science* **333**, 1266 (2011).
- [121] X. Yu, M. Xiao, and J. Zhang, “Triply-resonant optical parametric oscillator by four-wave mixing with rubidium vapor inside an optical cavity”, *Appl. Phys. Lett.* **96**, 041101 (2010).
- [122] H. Wu, M. Xiao, and J. Gea-Banacloche, “Evidence of Lasing without Inversion in a Hot rubidium Vapor under Electromagnetically-induced-transparency Conditions”, *Phys. Rev. A* **78**, 041802 (R) (2008).
- [123] D. Budker, D. F. Kimball, S. M. Rochester, and V. V. Yashchuk, “Nonlinear Magneto-optics and Reduced Group Velocity of Light in Atomic Vapor with Slow Ground State Relaxation”, *Phys. Rev. Lett.* **83**, 1767 (1999).
- [124] Y. Yu, J. Sheng, and M. Xiao, “Generation of bright quadricolor continuous-variable entanglement by four-wave-mixing process”, *Phys. Rev. A* **83**, 012321 (2011).
- [125] C. M. Bender and S. Boettcher, “Real Spectra in Non-Hermitian Hamiltonians Having PT Symmetry”, *Phys. Rev. Lett.* **80**, 5243 (1998).
- [126] C. M. Bender, “Making sense of non-Hermitian Hamiltonians”, *Rep. Prog. Phys.* **70**, 947 (2007), and references therein.
- [127] R. El-Ganainy, K. G. Makris, D. N. Christodoulides, and Z. H. Musslimani, “Theory of

- coupled optical PT-symmetric structures”, *Opt. Lett.* **32**, 2632 (2007).
- [128] K. G. Makris, R. El-Ganainy, D. N. Christodoulides, and Z. H. Musslimani, “Beam Dynamics in PT Symmetric Optical Lattices”, *Phys. Rev. Lett.* **100**, 103904 (2008).
- [129] S. Klaiman, U. Günther, and N. Moiseyev, “Visualization of Branch Points in PT-Symmetric Waveguides”, *Phys. Rev. Lett.* **101**, 080402 (2008).
- [130] M. C. Zheng, D. N. Christodoulides, R. Fleischmann, and T. Kottos, “PT optical lattices and universality in beam dynamics”, *Phys. Rev. A* **82**, 010103 (2010).
- [131] Y. Chong, L. Ge, and A. Stone, “PT-Symmetry Breaking and Laser-Absorber Modes in Optical Scattering Systems”, *Phys. Rev. Lett.* **106**, 093902 (2011).
- [132] A. A. Sukhorukov, Z. Xu, and Y. S. Kivshar, “Nonlinear suppression of time reversals in PT-symmetric optical couplers”, *Phys. Rev. A* **82**, 043818 (2010)
- [133] A. Miroshnichenko, B. Malomed, and Y. Kivshar, “Nonlinearly PT-symmetric systems: Spontaneous symmetry breaking and transmission resonances”, *Phys. Rev. A* **84**, 012123 (2011).
- [134] S. Longhi, “Bloch Oscillations in Complex Crystals with PT Symmetry”, *Phys. Rev. Lett.* **103**, 123601 (2009).
- [135] A. Guo, G. J. Salamo, D. Duchesne, R. Morandotti, M. Volatier-Ravat, V. Aimez, G. A. Siviloglou, and D. N. Christodoulides, “Observation of PT-Symmetry Breaking in Complex Optical Potentials”, *Phys. Rev. Lett.* **103**, 093902 (2009).
- [136] C. E. Rüter, K. G. Makris, R. El-Ganainy, D. N. Christodoulides, M. Segev, and D. Kip, “Observation of parity–time symmetry in optics”, *Nat. Phys.* **6**, 192 (2010).
- [137] A. Regensburger, C. Bersch, M.-A. Miri, G. Onishchukov, D. N. Christodoulides, and U. Peschel, “Parity–time synthetic photonic lattices”, *Nature* **488**, 167 (2012).
- [138] R. Kapoor and G. S. Agarwal, “Theory of electromagnetically induced waveguides”, *Phys. Rev. A* **61**, 053818 (2000).
- [139] A. G. Truscott, M. E. J. Friese, N. R. Heckenberg, and H. Rubinsztein-Dunlop, “Optically Written Waveguide in an Atomic Vapor”, *Phys. Rev. Lett.* **82**, 1438 (1999)
- [140] P. K. Vudyasetu, D. J. Starling, and J. C. Howell, “All Optical Waveguiding in a Coherent Atomic Rubidium Vapor”, *Phys. Rev. Lett.* **102**, 123602 (2009).

- [141] O. Firstenberg, M. Shuker, N. Davidson, and A. Ron, “Elimination of the diffraction of arbitrary images imprinted on slow light”, *Phys. Rev. Lett.* **102**, 043601 (2009); O. Firstenberg, P. London, M. Shuker, A. Ron, and N. Davidson, “Elimination, reversal and directional bias of optical diffraction”, *Nat. Phys.* **5**, 665 (2009).
- [142] J. Cheng and S. Han, “Electromagnetically induced self-imaging”, *Opt. Lett.* **32**, 1162 (2007).
- [143] H. Ling, Y. Li, and M. Xiao, “Electromagnetically induced grating: Homogeneously broadened medium”, *Phys. Rev. A* **57**, 1338 (1998).
- [144] T. Hong, “Spatial Weak-Light Solitons in an Electromagnetically Induced Nonlinear Waveguide”, *Phys. Rev. Lett.* **90**, 183901 (2003); Y. Wu and L. Deng, “Ultraslow Optical Solitons in a Cold Four-State Medium”, *Phys. Rev. Lett.* **93**, 143904 (2004); H. Michinel, M. J. Paz-Alonso, and V. M. Pérez-García, “Turning Light into a Liquid via Atomic Coherence”, *Phys. Rev. Lett.* **96**, 023903 (2006).
- [145] W. Huang, “Coupled-mode theory for optical waveguides: an overview”, *J. Opt. Soc. Am. A* **11**, 963 (1994).
- [146] H. Ramezani, T. Kottos, R. El-Ganainy and D. N. Christodoulides, “Unidirectional nonlinear PT-symmetric optical structures”, *Phys. Rev. A* **82**, 043803 (2010).
- [147] Z. Lin, H. Ramezani, T. Eichelkraut, T. Kottos, H. Cao, and D. N. Christodoulides, “Unidirectional Invisibility Induced by PT-Symmetric Periodic Structures”, *Phys. Rev. Lett.* **106**, 213901 (2011).
- [148] S. Longhi, “PT-symmetric laser absorber”, *Phys. Rev. A* **82**, 031801(R) (2010).
- [149] M.-A. Miri, P. LiKamWa, and D. N. Christodoulides, “Large area single-mode parity–time-symmetric laser amplifiers”, *Opt. Lett.* **37**, 764 (2012).
- [150] H. Kang, L. Wen, and Y. Zhu, “Normal or anomalous dispersion and gain in a resonant coherent medium”, *Phys. Rev. A* **68**, 063806 (2003).
- [151] S. Kuang, C. Jin, and C. Li, “Gain-phase grating based on spatial modulation of active Raman gain in cold atoms”, *Phys. Rev. A* **84**, 033831 (2011).
- [152] M. Fleischhauer, C. H. Keitel, M. O. Scully, C. Su, B. T. Ulrich, and S. Y. Zhu, “Resonantly enhanced refractive index without absorption via atomic coherence”, *Phys. Rev. A* **46**, 1468 (1992).

- [153] A. S. Zibrov, M. D. Lukin, L. Hollberg, D. E. Nikonov, M. O. Scully, H. G. Robinson, and V. L. Velichansky, “Experimental Demonstration of Enhanced Index of Refraction via Quantum Coherence in Rb”, *Phys. Rev. Lett.* **76**, 3935 (1996).
- [154] D. D. Yavuz, “Refractive Index Enhancement in a Far-Off Resonant Atomic System”, *Phys. Rev. Lett.* **95**, 223601 (2005).
- [155] N. A. Proite, B. E. Unks, J. T. Green, and D. D. Yavuz, “Refractive Index Enhancement with Vanishing Absorption in an Atomic Vapor”, *Phys. Rev. Lett.* **101**, 147401 (2008).
- [156] C. O’Brien and O. Kocharovskaya, “Optically Controllable Photonic Structures with Zero Absorption”, *Phys. Rev. Lett.* **107**, 137401 (2011).
- [157] J. Durnin, J. J. Miceli, Jr., J. H. Eberly, “Diffraction-free beams”, *Phys. Rev. Lett.* **58**, 1499 (1987).
- [158] L. Feng, Y. Xu, W. S. Fegadolli, M. Lu, J. E. B. Oliveira, V. R. Almeida, Y. Chen, and A. Scherer, “Experimental demonstration of a unidirectional reflectionless parity-time metamaterial at optical frequencies”, *Nature Materials* **12**, 108 (2013).
- [159] C. Hang, G. Huang, and V. V. Konotop, “PT Symmetry with a System of Three-Level Atoms”, *Phys. Rev. Lett.* **110**, 083604 (2013).
- [160] D. N. Christodoulides and R. I. Joseph, “Discrete self-focusing in nonlinear arrays of coupled waveguides”, *Opt. Lett.* **13**, 794 (1988).
- [161] N. K. Efremidis, S. M. Sears, D. N. Christodoulides, J. W. Fleischer, and M. Segev, “Discrete solitons in photorefractive optically induced photonic lattices”, *Phys. Rev. E* **66**, 046602 (2002).
- [162] J. W. Fleischer, T. Carmon, M. Segev, N. K. Efremidis, and D. N. Christodoulides, “Observation of Discrete Solitons in Optically Induced Real Time Waveguide Arrays”, *Phys. Rev. Lett.* **90**, 023902 (2003).
- [163] J. W. Fleischer, M. Segev, N. K. Efremidis, and D. N. Christodoulides, “Observation of two-dimensional discrete solitons in optically induced nonlinear photonic lattices”, *Nature* **422**, 147 (2003).
- [164] Z. Chen and K. McCarthy, “Spatial soliton pixels from partially incoherent light”, *Opt. Lett.* **27**, 2019 (2002).
- [165] D. Neshev, E. Ostrovskaya, Y. Kivshar, and W. Królikowski, “Spatial solitons in optically

- induced gratings”, *Opt. Lett.* **28**, 710 (2003).
- [166] D. N. Neshev, T. J. Alexander, E. A. Ostrovskaya, Y. S. Kivshar, H. Martin, I. Makasyuk, and Z. Chen, “Observation of Discrete Vortex Solitons in Optically Induced Photonic Lattices”, *Phys. Rev. Lett.* **92**, 123903 (2004)
- [167] I. L. Garanovich, S. Longhi, A. A. Sukhorukova, and Y. S. Kivshar, “Light propagation and localization in modulated photonic lattices and waveguides”, *Phys. Rep.* **518**, 1 (2012).
- [168] H. Ling, Y. Li, and M. Xiao, “Electromagnetically Induced Grating: Homogeneously Broadened Medium”, *Phys. Rev. A* **57**, 1338 (1998).
- [169] M. Mitsunaga and N. Imoto, “Observation of an electromagnetically induced grating in cold sodium atoms”, *Phys. Rev. A* **59**, 4773 (1999).
- [170] G. C. Cardoso and J. W. Tabosa, “Electromagnetically induced gratings in a degenerate open two-level system”, *Phys. Rev. A* **65**, 033803 (2002).
- [171] L. E. E. de Araujo, “Electromagnetically induced phase grating”, *Opt. Lett.* **35**, 977 (2010).
- [172] Y. Zhang, C. Yuan, H. Zheng, H. Chen, C. Li, Z. Wang and M. Xiao, “Surface Solitons of Four-wave Mixing in Electromagnetically Induced Lattice”, *Laser Physics Letters* **10**, 055406 (2013).
- [173] B. Little, D. J. Starling, J. C. Howell, R. D. Cohen, D. Shwa, and N. Katz, “Rapidly reconfigurable optically induced photonic crystals in hot rubidium vapor”, *Phys. Rev. A* **87**, 043815 (2013).
- [174] A. André and M. D. Lukin, “Manipulating Light Pulses via Dynamically Controlled Photonic Band gap”, *Phys. Rev. Lett.* **89**, 143602 (2002).
- [175] D. Wang, H. Zhou, M. Guo, J. Zhang, J. Evers, and S. Zhu, “Optical Diode Made from a Moving Photonic Crystal”, *Phys. Rev. Lett.* **110**, 093901 (2013).
- [176] D. Shwa, E. Shtranvasser, Y. Shalibo, and N. Katz, “Controllable motion of optical vortex arrays using electromagnetically induced transparency”, *Opt. Express* **20**, 24835 (2012).
- [177] T Pertsch, T Zentgraf, U Peschel, A Bräuer, and F Lederer, “Anomalous refraction and diffraction in discrete optical systems”, *Phys. Rev. Lett.* **88**, 093901 (2002).

- [178] G. D. Valle, S. Longhi, P. Laporta, P. Biagioni, L. Duò, and M. Finazzi, “Discrete diffraction in waveguide arrays: A quantitative analysis by tunneling optical microscopy”, *Appl. Phys. Lett.* **90**, 261118 (2007).
- [179] X. Yu, M. Xiao, and J. Zhang, “Triply-resonant optical parametric oscillator by four-wave mixing with rubidium vapor inside an optical cavity”, *Appl. Phys. Lett.* **96**, 041101 (2010).
- [180] A. Joshi and M. Xiao, “Stochastic Resonance in Atomic Optical Bistability”, *Phys. Rev. A*, **74**, 013817 (2006).
- [181] W. Yang, A. Joshi, and M. Xiao, “Chaos in an Electromagnetically Induced Transparency Medium inside an Optical Cavity”, *Phys. Rev. Lett.* **95**, 093902 (2005).
- [182] A. Peruzzo, M. Lobino, J. C. F. Matthews, N. Matsuda, A. Politi, K. Poulios, X. Zhou, Y. Lahini, N. Ismail, K. Wörhoff, Y. Bromberg, Y. Silberberg, M. G. Thompson, and J. L. O'Brien, “Quantum Walks of Correlated Photons”, *Science* **329**, 1500 (2010).
- [183] R. Iwanow, D. A. May-Arrioja, D. N. Christodoulides, G. I. Stegeman, Y. Min, and W. Sohler, “Discrete Talbot Effect in Waveguide Arrays”, *Phys. Rev. Lett.* **95**, 053902 (2005).
- [184] H. Ramezani, D. N. Christodoulides, V. Kovanis, I. Vitebskiy, and T. Kottos, “PT-Symmetric Talbot Effects”, *Phys. Rev. Lett.* **109**, 033902 (2012).
- [185] Y. Zhang, J. Wen, S. Zhu, and M. Xiao, “Nonlinear Talbot effect”, *Phys. Rev. Lett.* **104**, 183901 (2010).
- [186] J. Wen, S. Du, H. Chen, and M. Xiao, “Electromagnetically induced Talbot effect”, *Appl. Phys. Lett.* **98**, 081108 (2011).

A Publications of dissertation author

A.1. Journal papers

1. **Jiteng Sheng**, J. Wang, and Min Xiao, "Synchronous control of dual-channel all-optical multistate switching", *Optics Letters*, accepted, 2013.
2. **Jiteng Sheng**, M.-A. Miri, D. N. Christodoulides, and Min Xiao, "PT-symmetric optical potentials in a coherent atomic medium", *Phys. Rev. A* **88**, 041803(R) (2013).
3. U. Khadka, **Jiteng Sheng**, and Min Xiao, "Spatial-domain interactions between ultra-weak optical beams", *Phys. Rev. Lett.* **111**, 223601 (2013).
4. J. F. Wang, **Jiteng Sheng**, S. N. Zhu, and Min Xiao, "Implementation of bright two-color quadripartite continuous-variable entanglement by the quantum optical dimer", *J. Opt. Soc. Am. B* **30**, 2130 (2013).
5. **Jiteng Sheng** and Min Xiao, "Amplification of the intracavity dark-state field by a four-wave mixing process", *Laser Physics Letters* **10**, 055402 (2013).
6. **Jiteng Sheng**, U. Khadka, and Min Xiao, "Realization of all-optical multistate switching in an atomic coherent medium", *Phys. Rev. Lett.* **109**, 223906 (2012).
7. U. Khadka, **Jiteng Sheng**, X. Yang, and Min Xiao, "Measurement of two independent phase-shifts using coupled parametric amplifiers", *New Journal of Physics* **14**, 043026 (2012).
8. **Jiteng Sheng**, H. Wu, X. Yang, U. Khadka, and Min Xiao, "Noise correlations in a doubly-resonant atomic optical parametric oscillator", *Optics Letters* **37**, 1655 (2012).
9. X. Yang, **Jiteng Sheng**, U. Khadka, and Min Xiao, "Generation of correlated and anti-correlated multiple Fields via atomic spin coherence", *Phys. Rev. A* **85**, 013824 (2012).
10. **Jiteng Sheng**, X. Yang, H. Wu, and Min Xiao, "Modified self-Kerr-nonlinearity in a four-level N-type atomic system", *Phys. Rev. A* **84**, 053820 (2011).
11. X. Yang, **Jiteng Sheng**, and Min Xiao, "Electromagnetically induced absorption via incoherent collisions", *Phys. Rev. A* **84**, 043837 (2011).
12. **Jiteng Sheng**, X. Yang, U. Khadka, and Min Xiao, "All-optical switching in an N-type four-level atom-cavity system", *Optics Express* **19**, 17059 (2011).
13. X. Yang, **Jiteng Sheng**, U. Khadka, and Min Xiao, "Simultaneous control of two four-wave mixing fields via atomic spin coherence", *Phys. Rev. A* **83**, 063812 (2011).

14. **Jiteng Sheng**, H. Wu, M. Mumba, J. Gea-Banacloche, and Min Xiao, "Understanding cavity resonances with intracavity dispersion properties", *Phys. Rev. A* **83**, 023829 (2011).
15. Y. B. Yu, **Jiteng Sheng**, and Min Xiao, "Generation of bright quadricolor continuous-variable entanglement by four-wave mixing process", *Phys. Rev. A* **83**, 012321 (2011).

A.2. Conference presentations

1. **Jiteng Sheng**, M.-A. Miri, D. N. Christodoulides, and M. Xiao, "PT symmetry in coherent atomic media", CLEO/QELS conference, June 9-14, 2013.
2. **Jiteng Sheng** and M. Xiao, "Nonlinear optical effects in N-type four-level atom-cavity systems", CLEO/QELS conference, May 6-11, 2012.
3. **Jiteng Sheng**, H. Wu, J. Gea-Banacloche, and M. Xiao, "Observation of interference between bright- and dark-polariton peaks", CLEO/QELS conference, May 16-21, 2010.